

# FINAL REPORT

Expanded Processing Techniques for EMI Systems

SERDP Project MR-1772

JULY 2012

Mark Prouty  
**Geometrics, Inc.**

Skip Snyder  
**Snyder Geoscience, Inc.**

David George  
**G&G Sciences, Inc.**

Charles Oden  
**Earth Science Systems, LLC**

*This document has been cleared for public release*



<b>Report Documentation Page</b>			Form Approved OMB No. 0704-0188	
<p>Public reporting burden for the collection of information is estimated to average 1 hour per response, including the time for reviewing instructions, searching existing data sources, gathering and maintaining the data needed, and completing and reviewing the collection of information. Send comments regarding this burden estimate or any other aspect of this collection of information, including suggestions for reducing this burden, to Washington Headquarters Services, Directorate for Information Operations and Reports, 1215 Jefferson Davis Highway, Suite 1204, Arlington VA 22202-4302. Respondents should be aware that notwithstanding any other provision of law, no person shall be subject to a penalty for failing to comply with a collection of information if it does not display a currently valid OMB control number.</p>				
1. REPORT DATE <b>JUL 2012</b>	2. REPORT TYPE <b>N/A</b>	3. DATES COVERED <b>-</b>		
4. TITLE AND SUBTITLE <b>Expanded Processing Techniques for EMI Systems</b>			5a. CONTRACT NUMBER	
			5b. GRANT NUMBER	
			5c. PROGRAM ELEMENT NUMBER	
6. AUTHOR(S)			5d. PROJECT NUMBER	
			5e. TASK NUMBER	
			5f. WORK UNIT NUMBER	
7. PERFORMING ORGANIZATION NAME(S) AND ADDRESS(ES) <b>Geometrics, 2190 Fortune Drive, San Jose, CA 95131</b>			8. PERFORMING ORGANIZATION REPORT NUMBER	
9. SPONSORING/MONITORING AGENCY NAME(S) AND ADDRESS(ES)			10. SPONSOR/MONITOR'S ACRONYM(S)	
			11. SPONSOR/MONITOR'S REPORT NUMBER(S)	
12. DISTRIBUTION/AVAILABILITY STATEMENT <b>Approved for public release, distribution unlimited</b>				
13. SUPPLEMENTARY NOTES <b>The original document contains color images.</b>				
14. ABSTRACT <b>The goal of this project was to improve the data processing algorithms and optimize the instrument using the results and experience of prior MetalMapper UXO-discrimination demonstrations at the former Camp San Luis Obispo and the former Camp Butner. We explored 4 main topics. First, we examined the detection algorithms and discovered that, indeed, it is possible to perform better target detection using physics-based algorithms and the entire data set, rather than simulating a simpler data set and mapping the result. Secondly, we examined the data array itself, and conclude that a smaller set of receivers could be used, so long as the instrument is accurately located above the unknown target. The outer receivers provide significant benefit for interrogating targets at an offset of more than 40cm from the center of the array. Thirdly, we generalized our inversion algorithms to allow for data to be combined from more than one instrument location. Finally, we examined methods for inverting and analyzing data from multiple targets simultaneously.</b>				
15. SUBJECT TERMS				
16. SECURITY CLASSIFICATION OF:			17. LIMITATION OF ABSTRACT <b>SAR</b>	18. NUMBER OF PAGES <b>84</b>
a. REPORT <b>unclassified</b>	b. ABSTRACT <b>unclassified</b>	c. THIS PAGE <b>unclassified</b>		
19a. NAME OF RESPONSIBLE PERSON				

# REPORT DOCUMENTATION PAGE

*Form Approved  
OMB No. 0704-0188*

Public reporting burden for this collection of information is estimated to average 1 hour per response, including the time for reviewing instructions, searching existing data sources, gathering and maintaining the data needed, and completing and reviewing this collection of information. Send comments regarding this burden estimate or any other aspect of this collection of information, including suggestions for reducing this burden to Department of Defense, Washington Headquarters Services, Directorate for Information Operations and Reports (0704-0188), 1215 Jefferson Davis Highway, Suite 1204, Arlington, VA 22202-4302. Respondents should be aware that notwithstanding any other provision of law, no person shall be subject to any penalty for failing to comply with a collection of information if it does not display a currently valid OMB control number. **PLEASE DO NOT RETURN YOUR FORM TO THE ABOVE ADDRESS.**

<b>1. REPORT DATE (DD-MM-YYYY)</b> 24-07-2012			<b>2. REPORT TYPE</b> Final		<b>3. DATES COVERED (From - To)</b> 10/10 to 04/12	
<b>4. TITLE AND SUBTITLE</b>  Expanded Processing Techniques for EMI Systems			<b>5a. CONTRACT NUMBER</b> W912HQ-10-C-0067			
			<b>5b. GRANT NUMBER</b>			
			<b>5c. PROGRAM ELEMENT NUMBER</b>			
<b>6. AUTHOR(S)</b>  Mark Prouty, D.D. Snyder, Dave George, Charles Oden			<b>5d. PROJECT NUMBER</b> MR-1772			
			<b>5e. TASK NUMBER</b>			
			<b>5f. WORK UNIT NUMBER</b>			
<b>7. PERFORMING ORGANIZATION NAME(S) AND ADDRESS(ES)</b>  Geometrics, 2190 Fortune Drive, San Jose, CA 95131			<b>8. PERFORMING ORGANIZATION REPORT NUMBER</b>			
<b>9. SPONSORING / MONITORING AGENCY NAME(S) AND ADDRESS(ES)</b>  SERDP			<b>10. SPONSOR/MONITOR'S ACRONYM(S)</b>			
			<b>11. SPONSOR/MONITOR'S REPORT NUMBER(S)</b>			
<b>12. DISTRIBUTION / AVAILABILITY STATEMENT</b>  Distribution unlimited						
<b>13. SUPPLEMENTARY NOTES</b>						
<b>14. ABSTRACT</b>  The goal of this project was to improve the data processing algorithms and optimize the instrument using the results and experience of prior MetalMapper UXO-discrimination demonstrations at the former Camp San Luis Obispo and the former Camp Butner. We explored 4 main topics. First, we examined the detection algorithms and discovered that, indeed, it is possible to perform better target detection using physics-based algorithms and the entire data set, rather than simulating a simpler data set and mapping the result. Secondly, we examined the data array itself, and conclude that a smaller set of receivers could be used, so long as the instrument is accurately located above the unknown target. The outer receivers provide significant benefit for interrogating targets at an offset of more than 40cm from the center of the array. Thirdly, we generalized our inversion algorithms to allow for data to be combined from more than one instrument location. Finally, we examined methods for inverting and analyzing data from multiple targets simultaneously.						
<b>15. SUBJECT TERMS</b>  MetalMapper, UXO, EM, Time Domain, EMI						
<b>16. SECURITY CLASSIFICATION OF:</b>			<b>17. LIMITATION OF ABSTRACT</b>	<b>18. NUMBER OF PAGES</b>	<b>19a. NAME OF RESPONSIBLE PERSON</b> Mark Prouty	
<b>a. REPORT</b> U	<b>b. ABSTRACT</b> U	<b>c. THIS PAGE</b> U	None	84	<b>19b. TELEPHONE NUMBER (include area code)</b> 408-954-0522	

## Table of Contents

<b>1</b>	<b>Objective.....</b>	<b>1</b>
<b>2</b>	<b>Background .....</b>	<b>3</b>
<b>3</b>	<b>Materials and Methods .....</b>	<b>5</b>
3.1	MMTargets .....	5
3.2	Constrained Single-Target Inversion.....	6
3.3	The F-Test Statistic.....	7
3.4	F-Test - Synthetic Target Populations.....	7
3.5	F-Test and the Detection of Rod-Like Targets.....	11
<b>4</b>	<b>Results.....</b>	<b>14</b>
<b>4.1</b>	<b>Improved Target Detection (Task 1) .....</b>	<b>14</b>
4.1.1	Introduction and Background .....	14
4.1.2	Traditional method .....	14
4.1.3	MetalMapper refinements to traditional method.....	15
4.1.4	Objective of this work and basic considerations .....	16
4.1.5	Enabling and limiting concepts .....	16
4.1.6	Requirements placed upon our methods .....	17
4.1.7	Progress of our work and lessons learned .....	18
4.1.8	Method of Signal Pattern Correlation .....	19
4.1.9	Results .....	27
4.1.10	Conclusions and Recommendations.....	30
4.1.11	Traditional Inversion Using Dynamic Data .....	32
<b>4.2</b>	<b>Optimizing The MetalMapper Receiver Array (Task 2).....</b>	<b>34</b>
4.2.1	Background .....	34
4.2.2	Arrays Studied.....	37
4.2.3	Target Space.....	38
4.2.4	Target Features .....	39
4.2.5	Electromagnetic Interference.....	40
4.2.6	Position and Attitude Uncertainty.....	41
4.2.7	Parameter Extraction.....	41
4.2.8	SNR and MSE.....	42
4.2.9	Target Size & Time Persistence .....	42
4.2.10	Target Shape .....	43
4.2.11	An Array Performance Metric .....	46
4.2.12	Array Performance Results.....	46
4.2.13	Single-Site Data – Sphere Target.....	46
4.2.14	Single-Site Data – Prolate Spheroid Target.....	47
4.2.15	Multi-Site Performance .....	48
4.2.16	Conclusions- Optimum Array Study.....	50
4.2.17	Recommendations for Further Study.....	51
<b>4.3</b>	<b>Parameter Extraction Using Multi-Point Data Sets (Task 3).....</b>	<b>53</b>
<b>4.4</b>	<b>Multiple Source Detection (Task 4).....</b>	<b>55</b>
4.4.1	Reduction-to-Pole and Downward Continuation .....	56
4.4.2	Multi-Target Inversion .....	62

<b>4.5 Oasis Montaj Integration (Task 5) .....</b>	<b>66</b>
<b>5 Discussion and Recommendations .....</b>	<b>70</b>
<b>5.1 New Contributions and Conclusions .....</b>	<b>70</b>
<b>5.2 Recommendations and Future Work.....</b>	<b>71</b>
5.2.1 Recommendation for <i>MMTargets</i> .....	71
5.2.2 Recommendation for Detection .....	71
5.2.3 Recommendations for Optimal Arrays.....	72
5.2.4 Recommendations for Multiple Targets .....	72
5.2.5 Recommendations for Oasis montaj Enhancements.....	72
<b>5.3 Future Plans.....</b>	<b>73</b>
<b>6 References .....</b>	<b>74</b>
<b>7 Appendix A .....</b>	<b>75</b>

## List of Figures

Figure 2.1: MetalMapper at San Luis Obispo.....	3
Figure 2.2: Performance curves from San Luis Obispo.....	4
Figure 2.3: Performance curves from Camp Butner.....	4
Figure 3.1: Comparison of the polarizability curves produced by <i>MMTargets</i> and by <i>MMRMP</i> . <i>MMTargets</i> results correctly suggest a rod-like object, while the <i>MMRMP</i> results suggest a plate-like object.....	6
Figure 3.2: Histograms showing the distribution of F-Test values for 3 constrained solutions generated by <i>MMTargets</i> . The targets are a 180 mm oblate spheroid (1:3 aspect ratio), and a 60mm prolate spheroid (3:1 aspect ratio). The constraints are prolate spheroid (PS), oblate spheroid (OS), and sphere (SP).....	8
Figure 3.3: Scatter-plots showing the behavior of the F-Test statistic (prolate spheroid constraint) when plotted with other useful target features as the ordinate. The top row (A) uses a symmetry feature, the middle row (B) uses the time persistence of the major principal polarizability curve ( $dP_x/dt$ ), and the bottom (C) is a measure of the aspect ratio of rod-like body. The left-hand column shows data plot for the full target set (250 targets). The right- hand column uses a reduced target set (193 targets) wherein targets with offsets greater than 0.4m have been excluded.....	9
Figure 3.4: Scatter plot of a target attribute indicating rod-like symmetry ( $P_{oy}/P_{oz}$ ) against the F- Test attribute with prolate spheroid constraint (A), the oblate spheroid constraint (B), and the sphere constraint (C). The test data set consists of 250 identical 60mm prolate spheroids at random locations and random attitudes (see Section 4.3 of this report). The left hand column plots the full target set (FS). In the right hand column, we plot a reduced target set (RS) that generally excludes targets with horizontal offsets ( $r$ ) greater than 0.4m. ....	10
Figure 3.5: Figure showing the distribution of SNR (A) and the cumulative distribution of SNR (B) for 750 targets equally distributed between 250 60mm prolate spheroids (PS-3:1 aspect), 250 180mm oblate spheroids (OS-1:3 aspect), and 250 100mm spheres.....	11
Figure 3.6: Stacked histogram showing the distribution of $F_{PS}$ (F-Test PS) for the 750-target test population (250 PS, 250 OS, 250 SP). The colors identify the type.....	12
Figure 3.7: ROC curve showing the performance of the F-Test (PS) for detection of rod-like bodies of symmetry (BOR). The parameter is an F-Test threshold value. All targets with F- Test values larger than the threshold are designated as non-detectable (ND). The offsets of the 2 curves indicate the number ND's found for the indicated threshold. ....	12
Figure 4.1: Screen shot pictures of implementation in EM3D. The left panel shows a target at a depth of 35cm passing under the array. The right hand panel shows a much larger target at a depth of 75cm or so passing just outside the array. ....	23
Figure 4.2: User interface for Signal Pattern Correlation within Oasis montaj.....	24
Figure 4.3: Data profiles along Line 1, the westernmost line. The Avg5IZ trace is the signal that is similar to that produced by an EM61. The orange trace is effective RMS signal from seven MetalMapper sensors. Note these traces are plotted on a log/linear scale. The red points in the second panel are correlation coefficient while the blue points are dipole moments. The DelXDisp, DelYDisp, and DepthDisp traces show the target positions in cart-relative coordinates (cm from the center of the cart).....	26

Figure 4.4: Color contour plot of the area studied. The plot is made from the “5IZ” value – a signal roughly similar to the response of an EM61. The faint dots show the track of data points along each of 10 lines. The white crosses are computed target positions. The whole area is shown to the left. Two overlapping halves are enlarged to the right (top on the left, bottom on the right). .....	28
Figure 4.5: Map showing picks using the Signal Correlation method (white circles) compared to picks using the traditional method (black triangles). Area shown is the same as in Figure 4.4.....	29
Figure 4.6: Transient data for cube 3 (center cube) for a profile of dynamic MM data acquired over the IVS at Butner (July 2010).....	32
Figure 4.7: Results of operating MMTargets on a profile of dynamic MM data acquired over the IVS at Butner. The upper profile shows the “detection indicator” (related to 1/MSE). The lower profile plots the RMS value of the data (similar to the magenta profile in Figure 4.6). .....	33
Figure 4.8: Three “optimal” arrays evaluated by Grimm for the AOL system design. The annotation “3-C” indicates 3-component receivers. Arrays A and B have a single horizontal transmitter. Array C has 3 orthogonal transmitters and is therefore suitable for cued ID measurements from a single point. ....	34
Figure 4.9: An example of the principal polarizability transients estimated from two data sets over the same UXO target. A large lateral offset (~0.5m) between the center of the antenna platform and the target in the case of SLOStatA01584 caused the transverse polarizability axes to be inadequately illuminated. Note that the shape of the major polarizability transient (red curve) is nicely resolved. ....	36
Figure 4.10: Antenna arrays evaluated during this study. All receiver coils are located on the diagonals of the Z (horizontal) transmitter coil. ....	37
Figure 4.11: Random target locations (250) occupying an octant of a spheroid centered on the horizontal transmitter loop and having a half-length equal to 10X the diameter of the target (100mm or 60mm). ....	38
Figure 4.12: Principal polarizability transients for the 100mm sphere (top) and the 60mm diameter prolate spheroid used as targets in this study.....	39
Figure 4.13:Definition of 5 target features used in this report as the basis for an index of array performance. The values of these 5 parameters are known (Table 2.1). The distribution of the parameter estimates in linear or log space suggests that they form a Gaussian normal distribution. ....	40
Figure 4.14: : RMS noise levels measured with the MM at Camp Butner, NC in 2010. The noise levels are shown for the case when the Z transmitter is energized. The noise when the X and Y transmitters are energized is similar in magnitude and behavior. ....	40
Figure 4.15:Summary of the distribution of SNR (A), MSE (B) and the relationship between the two (C & D). The figures are based on inversions of 250 target data sets for the 3T7C-MM array. ....	42
Figure 4.16: Scatter plots showing target clustering based on 2 different size parameters (Size A/SizeB). For each of these parameters we have used the time persistence ( $\tau_{12}$ ) as the plot ordinate. The histograms shown below the scatter plots exhibit approximate bilateral symmetry about a mean value of 0. Thus a good measure of array performance based on these 3 parameters would be the standard deviation ( $\sigma$ ) of the plotted parameter.....	43

Figure 4.17: Scatter plots of EM aspect ratio parameter (A- $P_{0E}$ ) and symmetry parameter (B-RL0) versus target position relative to the platform reference point. The difference between the FS plots (left columns) and RS plots (right columns) demonstrate that it is difficult to resolve shape for shallow targets with horizontal offsets ( $r$ ) near 0.5m .....	44
Figure 4.18: Histograms showing the distribution of $P_{0R}$ and $\text{Log}_{10}\text{RL}_0$ . These figures show that these two shape parameters have a mean value near their known values and bilateral symmetry.....	45
Figure 4.19: Performance summary for 6 arrays evaluated using the sphere target set. The upper panel represents results for the full set (FS), the lower panel shows results for the reduced (RS) target set .....	46
Figure 4.20: Performance summary for the 3 best 3-C arrays from evaluation with the sphere target. The performance is based on parameters extracted from the 60mm prolate spheroid target set with single-site parameter extraction. The top panel represents performance with the full target set. The bottom panel is for the reduced target set.....	47
Figure 4.21: Performance summary for the 3 best 3-C arrays from evaluation with the sphere target. The performance is based on parameters extracted from both the 100mm sphere and the 60mm prolate spheroid target sets with single-site parameter extraction. The left panel represents performance with the full target set (FS). The right panel is for the reduced target set (RS). ....	48
Figure 4.22: Performance results for 2-point parameter extraction with the 3T7C-MM (Left panel) and 3T5C-30 (Right panel) arrays. The performance estimates uses parameter estimates from the sphere target group. For comparison, we show the performance of the single-point extractions (center bar). ....	50
Figure 4.23: The left image shows two pink rectangles indicating the queued cart locations for two presumed independent targets. The right image shows the recovered 37 mm target ..	53
Figure 4.24: The recovered polarizability curves obtained with MMTTargets using data from queued data locations 479 and 481 simultaneously.....	54
Figure 4.25: Plots of simulated <i>MetalMapper</i> data for two oblate spheroidal targets in close proximity (targets 1 and 2 from Table 3.2) The dots indicate receiver locations from a single cued snapshot. These sparse data are insufficient to capture the high-frequency character of the anomalies. ....	55
Figure 4.26: Plots of simulated <i>MetalMapper</i> data for two oblate spheroidal targets in close proximity. Black dots indicate receiver locations from four cued snapshots. The shaded region shows the footprint of the <i>MetalMapper</i> cart. These data are sufficient to capture the high-frequency character of the anomalies.....	56
Figure 4.27: Left: original image from two vertically oriented oblate spheroid targets (target 3 and 4 from Table 4.2). Right: original image from two horizontally oriented oblate spheroid targets (target 5 and 6 from Table 4.2). Colored dots indicate receiver locations, and large black dots (and arrows) indicate true target positions. These maps simulate data acquired along two adjacent profiles offset by a distance of 1m.....	57
Figure 4.28: Images resulting from application of non-uniform Fourier transform followed by uniform inverse transform. Left: image from two vertically oriented oblate spheroid targets (target 3 and 4 from Table 4.2). Right: image from two horizontally oriented oblate spheroid targets (target 5 and 6 from Table 4.2). No window function was used. Colored dots indicate data points, and large black dots (and arrows) indicate true target position. ....	58

Figure 4.29: Frequency-domain amplitude spectra for dipoles at various depths. The amplitude spectra are independent of dipole orientation. ....	60
Figure 4.30: Images resulting from the reduction-to-pole routine. Left: image from two vertically oriented oblate spheroid targets (target 3 and 4 from Table 6.1). Right: image from two horizontally oriented oblate spheroid targets (target 5 and 6 from Table 6.1). Colored dots indicate data points, and large black dots (and arrows) indicate true target positions. Energy peaks are now very close to actual target locations. ....	61
Figure 4.31: Images resulting from application downward continuation routines. Left: image from two vertically oriented oblate spheroid targets (target 3 and 4 from Table 3.2). Right: image from two horizontally oriented oblate spheroid targets (target 5 and 6 from Table 3.2). Colored dots indicate data points, and large black dots (and arrows) indicate true target positions. ....	61
Figure 4.32: Images resulting from application of both the reduction-to-pole and downward continuation routines. Left: image from two vertically oriented oblate spheroid targets (target 3 and 4 from Table 3.2). Right: image from two horizontally oriented oblate spheroid targets (target 5 and 6 from Table 3.2). Colored dots indicate data points, and large black dots (and arrows) indicate true target positions. Energy peaks are very close to target locations. ....	62
Figure 4.33: Dialog for converting TEM files to CSV files to import into <i>Oasis</i> . ....	66
Figure 4.34: Dialog for converting noise file from TEM to SU format for <i>MMTargets</i> . ....	66
Figure 4.35: Selecting CSV files for importing into <i>Oasis</i> .....	67
Figure 4.36: Resulting imported data after selecting CSV files for importing into <i>Oasis</i> .....	67
Figure 4.37: Dialog for invoking <i>MMTargets</i> in single target inversion mode.....	67
Figure 4.38: Example of a targets database containing results from <i>MMTargets</i> inversion. ....	68
Figure 4.39: Example of a target summary plot. ....	69

## List of Tables

Table 4.1: Tabulation of various target features extracted from principal polarizabilities shown in Figure 6 and the target dimensions. ....	39
Table 4.2. Target parameters used to generate modeled data for testing frequency-domain filters and multiple inversion algorithms. ....	56
Table 4.3. Single-target inversion results (unconstrained positions) and true values from repeated from Table 6.1. ....	63
Table 4.4. Multi-target inversion results (constrained lateral positions) and true values from repeated from Table 6.1. ....	65
Table 4.5: <i>MMTargets</i> single target properties list. ....	68

## List of Acronyms

1-C	One Component (receiver)
3-C	Three Component (receiver)
2-D	Two Dimensional
AOL	Advanced Ordnance Locator
AOL2	Advanced Ordnance Locator (2 <sup>nd</sup> Generation)
APG	Aberdeen Proving Ground
BOR	Body Of Revolution
EL	Ellipsoid
EMI	Electromagnetic Induction
ESS	Earth Science Systems, LLC
ESTCP	Environmental Security Technology Certification Program
FS	Full (target) Set
ID	Identification
MSE	Mean Squared Error
ND	Not Detectable
OS	Oblate Spheroid
PS	Prolate Spheroid
ROC	Receiver Operating Characteristic
RS	Reduced (target) Set
SLO	San Luis Obispo
SERDP	Strategic Environmental Research and Development Program
SGI	Snyder Geoscience Incorporated
SNR	Signal to Noise Ratio
SP	Sphere
TOI	Target of Interest
USGS	United States Geological Survey
UXO	Unexploded Ordnance
YPG	Yuma Proving Ground

## Keywords

Unexploded Ordnance, EM Induction, Array, Inversion, MetalMapper

## Acknowledgements

This work was supported by the Strategic Environmental Research and Development Program Project MR-1772.

## 1 Objective

The goal of this project was to expand existing investigations and processing routines for so-called “Advanced EMI” arrays. Previous demonstrations conducted with advanced systems both at seeded sites (e.g., APG and YPG) and live sites such as Camp Sibert, AL, Camp San Luis Obispo (SLO), and Camp Butner have shown that unanswered questions remain relating to antenna array configuration, physics-based target modeling, and classification. Our objective here has not been to develop new sensors, sensor hardware, or programs for target modeling. Rather, it is to seize an opportunity to review and update earlier research in retrospect in order to search for a better and/or simpler antenna configuration, and to maximize the benefit derived from these systems through expanded data processing and better anomaly classification. The study we conducted was enabled and justified by the fact that real data and ground truth was available from the ESTCP classification studies at SLO and Camp Butner in North Carolina. The research has been focused on five specific objectives:

1. Improved Target Detection – The objective of this task was to exploit the capability of an instrument such as the *MetalMapper*, which samples the vector field at multiple locations inside the transmitter loop, to generate simple physics-based estimates of position and size of targets within the field of view of the transmitter. Applied to dynamic data either in real-time during acquisition or during post-acquisition processing, this type of processing can serve as a primary target picking screen that sorts targets into at least 2 and perhaps 3 categories: 1) high-confidence clutter; 2) targets selected for cued ID; and perhaps 3) high-confidence targets of interest (i.e. dig). The advantage here is to reduce the number of anomalies that must be revisited for static data collection. These algorithms have been implemented as part of the acquisition software, allowing the operator to see a higher-level processed answer in real-time to assist in re-locating static targets, or to stop and acquire static data.
2. Target Parameter Extraction with Multiple-Point Static or Dynamic Data Sets – The *MetalMapper* and other advanced EMI systems were developed with cued target characterization in mind. In principle, a data set acquired at a single spatial measurement point is sufficient for the target analysis. Here, our objective has been to determine the extent to which the quality of parameter extraction is enhanced by sampling the secondary EMI response at several spatial points in the proximity of the target. In addition, we have analyzed the ability to discriminate targets using the dynamic data. We find that some of the benefits obtained from more sample points over a larger aperture will be offset by two mechanisms. First, the platform is in motion, producing noise and position uncertainty. Second, the dynamic data acquired with the *MetalMapper* used only the vertical axis transmitter.
3. Optimal Array Configuration(s) – The goal was to define one or more antenna arrays that meet the need for cost-effective sensor arrays for static (i.e. cued) measurements for characterization and identification. This could result in smaller systems that are easier to deploy and less expensive, yet may provide nearly equivalent performance for discrimination.

4. Multiple Source Detection – The objective here is to identify those target picks associated with complex secondary magnetic fields that arise either from the presence of multiple targets in close proximity, targets that are asymmetrical, or that may be too large dimensionally to be approximated with a point dipole. A multi-target inversion algorithm has been developed and tested. Downward continuation and reduction-to-pole algorithms have also been developed to aid interpretation and to provide useful starting models for the multi-target inversion.
5. Oasis montaj Integration – This task was not part of the original work scope, but was added after the program office suggested that the new routines should be integrated into existing *Oasis montaj* workflows.

Although some of these objectives overlap (e.g. detecting multiple targets), the methods for reaching these objectives are different.

Work was performed on this project by Geometrics , Snyder Geoscience (SGI), Earth Science Systems (ESS), and G&G Sciences. SGI was primarily involved with supplying data, creating data format conversion routines, testing the codes, and conducting the optimal array configuration analysis. ESS wrote the software for modeling data, inverting data, target detection, complex source treatment, and Oasis montage integration. SGI and ESS charged time against Task 2, “Parameter Extraction Using Multi-Point Data Sets” and towards Task 3, “Optimal Array Configurations”. ESS charged time against Task 2, “Parameter Extraction Using Multi-Point Data Sets”, Task 4, “Multiple Source Detection”, and Task 5, “*Oasis montaj* Integration”. Task 1, “Improved Target Detection”, was tackled by G & G Geosciences. Geometrics performed the overall management of the project.

## 2 Background

With ESTCP support (MM-0603), Geometrics undertook the commercialization of an advanced EMI system, called the MetalMapper, for application to UXO detection and characterization. In 2009, the MetalMapper participated in a live-site demonstration at the former Camp San Luis Obispo (SLO) in central California (Figure 2.1), and in 2010 at the former Camp Butner in North Carolina. The data acquired at SLO and Camp Butner, together with the ground-truth that resulted from the digging provides a unique and timely opportunity for retrospective analyses directed toward improving the performance of this new generation of EMI sensors.

This study was performed as a result of a desire to improve data analysis methods using the lessons learned during the MetalMapper surveys at San Luis Obispo (SLO) and Camp Butner. ROC curves from those surveys (Figure 2.2 and Figure 2.3) are excellent, but we wish to investigate the failures to further understand the limitations and improve the performance for the small portion of UXO that are labeled as non TOI.



Figure 2.1: MetalMapper at San Luis Obispo

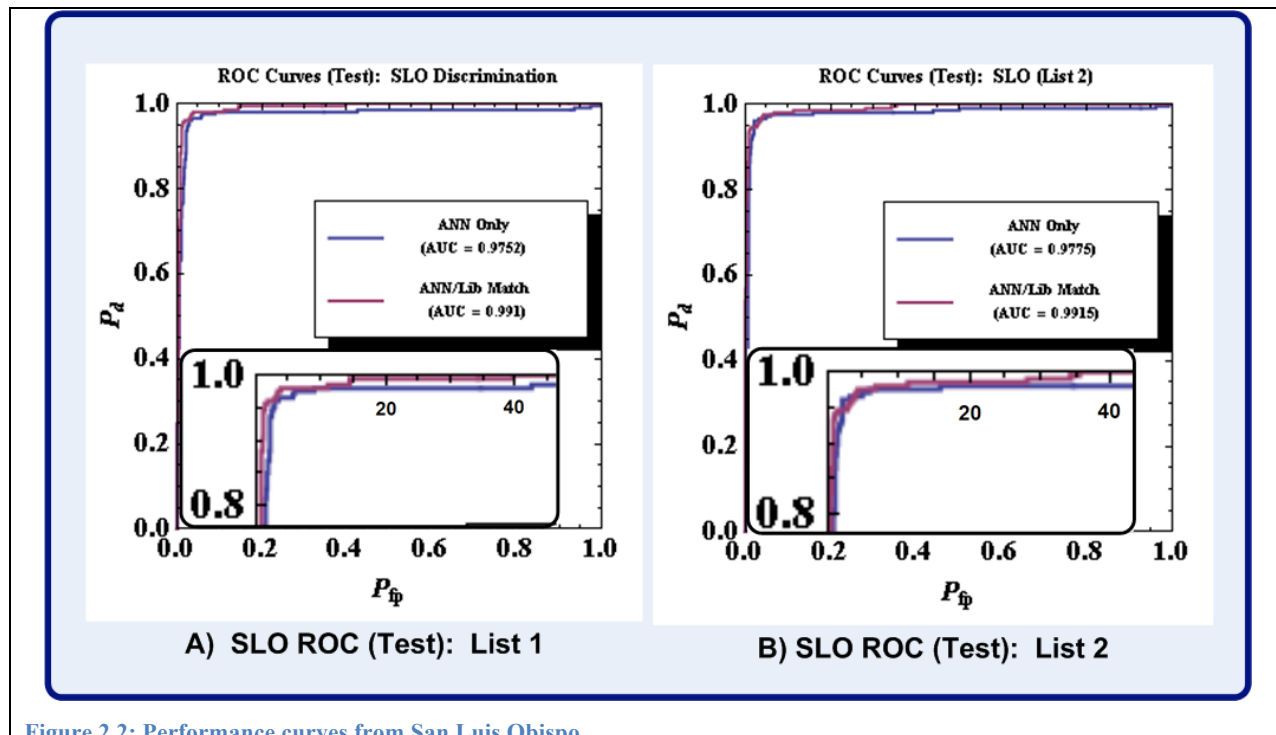


Figure 2.2: Performance curves from San Luis Obispo

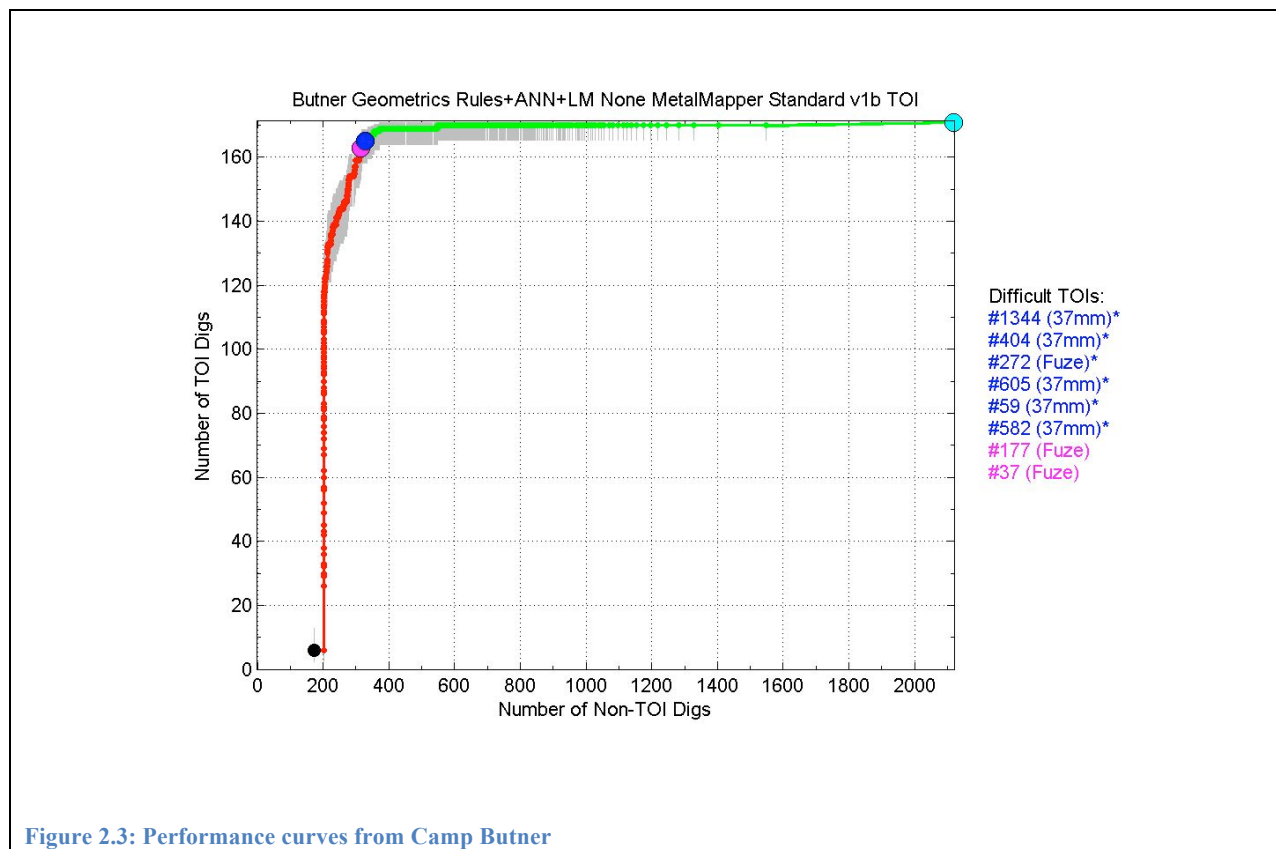


Figure 2.3: Performance curves from Camp Butner

### 3 Materials and Methods

#### 3.1 MMTTargets

A new modeling and inversion program called *MMTargets* was created for this project. Derived from an existing program that was written for the USGS *ALLTEM* system to invert dynamic data [1], *MMTargets* can be used to generate synthetic datasets, or invert data to estimate target parameters. The program has a large number of user-configurable settings that control how synthetic data are generated, or how the program processes and inverts a dataset. These settings are configured in an INI file.

*MMTargets* can model both static and dynamic data. In the forward modeling mode, it provides options to add simulated EM noise to the synthetic data. Different noise levels can be added for vertical and horizontally oriented coils. Uncertainty in positional and orientation are simulated by adding random noise to those parameters before generating data. The inversion routine uses several constrained models when inverting data. The inverted datasets can be a single cued snapshot, multiple queued snapshots, or dynamically acquired data. Furthermore, several different target shape constraints can be enforced; and the results provide better information for classification routines.

*MMTargets* provides flexible and highly configurable inversion routines. In addition to target shape constraints, limits can be placed on the location of the target and its maximum size. These limits are typically set using the extents of the survey coverage and the size limits of the targets at a given site. The target location can be constrained using the size and location (centroid) of the anomaly, or through anomaly focusing efforts such as reduction-to-pole or downward continuation (discussed below). The general inversion sequence is as follows:

1. Determine a reasonable set of initial parameters by inverting a simple 4-parameter spherical model to estimate location and sphere diameter.
2. Perform a constrained inversion using any number (specified by user) of the following models: sphere, oblate spheroid, prolate spheroid, ellipsoid. Users can also specify bounding constraints for each model parameter. This is useful, for instance, when the lateral location of the target is well known.
3. Select new starting models from a list or optionally generate new starting models (Monte Carlo, genetic mutation) and repeat the constrained inversion.
4. Generate principal polarizability curves by separately diagonalizing the data at each time gate. Insure that each polarizability curve has directional continuity in time so that principal polarizability curves do not switch at cross-overs.

The principal polarizability curves produced by *MMTargets* are not a result of the joint diagonalization procedure that is commonly applied in UXO processing. Because the Eigen currents precess as the currents decay, estimating a rotation matrix that best diagonalizes polarization matrixes for all times is not a fair representation of the physical process. An average Eigen-structure does not account for precession. When *MMTargets* generates polarizability curves it diagonalizes the polarizability matrix at each time-gate, and insures that there is directional continuity in each curve from time-gate to time-gate. The usefulness of this method is illustrated by re-processing the data from targets at the Camp Butner demonstration that were

missed in earlier processing. Target 849 (from our anomaly list, program office number 404) is a very typical 37 mm ordnance, but the polarizability curves generated by the inversion program *MMRMP* suggested a plate-like object, while those from *MMTargets* suggest a rod-like object (see Figure 3.1).

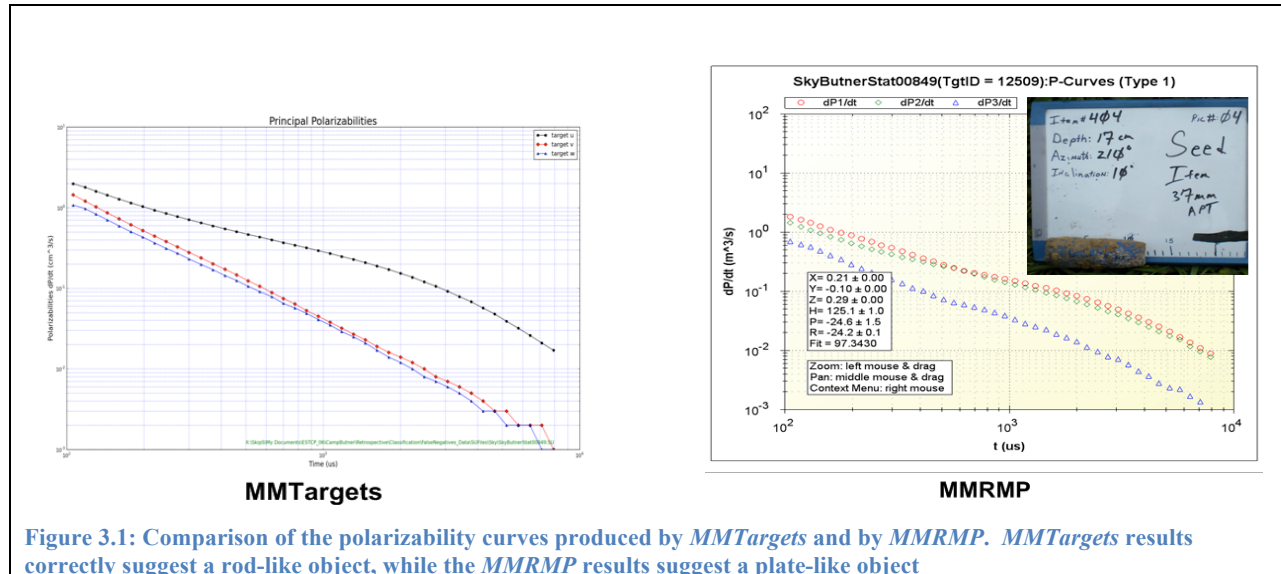


Figure 3.1: Comparison of the polarizability curves produced by *MMTargets* and by *MMRMP*. *MMTargets* results correctly suggest a rod-like object, while the *MMRMP* results suggest a plate-like object

### 3.2 Constrained Single-Target Inversion

*MMTargets* has the capability to employ constraints on its search to find a solution that best fits the data. The user can set constraints that will restrict the resulting target solution to be a sphere (SP), a prolate spheroid (PS), an oblate spheroid (OS), or an ellipsoid (EL). The ellipsoidal solution is, of course, the solution to the inverse modeling that has no constraints. How can we use these constraints as an aid in discrimination? In this section, we will suggest how the results from a constrained solution can be used to form an F-Test statistic the can be used to make a decision about the symmetry properties of a target.

In Section 4.3 we show an example (see Figure 4.9) of how the classic expression of symmetry for a buried target (i.e., a major polarizability curve and two smaller but nearly identical minor polarizability curves) can be compromised simply by the fact that the *MetalMapper* platform is laterally offset from the target. In the case shown in Figure 4.9, we were lucky to have taken a repeat measurement that was located more directly over the target and the resulting extraction of the principal polarizability curves exhibited the classic behavior of an elongated body of revolution. If we don't have a repeat measurement that is well centered over the target, can we develop a feature that is more robust than the symmetry feature ( $P_{0y}/P_{0z}$ ) we used in the optimal array study? In this report we show that the answer to this question is YES.

The *MMTargets* single-target inversion provides a rich set of properties that can be supplied to classifiers. For each model (sphere, prolate spheroid, oblate spheroid, and ellipsoid) the estimated parameters are the target location, principal radii, orientation, and the data misfit. All of these parameters provide valuable information for classification routines. For example, if the data misfit for the spherical model and the prolate model are similar, and the prolate model has a

large aspect ratio, this reduces the confidence that the target actually has a large aspect ratio. If multiple models provide similar misfit metrics, this may indicate that a complex (non-dipole) target is present and more advanced analysis algorithms may be needed.

### 3.3 The F-Test Statistic

Using the capability of *MMTargets* to fit the observed data with 4 different models, 3 of which are constrained to be bodies of revolution (BOR) we can form a statistic similar to an F-Test as it is traditionally applied to regression problems. The statistic is a relationship between the mean square errors of the constrained solution ( $MSE_C$ ) and that of the unconstrained solution ( $MSE_{EL}$ ). For the purposes of this section we shall assume that  $MSE_{EL}$  indicates the *MMTargets* solution for the ellipsoidal model. We will use  $MSE_{SP}$ ,  $MSE_{PS}$ , and  $MSE_{OS}$ , respectively, according to whether the constrained solution corresponds to the sphere (SP), prolate spheroid (PS), or the oblate spheroid (OS). We have experimented with various relationships for the F-Test and the one that works the best for our purposes is

$$F_C = \frac{MSE_c - MSE_{EL}}{MSE_{EL}} \quad (3.1)$$

Presumably, the unconstrained solution will always have an *MSE* that is smaller than those generated by a constrained solution. Thus  $F_C$  is always<sup>1</sup> a number that is greater than 0. In words, the statistic is simply a measure of how much larger the constrained solution error is relative to the fully unconstrained solution. Basically, the idea is that when the  $F_C$  statistic for the constrained solution is close to zero, it suggests that we cannot discount the possibility that the target has the shape indicated by the constraint in question. Thus, the  $F_C$  statistic can be viewed as an indicator of target symmetry characteristics.

### 3.4 F-Test - Synthetic Target Populations

Using the synthetic data set for the 60mm prolate spheroid target (i.e. 250 targets randomly distributed below the *MetalMapper* over an offset of 0.5 meters, see Section 4.3), we have computed  $F_{PS}$ ,  $F_{OS}$ , and  $F_{SP}$  according to Equation 3.1. Figure 3.2 shows the distribution of these three F-Test statistics for spatially identical distributions of a 180mm oblate spheroid (1:3 aspect ratio, Figure 3.2A) and a 60mm prolate spheroid (3:1 aspect ratio, Figure 3.2B). The row parameter is the model constraint moving from prolate spheroid model on the top to sphere on the bottom row. This distribution easily shows the identity of the target population as a whole since only the constraint that corresponds to the model type (i.e., oblate spheroid/prolate spheroid) produces any significant numbers of targets from within the population (250 targets) that have  $F\text{-Test} < 0.1$  ( $\log_{10}F\text{Test} < -1$ ). This is a useful observation since it provides a useful threshold on values of the F-Test statistic below which we may find the F-Test to be a useful and robust indicator of body of revolution symmetry.

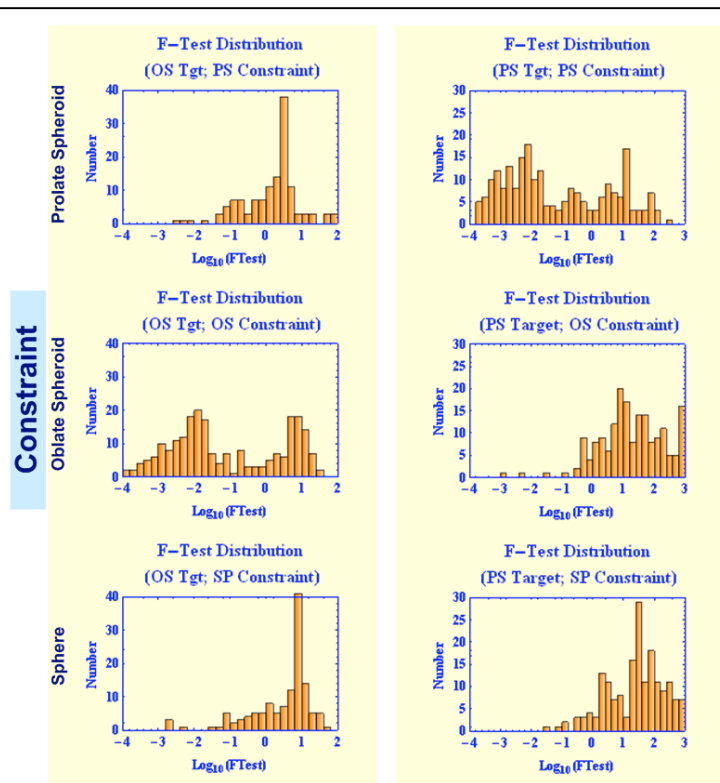
---

<sup>1</sup> In practice, we occasionally find a situation where  $MSE_C < MSE_{EL}$ .

In Figure 3.3 below, we show a number of Log-Log scatter plots in which the F-Test statistic for the prolate spheroid constraint has been plotted as the abscissa.<sup>2</sup> The ordinates are other useful target attributes. With regard to the F-Test, points plotting at values of  $\text{Log}_{10}(\text{FTest}) \leq -1$  suggest that the data for that particular target are fit well by a model constrained to be a prolate spheroid (elongated along the axis of symmetry). We have expanded the scale of the F-Test (horizontal scale) to emphasize the scatter of F-Test values. Two columns of figures are shown. In the left-hand column are plotted points for all 250 targets in the target space (see Figure 4.11). The plots in the right-hand column contain only points falling within the reduced target space. In Section 4.3, we noted that the quality of the parameters extracted from targets located outside the reduced target space (i.e. targets

with offsets greater than 0.4 meters, see Section 4.3) is degraded. This degradation in the quality of the parameter pairs (as indicated by the point scatter) is manifest in the plots here as well. Note that in the scatter plots in the top row of Figure 3.3, both parameters are indicators of rod-like symmetry and in a noise-free case all the points would be located at ( $\text{F-Test}=0$ ,  $P_{0Y}/P_{0Z}=1$ ).

In Figure 3.4A we have taken Figure 3.3A (i.e., top row) and added corresponding plots based on the F-Test statistic for the oblate spheroid ( $F_{OS}$ ), and the sphere ( $F_{SP}$ ) constraints. As one might expect after studying the histograms in Figure 3.2, the plots based on  $F_{OS}$  and  $F_{SP}$  (Figure 3.3B and Figure 3.3C, respectively) show that these 2 constrained solutions have fit errors (MSE) that are more than 10% (0.1) higher than the unconstrained (ellipsoidal) solution.

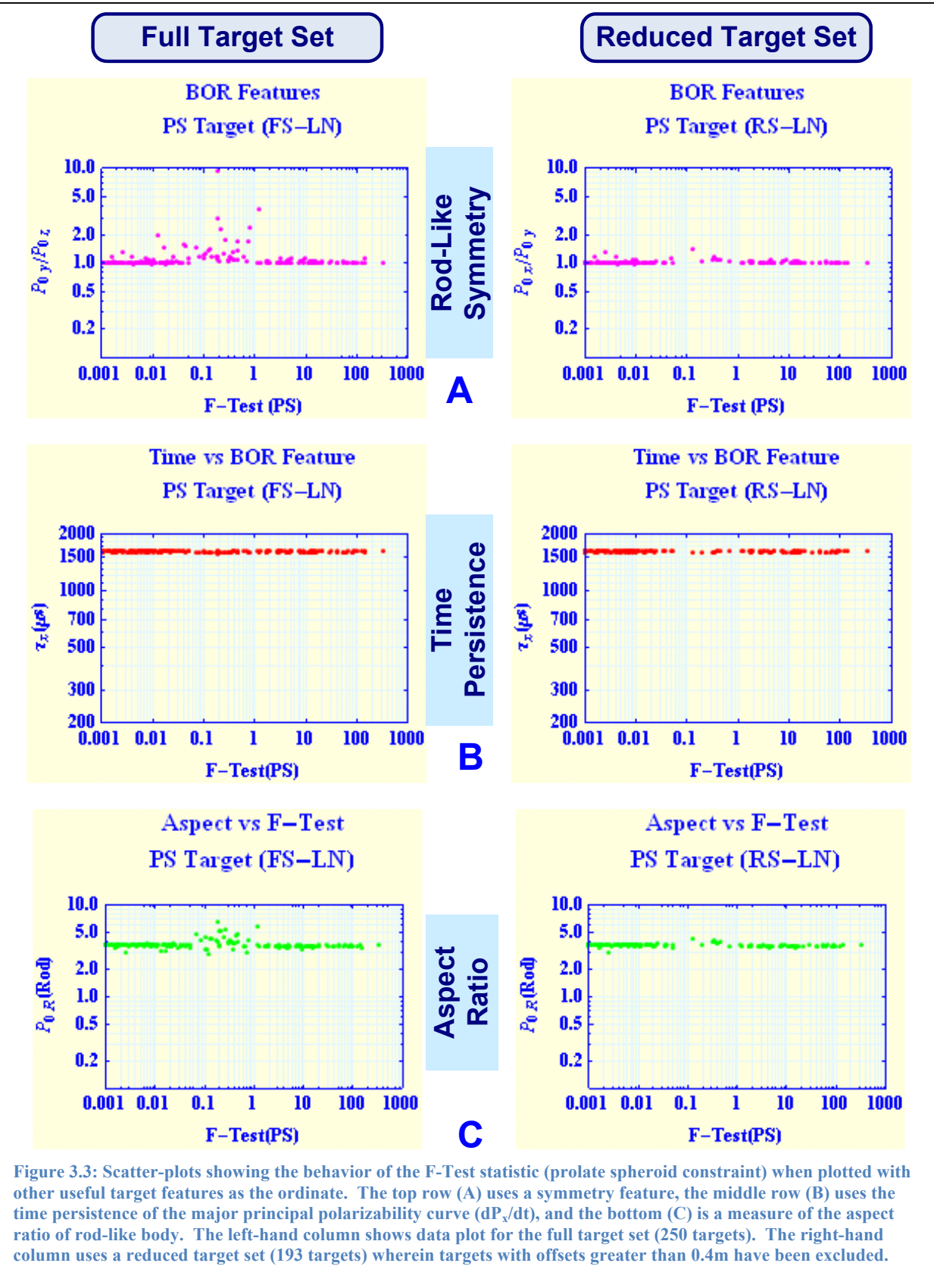


A) Oblate Spheroid Target

B) Prolate Spheroid Target

Figure 3.2: Histograms showing the distribution of F-Test values for 3 constrained solutions generated by *MMTargets*. The targets are a 180 mm oblate spheroid (1:3 aspect ratio), and a 60mm prolate spheroid (3:1 aspect ratio). The constraints are prolate spheroid (PS), oblate spheroid (OS), and sphere (SP).

<sup>2</sup> We focus here on the F-Test (prolate spheroid constraint) because we are usually seeking to identify elongated bodies of revolution (BOR).



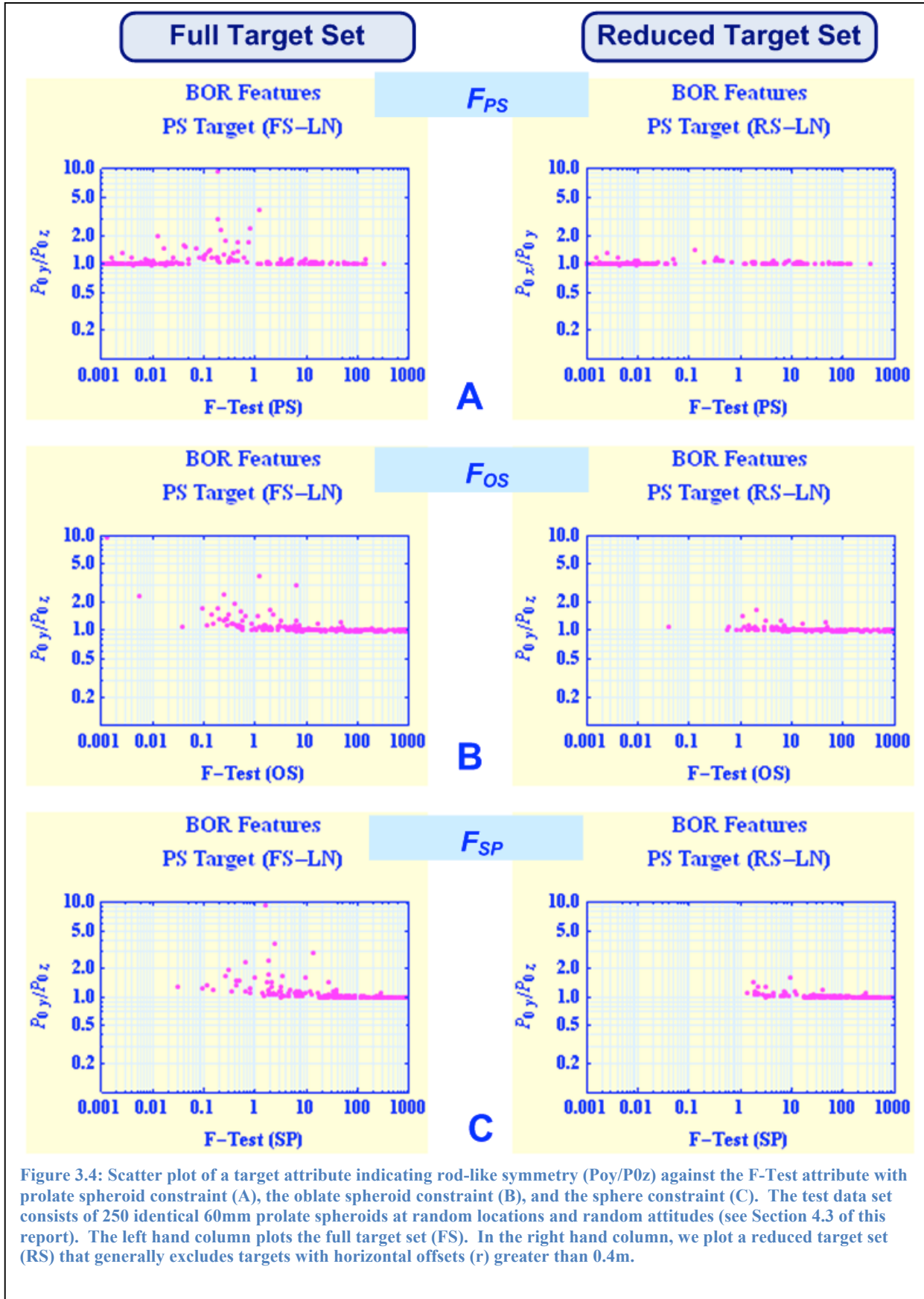
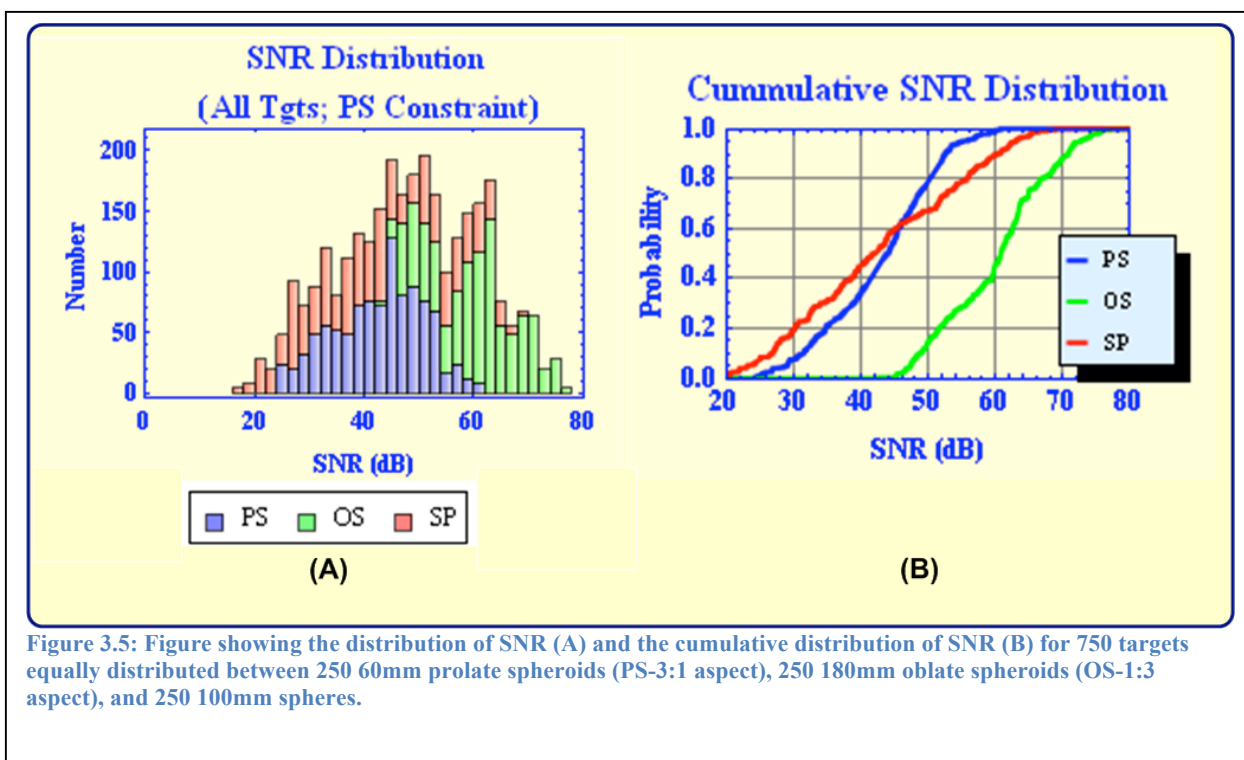


Figure 3.4: Scatter plot of a target attribute indicating rod-like symmetry ( $P_0y/P_0z$ ) against the F-Test attribute with prolate spheroid constraint (A), the oblate spheroid constraint (B), and the sphere constraint (C). The test data set consists of 250 identical 60mm prolate spheroids at random locations and random attitudes (see Section 4.3 of this report). The left hand column plots the full target set (FS). In the right hand column, we plot a reduced target set (RS) that generally excludes targets with horizontal offsets ( $r$ ) greater than 0.4m.

### 3.5 F-Test and the Detection of Rod-Like Targets

The distributions that we display in Figure 3.2 suggest that we can classify a population of the same target type (e.g., rod-like targets such as prolate spheroids or plate-like targets such as oblate spheroids) by looking at distribution of the F-Test for the appropriate constraint. However, it would be more useful if the F-Test can be used to detect individual rod-like (or plate-like) targets. The distribution of F-Test values covers a multi-decade region of  $\text{Log}_{10}(\text{FTest})$  space, so the F-Test cannot be used in a 2-D scatter plot to help identify a cluster of rod-like bodies of revolution with similar characteristics. However, generally speaking, the F-Test for a particular constraint (e.g., prolate spheroid) is minimum when compared with the F-Tests for the two alternate constraints (oblate spheroid and sphere) when the target has “rod-like” symmetry. In this section we use the F-Test as a detector of rod-like bodies.



To demonstrate how such a detector might be applied, we use a population of 3 target types: a) 60mm prolate spheroids (PS); b) 180 mm oblate spheroids (OS); and c) 100mm spheres (SP). There are 250 of each of the target types distributed in an octant of a spheroid centered with the MetalMapper array (3T7C-MM). The distribution of these targets is described in Section 4.3 (see Figure 4.11). We added random noise to the model data consistent with noise levels observed at SLO and reduced by  $1/\sqrt{90}$  to account for stacking.<sup>3</sup> Figure 3.5A is a stacked histogram of the SNR for the entire target population (750). Figure 3.5B shows the cumulative distribution for the 3 targets. The colors refer to each of the 3 different target types. The figure

<sup>3</sup> The standard deviations of the noise were  $\sigma_x=30\text{pT/s}$ ,  $\sigma_y=30\text{pT/s}$ , and  $\sigma_z=15\text{pT/s}$ . This a factor of 10 less than we used for much of the model data in our array study. But in that study we did not account for a stack count of 90.

shows that virtually all the targets have an SNR > 10 (20dB). Therefore, any inability to distinguish target shape from the target data sets used in this exercise cannot be blamed on poor SNR.

It is also interesting to show the distribution of the F-Test ( $F_{PS}$ -prolate spheroid) for the 3 target types. We have done that in Figure 3.6. This distribution confirms what we saw previously in Figure 3.2.  $F_{PS}$  covers a multi-decade domain in log-space and the distribution of  $F_{PS}$  for the prolate spheroid is noticeably more dominant for values of  $F_{PS} < -1$  while the distribution of values for the other two constraints (OS & PS) peaks. The difference is most obvious between prolate spheroid (PS-Blue) and oblate spheroid (OS-Green) targets.

As a simple detector of rod-like targets, we performed the following rule-based test:

1. For each target
2. Sort the 4 solutions according to their respective F-Test values.<sup>4</sup> In all but a few isolated cases, this will place the EL solution at the top of the list of 4 F-Test values. Now, the value  $F_{2C}$  in the second position will have the minimum value of the 3 non-zero  $F_{iC}$ 's.
3. If  $F_{2C} < F_{TH}$ , then the target type is C else type is EL (ellipsoid – meaning not analyzable for shape).  $F_{TH}$  is a threshold value for the F-Test above which we designate the target as not analyzable and default to the EL solution.
4. Loop to 1 until done.

We applied the algorithm above to each of the 750 targets. As ground-truth, we identified prolate spheroids (PS) as the positive decision (1), and oblate spheroids and spheres and negative decisions (0). We used the fit statistic (MSE) value as means of ordering each decision. That is, a solution in which  $F_{2C}$  corresponds to the PS constraint and has a low value for the MSE of the solution is considered a rod-like object with high confidence. Likewise, if  $F_{2C}$  corresponds to either an OS or SP with a low value of the solution MSE the target will be considered to be NOT PS with high confidence. Figure 3.7 is a ROC showing the performance of the F-Test for detection of rod-like objects. We

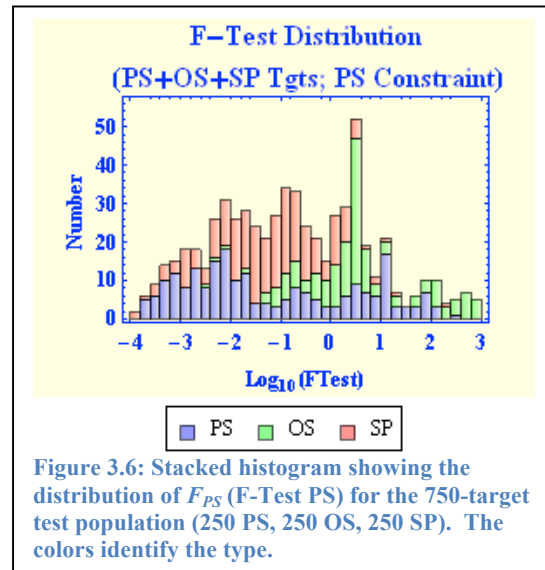


Figure 3.6: Stacked histogram showing the distribution of  $F_{PS}$  (F-Test PS) for the 750-target test population (250 PS, 250 OS, 250 SP). The colors identify the type.

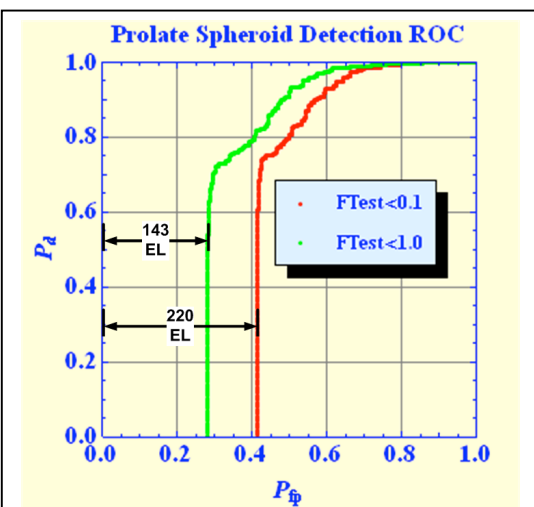


Figure 3.7: ROC curve showing the performance of the F-Test (PS) for detection of rod-like bodies of symmetry (BOR). The parameter is an F-Test threshold value. All targets with F-Test values larger than the threshold are designated as non-detectable (ND). The offsets of the 2 curves indicate the number ND's found for the indicated threshold.

<sup>4</sup> We set the F-Test for the unconstrained (EL) solution to 0.

evaluated the ROC for 2 different values of the F-Test threshold. The results show that we can detect approximately 75% of the prolate spheroid targets with a false alarm rate of  $P_{fp}=0.29$ . Most of the false alarms are associated with targets that are not detectable (ND) because  $FTest > F_{TH}$ . We have not calculated the corresponding ROC for the *reduced* target set. It will be interesting to see whether the false alarm rate is reduced significantly in that case. It is also worthy of note that reducing the F-Test threshold (from 1.0 to 0.1) does not appreciably change the performance of the basic rod-like prediction. The only significant difference between the two ROC curves is the offset due to the need to designate 79 more targets as ones that we cannot detect.

The primary reason for the broad F-Test distributions is noisy data, which produces a noisy objective function. While the noise is small enough to permit reasonable inversion results, the noise causes a number of small local minima in the same vicinity of the reported solution. The local minima in the vicinity of the solution all have similar MSE values, and some will likely have lower MSE values than that of the reported solution. It is anticipated that smoothing the objective function will reduce these difficulties and reduce the breadth of the F-Test distributions. This is recommended as future work.

More experimentation is required to perfect the procedures for exploiting the information in the F-Test values. Clearly, we need to evaluate the ROC for larger values of the F-Test threshold. And we also need to evaluate its use on real data. We have the data sets (e.g., SLO, and Butner). But we need to invert each data set with *MMTargets* before we can extend this type of analysis to a real data set.

## 4 Results

### 4.1 Improved Target Detection (Task 1)

#### 4.1.1 Introduction and Background

The objective of this work was to improve upon the process of mapping and picking targets for cued re-acquisition. The method was proposed and developed because authors believed there is a better way to pick and select targets for cued re-acquisition.

The fundamental input data for the process is dynamic survey data that is collected along survey lines. This data is typically different than static data used for target classification in that it typically is for just one transmitter loop (the Z-axis loop), it has short data-point collection times and short decay-transient times. The data collection intervals for each data point are typically 0.1s and the signal repetition rates are typically 90 or 270 Hz (2.7ms or 0.9ms transient decay times).

The objective of analysis of the data is to produce a list of targets, cued for re-acquisition. The process involves selection of spatial anomalies in the data and production of the cued-target list. There is usually no shortage of spatial anomalies that can be detected. But re-acquisition of all of the anomalies would be cost-prohibitive. Therefore, typically a threshold is included in the process to select cued targets from a map of all possible targets. The threshold can be set by ancillary measurements to assure selection of all anomalies for the ‘weakest’ target of interest, based on historical evidence of site usage or exploratory surveys.

#### 4.1.2 Traditional method

Simplified, the traditional method plots signal amplitude on a 2D map and picks peaks of signal level.

- Sequential data points are collected as the system is moved across the ground. A data point consists of one or more signal amplitudes.
- The signal amplitude is plotted at a point on a map. For traditional EM61 data, signal amplitude is plotted at the center point of the loop at the time that each data point is collected. Dynamic surveys with MetalMapper have been similar, as described below.
- The data are processed by edits, filtering, background subtraction, coordinate analysis and orientation corrections, and other considerations.
- The data points are then plotted on a 2D map.
- The map is ‘gridded’ and ‘contoured.’ This step and the previous two steps are often iterative.
- Peaks are picked from the 2-D contour plot. Picking of peaks usually involves selection of an amplitude threshold – only peaks greater than the threshold are selected. The targets’ X-Y locations are taken to be the coordinates of the peaks and the target amplitudes are taken to be the amplitudes of the peaks.

#### 4.1.3 MetalMapper refinements to traditional method

MetalMappers were used to collect dynamic data over the San Luis Obispo and Camp Butner sites.

When ‘traditional method’ maps are made from MetalMapper data, the method just discussed is slightly more complicated because the MM has seven small sensors that sense the magnetic field at seven separate points within the Z-transmitter loop. For shallow targets, as the MM array is moved along a line, the signal amplitude from each sensor reaches a peak when the sensor is nearest the target<sup>5</sup>. On a map, when the sensor’s signal amplitude is plotted at the coordinate of the center of the antenna array, the sharp, narrow peaks of signal amplitude for each sensor are spatially offset with respect to one another because the sensors in front reach the target first. We would rather that the peaks all line up with one another since they are each sensing a single target. Contrarily, for a deep target, the peaks from all sensors are broader and appear nearly aligned.

Because of this, for MM data, we have historically used either of two methods to produce a map for target detection and selection.

1. The 5IZ method: We used the five innermost sensors and computed the average signal from the Z coils of those sensors. This value is plotted at the center of the antenna array since the receivers are symmetrically distributed about the center. This method solves the peak-offset problem by producing an average signal that is equivalently from a larger loop and that has a broader peak. This method approximates the signal that could be received using an EM61 because we are using only the Z component, like an EM61 sensor, and because we are averaging the signal over a spatial area more nearly the size of an EM61 receiver loop.
2. The ‘Split Cube’ method: In this method, the data from each cube is plotted at the coordinate where the sensor is located at the time of the data point. Since each cube follows its own track as the antenna array is moved across the ground, this method essentially ‘splits’ a single survey line into seven survey lines. The data from the seven lines are contoured on a 2D map as usual. For shallow targets this method works reasonably well because it aligns the peak offsets along the profile as discussed just previously. However, for deeper targets, a sensor’s peak response may be nearer to the center of the antenna array than to the coordinate of the sensor. So, one refinement to this method has been to use an effective coordinate for each sensor that is part way between the center of the antenna array and the sensor itself. Within this method we have used either the Z signal from each sensor or the magnitude (M) signal from each of the seven sensors, where magnitude is the orthogonal summation of the Z, Y, and X components

---

<sup>5</sup> This is not precisely true because the target response is a function of the amplitude of the primary field. For shallow targets the primary field amplitude is largest near the edge of the transmitter loop. Thus signal amplitude at a given sensor is a function of the distance of the target from the edge of the transmitter loop and the distance of the sensor from the target.

#### 4.1.4 Objective of this work and basic considerations

In this project we attempt to improve upon the traditional method of mapping and target picking. We believed from observation of significant amounts of data improved maps could be made. For example, it stands to reason that a small shallow target can be identified because it shows a signal anomaly in only two or three sensors that pass near it, while a deep target can be identified because it shows a signal anomaly of roughly equal magnitude in all seven sensors. In both cases, the signal amplitude might be about the same; but we know that the deeper target has a substantially larger moment, and that this moment becomes amplified even more if we consider the size of the transmitted field that activated the target.

The traditional method of producing a cued-target list can be thought of as a two-step process. In the first step, a data point is calculated from each measurement point and assigned a coordinate on the map – this data point is not yet a pick because no criteria are applied. Traditionally, this data point is assigned the coordinate of the center of the antenna array and the amplitude of the received signal. The results from all of the data points are plotted and the map is gridded and contoured. Finally, targets are picked from peak amplitudes of anomalies on the 2D map<sup>6</sup>. This second step is the picking process where the criterion is target amplitude.

The 5IZ method for the MetalMapper is an identical process where the amplitude of the target is taken as the average Z-component for the five innermost sensors. The ‘Split Cube’ method is similar except that seven targets are *picked* from the data. Each of the targets is *picked* at the location of an individual sensor and each is assigned the signal amplitude at that sensor. In either case, previous processing of MetalMapper dynamic data has been not dissimilar to traditional methods, nor has it been a substantial improvement.

#### 4.1.5 Enabling and limiting concepts

An important point is that the MetalMapper collects vector data at each sensor. Yet the methods used to analyze the San Luis Obispo and Camp Butner dynamic surveys did not make use of the MetalMapper’s vector capabilities. Following the reasoning above, our initial objective is to pick zero or more tentative targets from each data point and to assign each target a coordinate and a scalar magnitude. Our final objective is to examine the map of scalar magnitudes and to pick cued targets for reacquisition. So to take advantage of the MetalMapper’s vector capabilities, somewhere within the method we must produce one or more scalars from one or more vectors. The work herein has used physics-based approaches to use the vector data produced by the MetalMapper. This is the fundamental enabling concept of the proposed method.

This work has been limited to following a procedure analogous to the conventional two-step process. That is, we are considering data points along a line independently of one another in the first step, and considering all data points together in the second step. The proposed method provides a substantial improvement to the first step and changes the methodology of the second step. In the first step we select zero or more targets from each data point and assign each target a coordinate and amplitude. But the selections are made (using a minimum correlation factor

---

<sup>6</sup> This of course is a grossly simplified description since editing, subtracting backgrounds, smoothing and filtering, companding, and plotting are usually often complicated activities. In addition, the process of picking peaks from the 2D map can become very complicated.

criterion), they are assigned an estimated coordinate, and their amplitude is a function of their depth and the magnitude of the primary energizing field at that coordinate. It turns out that the picks tend to group or cluster so well that a gridded contour map of those picks is not helpful. So instead, the second step is one of applying a clustering algorithm to produce the final set of cued targets, instead of gridding and peak-picking.

The number of tentative *targets* from an individual data point is an important factor. A traditional survey produces exactly one data point from each measurement point. Our traditional *split cube* method produces seven data points from each measurement point. The method proposed herein produces zero or more *targets* from each data point. The number of possible targets is fundamentally related to the diversity of the data. The MetalMapper measures seven 3-component signals -- 21 components that are not completely independent. So an important question is *How many targets can be effectively separated and detected from one data point?*

Given uncertainties and noise in the data, and given our experience in experiments in performance of this work, we believe the practical answer is one or occasionally two or rarely three for the shallowest targets, and only one for any deeper target. If there are interfering targets, the proposed method may be able to detect that fact but cannot separate the multiple targets, if for no other reason than the lack of diversity in the data.

#### **4.1.6 Requirements placed upon our methods**

In the method we have chosen, we divide a volume below the sensor array into a set of voxels. Once we do this, our next task is to produce a statistic for each voxel that relates to the likelihood that the voxel contains a target. Then our final task is to choose which voxels are most likely to contain a target and to assign values to those choices that are related to the moment of the target. Note that this method is a 3D method, as differentiated from the conventional 2D method. This complicates choices for data visualization. For most of this work we have generated groups of plots to visualize the data. The plots are shown as horizontal 2D maps for each *layer* of voxels.

We would like a method that produces maps with the following characteristics:

1. A plot of some statistically constant value when there are no targets present. The statistically constant value is related to the noise level (assumed statistically constant) from each of the sensors and we assume that this noise level is statistically the same for all of the sensors. The plotted value should neither increase with depth nor increase with distance from the sensors. It should show a ‘background’ map that is random but low level, like the noise level from the sensors. Since a map for a given data point is produced from the data for only seven sensors, an individual map cannot show randomness very well. The randomness must be perceived from sequences of maps.
2. A plot that shows an increase of the plotted value when signals from one or more sensors rise above background levels. We would hope that the plotted value shows some indication of the target’s moment. Because a target’s moment increases by R-cubed for a constant observed signal, a better requirement is that the mapped value be monotonically related, but not necessarily proportional, to the observed signal.
3. A plot that shows an increase of the plotted value for voxels that are more likely to contain a target. This likelihood is a function of the agreement between observed signals from two or more sensors. If the observed signals from two or more sensors correlate well with the signals that would be produced from a target in a cell under consideration,

then a larger value should be plotted. These considerations must be true both laterally and vertically, because we assume that we are going to pick one or more targets from the maps.

4. A smaller anomalous area of increased values when the target is shallow and a larger range of increased values when the target is deep. This correlates to the idea that a shallow target can have a signal that couples into only two or three sensors, whereas, a signal from a deep target will couple into most of the sensors.

#### 4.1.7 Progress of our work and lessons learned

The requirements we just stated were partly a result of our work as it progressed. In our studies we pursued the following methods.

##### 4.1.7.1 Sensor groups and forward computations

We originally proposed to use pairs and/or groups of sensors to compute an apparent target. That computation was to be followed by examination of apparent targets to determine if any them were likely to be real and if so, how big they were. This approach was based on idea that fundamentally two sensors are capable of detecting a target, its position, and its moment – six measurements ( $B_{1x}, B_{1y}, B_{1z}, B_{2x}, B_{2y}, B_{2z}$ ) and six unknowns ( $x, y, z, M_x, M_y, M_z$ ). The original concept was that shallow targets could be detectable by just two sensors whereas deep target would require all sensors.

This method was problematic in terms of defining and using sensor groups. We experimented with using two specified sensors for specific triangular areas in shallow layers, and all sensors for the whole lateral area for deep layers, and other combinations for medium depth targets. But given that a target's depth is unknown at the outset, selection of sensor groups is not straight forward.

Furthermore, we were unable to develop an analytical method for the solution to the two-sensor problem. And the three-or-more cube problem is over-determined and requires some method of minimization.

Looking at sensor groups convinced us that a better approach was to use all sensors, all of the time, but to weight the contribution of each sensor in computations so that closest sensors contributed most to any result. Given that we were performing computations for a given voxel, we could compute the distance to each sensor and weight its contribution to a result as a function of its distance. Given that a magnetic dipole field decreases as  $1/R^3$  it seemed intuitive to establish weighting as  $1/R^3$ . That way, for shallow targets, the closest one or two cubes would dominate the solution but for deep targets all sensors would contribute to the solution. Furthermore this approach allows a kind of continuous transition between use of just a few sensors and use of all sensors.

##### 4.1.7.2 Method of Apparent Moments

This second approach and the approach that required a substantial amount of effort on this project we called the method of *Apparent Moments*. However, this method proved to be severely limited and was not implemented in the final analysis. It is described briefly here.

Our overall objective in any method was fundamentally to determine position and apparent moment of a target (or targets) given one measurement of MetalMapper data. Assuming a dipole target, and assuming a known position of that dipole, computations of its magnetic field are

simple and straight forward. Importantly, given the position of target, and given its magnetic field, its moment (magnitude and orientation) is a simple forward computation.

Given this, with the volume below the array divided into a grid of voxels, our approach was to compute an apparent moment in each voxel for each signal observed at the seven sensors. Given seven sensors, the result was seven apparent moments in each voxel. From here, the concept was to examine the apparent moments in each voxel. A good target would produce seven moments all having same orientation and magnitude whereas noise would produce seven moments with random orientations and magnitudes. So the objective became one of developing a method to determine whether the seven *apparent* moments matched each other or whether they did not.

We computed a mean apparent moment in each voxel as a weighted average of the seven apparent moments. Weighting was chosen as discussed above to amplify the contribution from closest sensors to a voxel under consideration. This produces an apparent mean moment in each voxel but it does not say which mean moment is highest quality. If the largest moment is selected, the deepest voxels are almost always chosen because they have the largest mean moments even though the individual moments do not agree. To select a ‘best’ mean moment requires computation of a quality factor.

We developed a quality factor based on the correlation/matching of individual apparent individual moments in a voxel. We optionally included another quality factor based upon whether or not the apparent moment(s) in a voxel had an expected orientation – i.e. whether or not they matched the orientation of the primary field for that voxel. We experimented with methods to compute these quality factors and to select the voxel(s) with the best quality.

None of the methods we tried performed particularly well. A constant difficulty with the method was that dipole moments computed for deep voxels were (not unexpectedly) always larger than moments computed for shallow voxels. It was difficult to compute quality factors that robustly picked targets. We found that the signal-pattern correlation method in the next section consistently outperformed the apparent moment method. Nevertheless, the apparent moment method allows a user to pick targets without assuming that the target dipole is aligned with the primary field. If this issue becomes more important than believed, the apparent-moment method should be re-visited.

We obtained the best results with a method that suggested itself during this work and is described next.

#### 4.1.8 Method of Signal Pattern Correlation

We call this method *Signal Pattern Correlation* because it employs a simple correlation of the observed signal vectors with a set of reference signal vectors. The method might be called *Pattern Matching* or even *Matched Filtering*.

##### 4.1.8.1 Computations

This method is based upon a correlation of a set of reference signals with the observed signals for each of the seven sensors. We divide the volume below the antenna array into a set of cells or voxels and then perform a correlation for every voxel in our test volume. We then choose zero or more voxels having highest correlations and/or largest signal levels.

We assume the traditional dipole model and compute the signal that would be observed at each sensor from

$$\mathbf{S}_{ijkl} = \frac{1}{R_{ijk}^3} \mathbf{g}_{ijkl} \mathbf{M}_{ijk} + \mathbf{N}_l \quad l=1,2,\dots,7 \quad (4.1)$$

where  $\mathbf{S}_{ijkl}$  is the signal at sensor  $l$  from an object at location (i,j,k), and

$$\mathbf{g}_{ijkl} = 3\mathbf{r}_{ijkl}\mathbf{r}_{ijkl}^T - \mathbf{I} \quad (4.2)$$

where  $ijk$  are the indices of cell containing the target,  $\mathbf{R}$  is the vector from the cell at  $ijk$  to the sensor  $l$ ,  $R$  is the magnitude of  $\mathbf{R}$ ,  $\mathbf{r}$  is the unit vector aligned with  $\mathbf{R}$ ,  $\mathbf{M}_{ijk}$  is an arbitrary moment representing the target, and  $\mathbf{M}_{ijk}$  is shown with indices to indicate that it is located in cell  $ijk$ . We assume that a target of interest will have the same orientation as the primary field. Thus

$$\mathbf{M}_{ijk} = M\mathbf{T}_{ijk} \quad (4.3)$$

where  $\mathbf{T}_{ijk}$  is the primary transmitter field at the cell  $ijk$ ,  $T$  is its magnitude, and  $M$  is a constant representing the magnitude of the target. The assumption that the target moment has the same orientation as the primary field is correct in early time channels for any target and correct for all time channels for a spherical target.

To compute reference vectors to be used for correlation, we set  $M = 1$  and compute a reference signal  $\hat{\mathbf{S}}_{ijkl}$  from Equation 4.1. Then we correlate the observed signal  $\mathbf{S}_l$  with  $\hat{\mathbf{S}}_{ijkl}$ . We chose a dot product as the method of correlation. We note that a dot product of seven 3-component vectors is the same as a simple correlation of 21 signals with 21 references. The correlation factor for a given voxel is

$$C_{ijk} = \frac{1}{\sigma_{ijk}\sigma_s} \sum_l (\hat{\mathbf{S}}_{ijkl} \cdot \mathbf{S}_l) \quad (4.4)$$

where  $\hat{\mathbf{S}}_{ijkl}$  is the reference vector for cell  $ijk$  and sensor  $l$ ,

$$\hat{\mathbf{S}}_{ijkl} = \frac{1}{R_{ijkl}^3} \mathbf{g}_{ijkl} \mathbf{T}_{ijk} \quad (4.5)$$

$$\sigma_{ijk} = \sqrt{\sum_l |\hat{\mathbf{S}}_{ijkl}|^2} \quad (4.6)$$

$$\sigma_s = \sqrt{\sum_l |\mathbf{S}_l|^2} \quad (4.7)$$

Note that  $\sigma_s$  is like the root-mean-square (RMS) value<sup>7</sup> of the signals at seven sensors and that  $\sigma_{ijk}$  is a normalizing factor to cause the maximum correlation to be unity.

If an actual target is in the cell  $ijk$ , then

$$\mathbf{S}_l = M\mathbf{S}_{ijkl}, \quad C_{ijkl} = 1, \quad \text{and} \quad M = \frac{\sigma_s}{\sigma_{ijk}} \quad (4.8)$$

This equation gives the moment of a dipole if it is actually located in cell  $ijk$ .

<sup>7</sup> Actually,  $\sigma_s$  is a ‘root-sum-square’ (RSS) value. In this case RMS and RSS are related by the constant factor  $\sqrt{7}$  for seven sensors.

Note that because the reference signals are scaled by  $1/R^3$  in Equation (4.1), the weighting discussed earlier, to use only nearest sensors for shallow targets, and to use all sensors for deep targets, is implicitly included.

#### **4.1.8.2 Selection of Targets**

Once the values above are computed for each voxel, the next step is to select the ‘best’ voxel(s) as the one(s) most likely to contain a target. For this we examine the correlation coefficient knowing that a perfect correlation is +1. Also note that for a single data point, we have a single realization of the received signals, and that the effective amplitude of the received signals is  $\sigma_s$ . Thus we have two parameters that can be used to decide whether target(s) are present. The first,  $\sigma_s$  is an enabling indicator – if the signal amplitude is small, such as ‘background’ then we know there are no targets present even if noise should indicate a high correlation coefficient in any voxel. If the signal amplitude is large enough, such as above a threshold, then we know to examine the correlation coefficients in all of the voxels to determine where the target(s) might be.

One method is to select the best voxel in the entire volume of voxels – the voxel that had the largest correlation coefficient. This method is modified by selecting no voxels if the best voxel was on the edge (or surface) of the voxel array – the justification is that if the correlation was spatially increasing toward any edge or surface of the array, then the maximum voxel might be located outside the array – therefore the target is not located within the voxel array. For discussion purposes herein we have named this method the *best-pick* method.

A second method is to select any voxel having a spatially local maximum correlation coefficient. Any voxel under consideration has 26 neighbors (a 3x3x3 array in which the voxel of interest is in the center). Therefore the method requires that all 26 neighbors have a correlation coefficient less than the center voxel. A characteristic of this method is that it is capable of selecting multiple targets from the data. We have named this method the *multi-pick* method.

Both of the methods can be modified by requiring not only that the signal level  $\sigma_s$  be above a threshold, but also that the correlation coefficient  $c_{i,j,k}$  be above a threshold. These thresholds are a key characteristic of the method. They allow completely automated selection of targets with deterministic specifications selection parameters, similar to the conventional specification of a threshold when picking peaks from a contour map.

Once a target is selected, its moment is computed from Equation 4.8. Note that selection of targets depends only on signal amplitude and on correlation of the signal pattern to an expected pattern. In this regard it is not completely dissimilar to the traditional method of signal contour mapping and picking peaks. However, this method adds and allows an important refinement to the traditional process. Once a target has been picked, its moment is determined. So a second level of target picking can be done by examining moments of the targets. The conventional method never produces the moment of the targets nor does it estimate target depth. This new method allows the analyst to at first pick *all* targets having adequate signal amplitude at the sensors, and then to substantially reduce the number of picks based on target moment, *instead of* signal amplitude. The second step improves on the issue of picking too many near-surface targets at the expense of missing deeper targets.

This method tends to display points on a map that cluster into groups because a given target can be detected in many individual data points. Whereas in the traditional method all of the

detections are smeared along a survey line, in this method the detections tend to cluster in groups directly at the target. We found that if we allowed ‘detections’ based on small, noise-only signals, the results tended to scatter as expected. But when we plotted the resulting moments on a map, the (scattered) deep *targets* dominated the map because of their larger amplitudes. Therefore we employed a signal threshold discussed earlier. This causes many areas on the map to have no data points. The maps tend to have spatially small clusters of points directly where a target is located and not many points elsewhere. Thus the traditional method of gridding and contouring is not very helpful. Instead, a method is needed to pick clusters of points and to determine the mean location and value (*moment* in this case) of each cluster. Of course a clustering algorithm becomes complex to determine where there are clusters and which points belong to each cluster, in the same way that picking peaks from a 2D map becomes complex to determine which maxima are independent peaks. A simple clustering algorithm was implemented for this study but is not part of the proposed method. If future work is done with this method, selection and implementation of better clustering algorithms will be part of that work.

#### 4.1.8.3 Implementation and Performance

The method was implemented in two ways. The second method below is the most important because its result is to improve the process of producing a cued target list. However, the method is also useful for user/operator feedback, in real time, in the field. That implementation is presented first.

#### 4.1.8.4 Real-time detection and dancing arrows display in program EM3D.

The MetalMapper data acquisition program EM3D has traditionally provide a display known as *dancing arrows*. This display has been used to center the MetalMapper over a target because the arrows tend to point directly toward the target. The operator can also see targets passing by the array through observation of the *dancing arrows*.

The correlation detection method in this report was implemented in EM3D to add detected targets to the *dancing arrows* display. The method selects zero or more criteria discussed above and plots the target(s) along with the *dancing arrows*. The detected depth is displayed as a color and the magnitude of the moment of the target is displayed as symbol size. The result is that the user can watch targets pass by the array, and will have estimates of their size and depth.

The method is implemented as an array of voxels that is 1.56m wide with cells that are 6.5cm square and 20cm tall. The center of the first cell is positioned 5 cm above the center of the Z-antenna and receiver array so that the first layer of cells not on the surface of the voxel volume is 15cm below the center of the Z antenna, or roughly ground level. The voxel array contains 25 x 25 x 7 cells. The effective volume of useful cells is 1.43m x 1.43m x 100cm, from 15cm to 115 cm below the antenna array. The entire array contains 4375 cells and can be run for every data point collected by EM3D, without slowing down data collection, when data points are collected at 0.1s intervals. Tests were not made to determine how much faster than this the routine runs.

Samples of screen shots from EM3D are shown in Figure 4.1. It shows the *dancing arrows* panel. The pictures are shown from real data collected along Line 1, the westernmost line, of SLO. The target in the left hand panel is one of the smaller targets near the south end of the line. The target in the right hand panel is the larger anomaly about mid-way and to the east of the line.

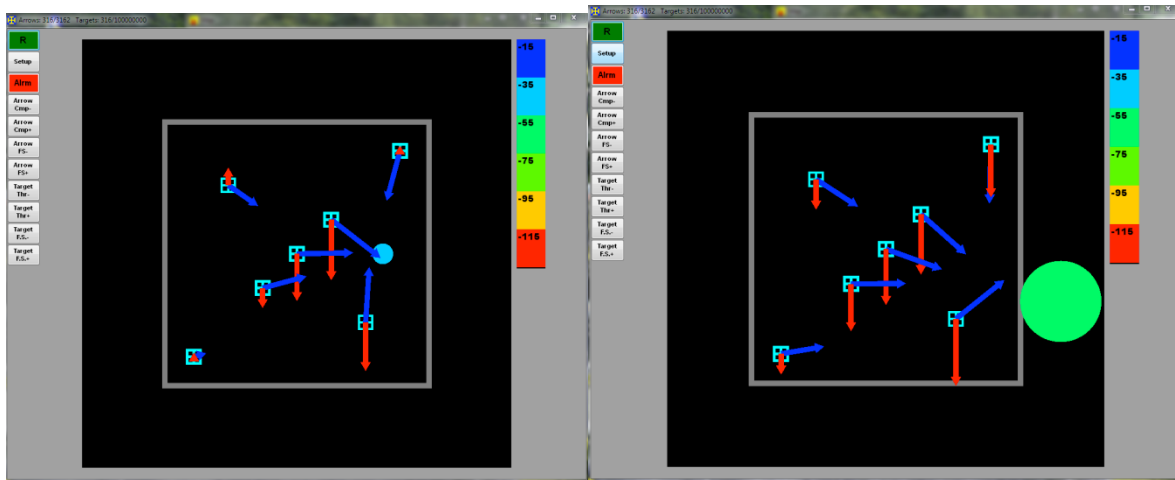


Figure 4.1: Screen shot pictures of implementation in EM3D. The left panel shows a target at a depth of 35cm passing under the array. The right hand panel shows a much larger target at a depth of 75cm or so passing just outside the array.

#### 4.1.8.5 Mapping detection and display in Oasis montaj

The method has been implemented as a GX-Net add-on routine for Geosoft's Oasis montaj. The implementation contains both the *best-pick* and *multi-pick* methods.

In Oasis montaj, it is convenient to show the best pick for each data point and to display that data beside the rest of the data for each fiducial. Displaying multiple picks per data-fiducial requires multiple channels or an array channel with variable length. Therefore multiple picks are entered in a new line or new group in Oasis montaj. The user must select either original survey lines or the one *multi-pick* line/group when plotting picks on a map.

The method allows the user to specify the overall size and cell size of the voxel array; and it allows the user to specify thresholds. The user interface is shown in Figure 4.2.

The implementation returns correlation coefficient, coordinate offsets and moment for the target(s) selected. Within montaj, the coordinate offsets, which are with respect the cart's coordinate system, are manipulated according to cart heading and orientation, to produce a ground-referenced coordinate for each target.

Within montaj, the user must compute absolute coordinates for the target, given cart-relative coordinates of the target(s) and orientation of the cart. For this study, a simple correction based on cart heading was used, where cart heading was the computed true heading, using GPS coordinates.

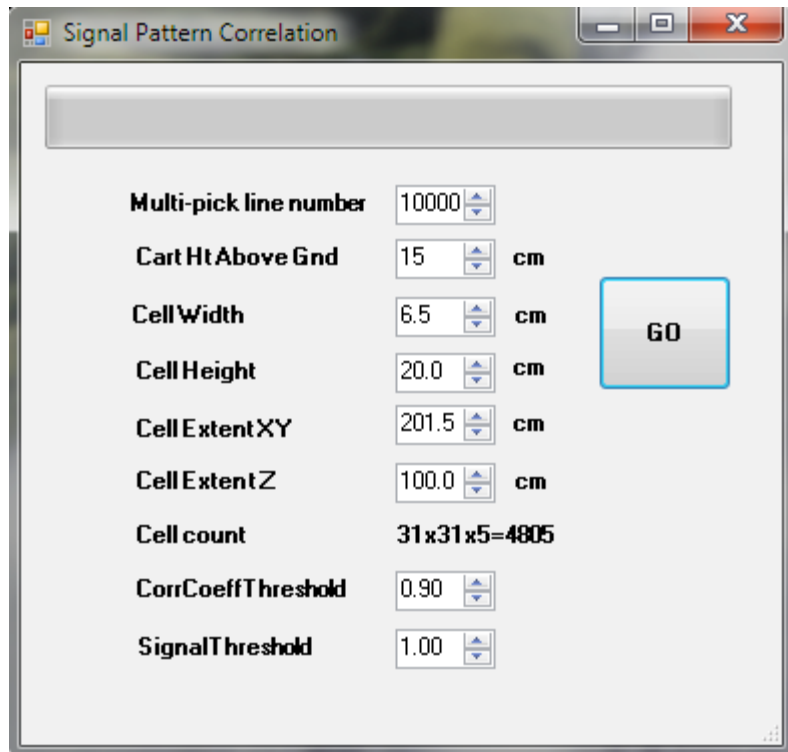


Figure 4.2: User interface for Signal Pattern Correlation within Oasis montaj.

Performance of the method is shown in Figure 4.3. Results showing the intended use of the method are shown in the next section on Results.

Preparation of data within montaj is a non-trivial process. Coordinates must be imported and converted from Longitude/Latitude to UTM, data must be edited, orientation data must be filtered, and EM data must be gated or other-wise manipulated to produce scalar values at individual coordinates, so that it can be plotted on a map.

Figure 4.3 shows application of the method along one line. This line is the westernmost line in the figures shown later. The top panel shows the traditional 5IZ signal in green and the root-sum-square (RSS) signal. Although labeled ‘SignalRMS’ and ‘Avg5IZ,’ these signals are actually the sum of 5 inner Z signals and the root-sum-squares of the seven sensor signals.<sup>8</sup>

---

<sup>8</sup> Work on this method leads the author to wonder why we have never (traditionally) used the RMS or RSS signal to produce the contour maps for conventional peak picking. It appears to be a reasonably robust signal that should produce a better map than the methods we have previously used.

Thus, the orange trace is the signal,  $\sigma_s$ , in Equation (4.7). The other four panels show computations from the method for the *best pick*. The second panel shows the correlation coefficient and the dipole moment for the best pick. For these plots, we used an RSS signal threshold of 1.0 and a correlation coefficient threshold of 0.90. The bottom three panels show the *delta* coordinates, i.e. the location of the detected target coordinates in the cart reference system. For a perfect detection, we expect to see a constant X coordinate that is the lateral offset of the target on the cross-track axis, a linearly varying Y coordinate as the cart passes the target at constant speed, and a constant depth. The results show that the method is indeed doing a good job of detecting and locating the targets.

Investigation of the correlation picking method surprised us in terms of its lateral effectiveness. It appears consistently able to pick targets up to 0.25m outside of the survey loop, meaning that the loop is covering a 1.5m swath along each line. It will detect large targets as much as 0.5m outside the survey loop. Thus, while we initially expected to implement a voxel array the same size as the MetalMapper array, 1m x 1m, we ended up with a voxel array four times as big, 2.0m x 2.0m. We found it important to select a voxel array that covered a 2m x 2m area because of the MetalMappers ability to locate targets that pass outside its nominal footprint.

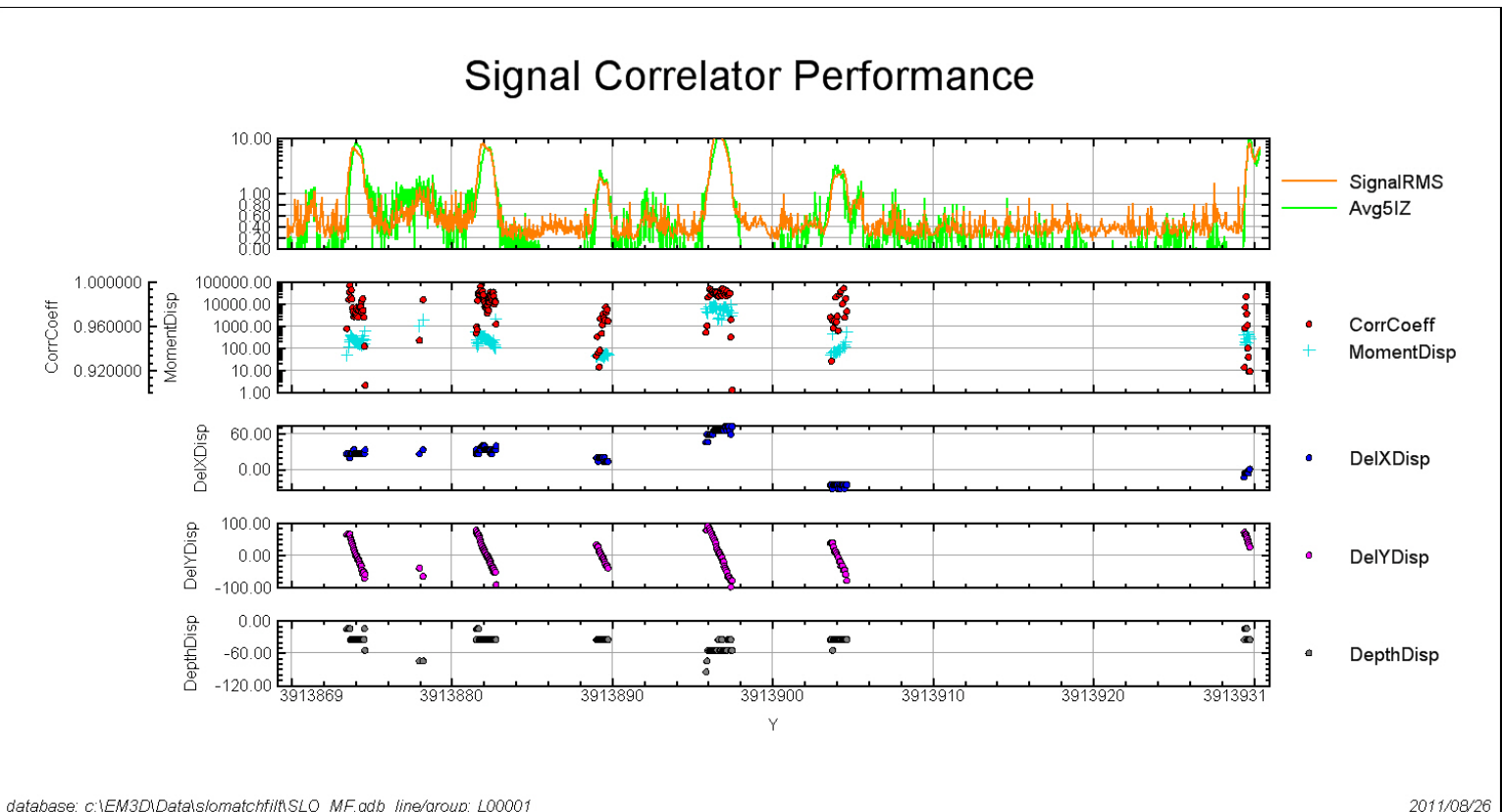


Figure 4.3: Data profiles along Line 1, the westernmost line. The Avg5IZ trace is the signal that is similar to that produced by an EM61. The orange trace is effective RMS signal from seven MetalMapper sensors. Note these traces are plotted on a log/linear scale. The red points in the second panel are correlation coefficient while the blue points are dipole moments. The DelXDisp, DelYDisp, and DepthDisp traces show the target positions in cart-relative coordinates (cm from the center of the cart).

#### 4.1.9 Results

To demonstrate the method in montaj, we chose ten survey lines from San Luis Obispo. These are lines 1 through 10 of the area we designated NWA in our survey there.

A contour map of all ten lines in the study area is shown in Figure 4.4. The map is described in the figure caption. Importantly, the contour plot is made of the traditional 5IZ scalar – the average value of the Z component of the five innermost sensors.

Figure 4.4 shows correlation picks in white. The picks clearly show picks of every significant peak that could be picked from the contour map. The points impressively fall on or near the peaks of the contour map but the clusters are significantly smaller and indicate that the re-acquisition coordinates would be better estimates of target position than the traditional re-acquisition coordinates. In this figures, most of the target picks are of substantially smaller targets than the threshold that was actually used at San Luis Obispo. In production implementation, a contour map would likely not be produced. The white points in Figure 4.4. would be plotted on a blank map for visual confirmation. But the next step is the one that is a clear advantage of this method. The clusters of points are grouped into single targets. This clustering allows the important step to use yet additional thresholds to select points for re-acquisition. One threshold is a distance that is used to decide which points should belong in a given cluster. This threshold could be related, if not identical, to the distance between targets that has traditionally been used to decide whether there is one or two targets at a given location. A second and very important threshold is a moment threshold. In the process of clustering points, an average moment can be computed for each cluster of points. Then this average moment can be compared to a threshold to determine if the cluster should become a re-acquisition point.

This final step is demonstrated in Figure 4.5. It shows clusters of targets that were picked using a distance threshold of 1m and an arbitrary moment threshold. The moment threshold was chosen to make the map approximately similar to the actual points that were picked for re-acquisition in this survey area. The map shows the finally picked clusters as white circles. It also shows, as black triangles, the targets that were actually picked for re-acquisition at San Luis Obispo. Study of this map shows that this new method picked a few targets that were not picked using the traditional method and it shows a few points that were picked with the traditional method but were not picked with this new method. While we cannot show this on these 2D plots, we also know the depth and size of the targets picked using this method.

We believe, from working with these data sets, that the picks using this new method are better. Further work needs to be done to support this conclusion quantitatively. We suggest a further analysis could be done to compare these picks and the original picks to the static data and even to the ground-truth data from SLO.

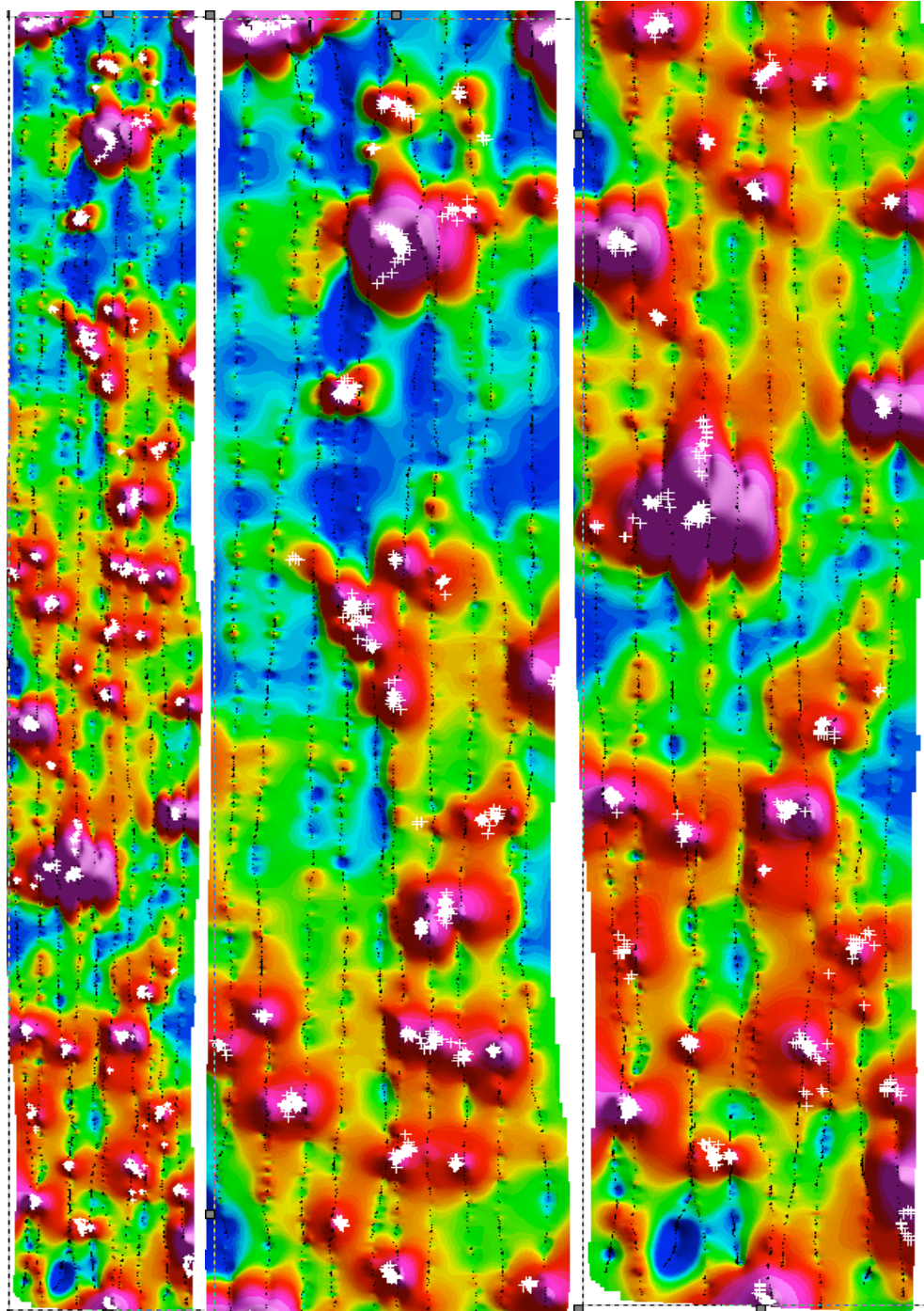


Figure 4.4: Color contour plot of the area studied. The plot is made from the “SIZ” value – a signal roughly similar to the response of an EM61. The faint dots show the track of data points along each of 10 lines. The white crosses are computed target positions. The whole area is shown to the left. Two overlapping halves are enlarged to the right (top on the left, bottom on the right).

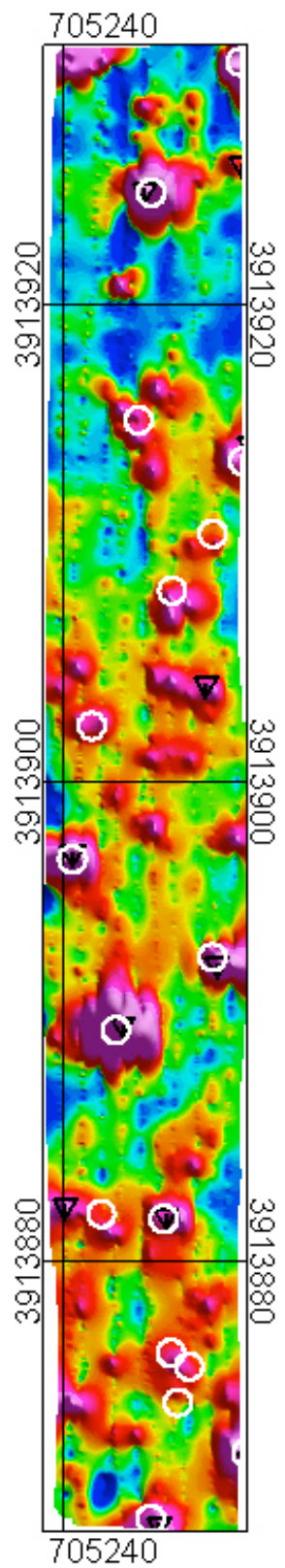


Figure 4.5: Map showing picks using the Signal Correlation method (white circles) compared to picks using the traditional method (black triangles). Area shown is the same as in Figure 4.4.

#### 4.1.10 Conclusions and Recommendations

This new method for cued target mapping and selection has some salient characteristics:

- When this new method is used, MetalMapper data is capable of detecting and mapping targets outside of the array. The small amount of work done in this study (only 10 survey lines at San Luis Obispo) suggests that it may be able to reliably detect and map targets over a path width of 1.5m whereas a ‘normal’ path width is usually assumed to be 1m, the width of the MetalMapper transmitting loop. MetalMapper survey lines have been traditionally been spaced 0.75m on the basis of a 1.0m path width. The wider path width effective in this method could allow 1m line spacing or perhaps line spacing of 1.25m at some sites.
- This method significantly improves a common difficulty of deciding whether multiple sightings of targets from two or more lines are two targets or one. Where a single target between two survey lines might be conventionally mapped as two targets, one on each line, the new method will more likely map the two sightings of the target as one target. Similarly, two targets that are offset from two lines but not between the two lines might conventionally be mapped as one target directly between the two lines, whereas this new method would correctly separate the two targets.
- This initial work indicates qualitatively that the correlation method is robust. Since the correlation is a linear process in terms of the correlation coefficient, we expect it to behave well in the presence of noise. In this regard it should be more robust than non-linear methods.
- The method was implemented (in prototype form) in real-time in the data acquisition program EM3D for MetalMapper. It shows targets moving across the dancing arrows display. It shows target size (i.e. moment, normalized by primary field at the target) via size of the target ‘dot’ and it shows target depth as color of the ‘dot.’ This implementation will allow better interpretation of the ‘dancing arrows’ display and should improve positioning during cued surveys, perhaps eliminating some portion of repeat cued acquisitions.
- Although not explicitly proven because of the small size of the data set, we believe the method provides significantly improved cued-target locations. Improved cued locations should also reduce number of repeat cued acquisitions.
- The multiple-pick method can show two or more targets when those two targets are separated enough in an EM sense. During simulations in this work, we observed that the best-pick method tended to follow one target for a while and then to follow the other target, as the array passed over the targets. In both cases, this new method tended to indicate the presence of multiple targets.
- The method provides a repeatable process that we believe is more deterministic and less ‘artistic’ than the traditional contouring/peak-picking method. Gridded contour maps can be significantly altered by different selection of data reduction and contouring/mapping parameters. Similarly, two-dimensional peak picking from a gridded contour map can be significantly altered by choice of a peak picking algorithm and its parameters. This new

method is not completely immune from similar issues but we believe, based on the small number of results from this study, that computing detection points from the processed data is less artistic than choosing parameters for gridding and contouring, and that selecting clusters of detection points, based on both point spacing and moment-magnitudes, is similar in artistry to peak detection from a 2d map.

- Most importantly, the method allows a final picking of targets based on three distinct thresholds or parameters, as differentiated from the conventional method that sets one threshold that is applied to a contour map. The first is signal level and/or signal-to-noise ratio, the second is correlation coefficient (indicative of signal quality), and the third is magnetic moment (indicative of volume or mass). We believe this will allow better control of threshold selections to assure detection of minimum size targets of interest while not selecting targets of non-interest, especially small near-surface scrap. It remains to be seen how many fewer targets this method will pick compared to the conventional method. A full analysis of the Camp Butner data and/or the San Luis Obispo data is indicated.
- The MetalMapper data in this method is acquired using only the Z transmitter loop. This means that a MetalMapper X and Y transmitter loops could be removed from the antenna array and the dynamic survey could be done using just the Z loop. With the X and Y loops removed, the MetalMapper would be reasonably man-deployable..

We make the following recommendations:

- Provide additional funding to allow a full analysis of this method using the entire sites of San Luis Obispo and Camp Butner.
- Assuming results of additional studies are encouraging, use the MetalMapper for new mapping surveys. We believe that with suitable modification in deployment configuration, that costs can be nearly as low as deployment of an EM-61. And we believe that cost-savings in the rest of the survey will more than offset the additional initial costs.
- Implement this method in a multi-step process, each customized for the site being surveyed. The signal thresholds can be set according to the noise levels and/or other characteristics of the site.

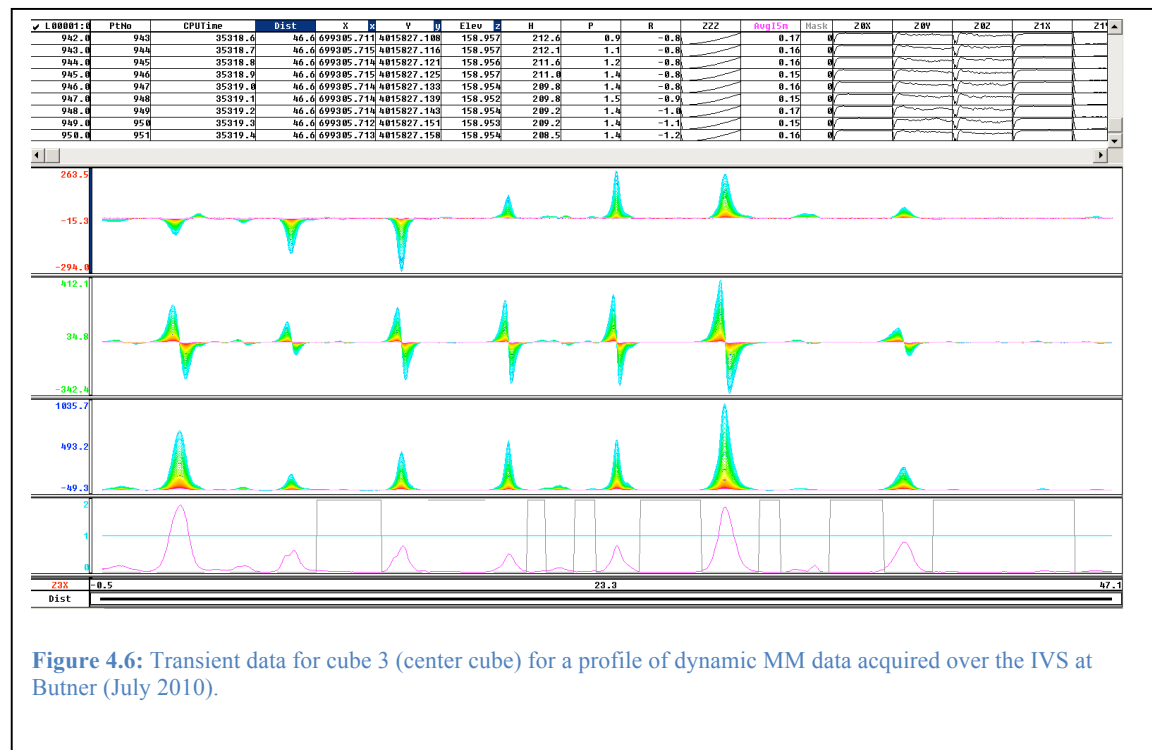
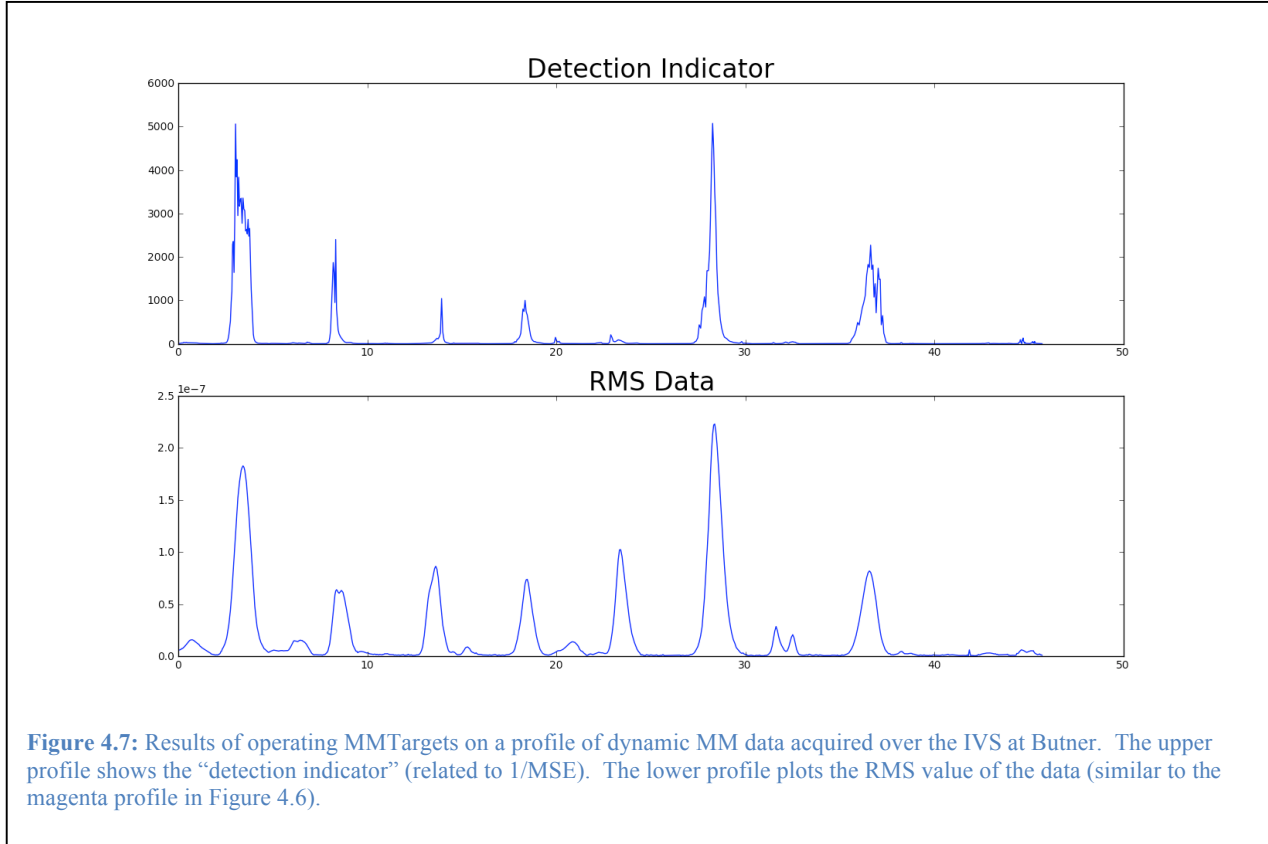


**Figure 4.6:** Transient data for cube 3 (center cube) for a profile of dynamic MM data acquired over the IVS at Butner (July 2010).

#### 4.1.11 Traditional Inversion Using Dynamic Data

In addition, *MMTargets* supports a 4 parameter (x, y, z, and radius) inversion that can be applied to dynamic *MetalMapper* data to support the target detection phase of remediation efforts. This procedure executes quickly enough to support pseudo-real time processing. The mean squared data misfit is useful for indicating when a potential target is present. Combining this with the anomaly amplitudes provides a high quality indicator that incorporates physics and reduces the uncertain threshold issues that arise with simple amplitude threshold-based target picking. We have applied this mode of processing to an example profile acquired over the IVS at Camp Butner (Figure 4.6). The method is functionally equivalent to the method of **Signal Pattern Correlation** described above except the technique does not rely on tabulated Green's functions. Our purpose here is simply to report that *MMTargets* has this capability. The results of the detector output are shown in Figure 4.7. At each point along the detector profile, *MMTargets* produces an estimate of the relative target position and its size. A simple threshold applied to the “Detector Indicator” curve identifies source point clusters corresponding to the target.



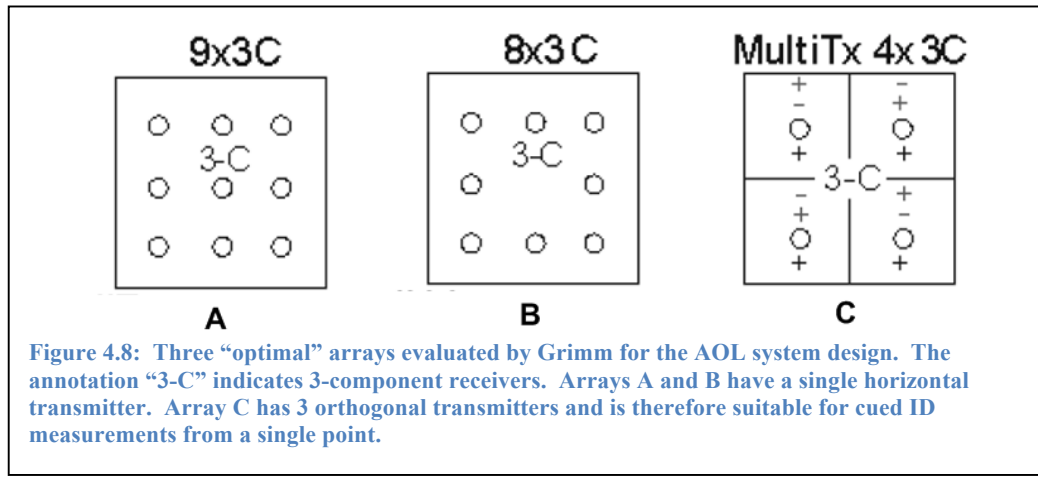
## 4.2 Optimizing The MetalMapper Receiver Array (Task 2)

### 4.2.1 Background

#### 4.2.1.1 The AOL Study

Early work on optimum arrays was reported by Grimm and Sprott [2] and was supported by NAVFODTECHDIV. Grimm extended that work (unpublished) to consider a configuration with 3 orthogonal transmitters. The important conclusions arising from Grimm and Sprott's study were:

1. In all cases, arrays with triaxial (3-component) sensors performed better than similar arrays with 1-component sensors where the performance metric is a measure of the error in the estimated target polarizability.



2. For arrays with a single 1 m x 1 m horizontal transmitter, a 3 x 3 grid of 3-component receivers centered inside the transmitter loop gave the best performance (Figure 4.8A). An 8 receiver array consisting of the 3 x 3 grid with the center receiver omitted performed nearly as well as the array with the 3 x 3 receiver grid (Figure 4.8B).
3. An array of 3 orthogonal 1 m x 1 m transmitters with 3-component receivers centered in each of the 4 quadrants of the horizontal loop (Figure 4.8C) also performed “very well.”
4. Grimm’s study formed the basis for specifying the receiver arrays for the original Advanced Ordnance Locator (AOL), the follow-on AOL2 project, and, subsequently, the MetalMapper project.<sup>9</sup> Grimm’s work was based on model parameter estimations using a grid of data points centered over the target. He did not perform an extensive study on the performance of the more complex 3-transmitter array (Figure 4.8C) using data from a single site. Grimm did not consider the deleterious effect of uncertainties in relative position and attitude errors within the measurement grid. The effect of these errors and the need for extremely precise locations (O[1cm]) has been noted for some years [3].

---

<sup>9</sup> The AOL project was awarded to Blackhawk Geoservices in 2003 by NAVFODTECHDIV (Contract #N00174-03-C-0006). The follow-on contract was awarded in 2005 to G&G Sciences, Inc. The MetalMapper project was funded by ESTCP and was awarded to Geometrics in 2006.

#### 4.2.1.2 The BUD Study

In a study leading up to the configuration of the BUD system, Smith et al [4] conducted a study similar to that of Grimm. The study focused on optimizing the positions of 4, 5, and 6 single-component receivers using a sphere model. Their study considered arrays with 1, 2, and 3 transmitter loops. The study found that the sensitivity of changes in receiver position is low when they used a spherical target. However, when highly elongated (1000:1 “needles”) targets were used, Smith and Morrison found narrow zones of high uncertainty for recovering polarizability for those targets when the array contained 4 single-component (Z) receiver loops. These zones are “greatly ameliorated” for the 5-receiver and 6-receiver cases (Fig. 4 in [3],). Although Smith et al do study the effect of receiver orientation on the recovery of target polarizability for elongated targets, they did not study the effect for vector (i.e., 3-C) measurements of the secondary fields.

#### 4.2.1.3 Discussion of Previous Receiver Arrays Studies

From our review of the two studies [2, 4, 5] we have identified several important differences:

1. Grimm [2, 5] considered both single-component (“1-C”) and 3-component (“3-C”) receiver arrays and concluded that “3-C” arrays performed better. Smith et al [4] considered only single-component receivers.
2. Grimm used a set of 5 different targets representing bodies with symmetry (rod-like and plate-like, and sphere-like), and two types of asymmetrical bodies (clutter-like). Smith et al studied only two targets: a sphere, and a 1000:1 elongate target.
3. Grimm’s study looked at the optimal number of receivers and for this purpose he evaluated 11 array geometries including the geometry of commercially available EMI systems (e.g. EM-61/EM-63). Smith and Morrison focused on arrays containing 4, 5, and 6 (“1-C”) receivers and studied performance of these arrays as a function of the receiver position. Although Grimm’s study [2] did not directly include the evaluation of an antenna configuration with 3 1mx1m transmitter loops, he did evaluate a system containing 4 ½ x ½ m transmitter loops that could be configured so that the currents flow with alternating polarity as well as a common polarity. Using this configuration he evaluated performance based on 3 different transmitter polarities simulating in most respects an array with 3 orthogonal 1m x 1m transmitters. The majority of Grimm’s testing, however, involved simulating measurements over a uniform grid of points numbering either 121 (11 x 11 = *Dense* grid) or 25 (5x5 = *Sparse* Grid). There was no effort in his multi-site modeling to introduce uncertainties either in platform location or in platform attitude. We now know that these uncertainties dramatically affect the ability to extract accurate target parameters. Grimm’s work concluded that the 4-transmitter array performs significantly better than the other 10 arrays he evaluated under all scenarios he considered.

#### 4.2.1.4 About the MM Array

During the AOL, AOL2, and MetalMapper projects we have made numerous free-air static measurements to characterize various UXO or UXO-surrogates (e.g., steel cylinders). These measurements were always conducted with the targets centered beneath the antenna array. Furthermore, the sites of previous demonstrations (e.g., APG, and YPG) were flat. Consequently, the static data from these sites was acquired with the platform well centered over the target. As part of our QC program at SLO, we acquired repeat measurements over targets anomalies with horizontal offsets to the source of more than 40 cm. Figure 4.9 shows the principal polarizability curves derived from two MetalMapper static data sets in proximity to the same target, a 60 mm mortar. Both curves have good Fit parameters (99.8 and 99.1). The polarizability curve set from SLOStatA01584 (Figure 4.9– lower left) does not exhibit the symmetry characteristic we have come to recognize and even require as an essential attribute or indicator of a UXO-like shape. In this case, the lateral offset between the platform and the target (~50 cm) prevented the target from being adequately stimulated along each of its principal axes.

The points we wish to make here are:

1. Large horizontal offsets between a target position and the platform can occur in steep terrain.<sup>10</sup>
2. The symmetry indicator derived from estimates of the principal polarizability can be significantly degraded by large offsets.
3. In our opinion, previous model studies performed to select an optimum array did adequately focus on the effect of platform offset. Our intuition tells us that 3-component measurements of the secondary fields become more important with increasing offset of the target from the platform.

#### 4.2.1.5 Optimal Arrays Study Objectives

In the implementation of the AOL systems (AOL and AOL2) as well as the BUD system, engineering considerations led to the construction of prototype antenna arrays that depart from the optimum arrays identified by the cited studies. Geometrics is working to commercialize a

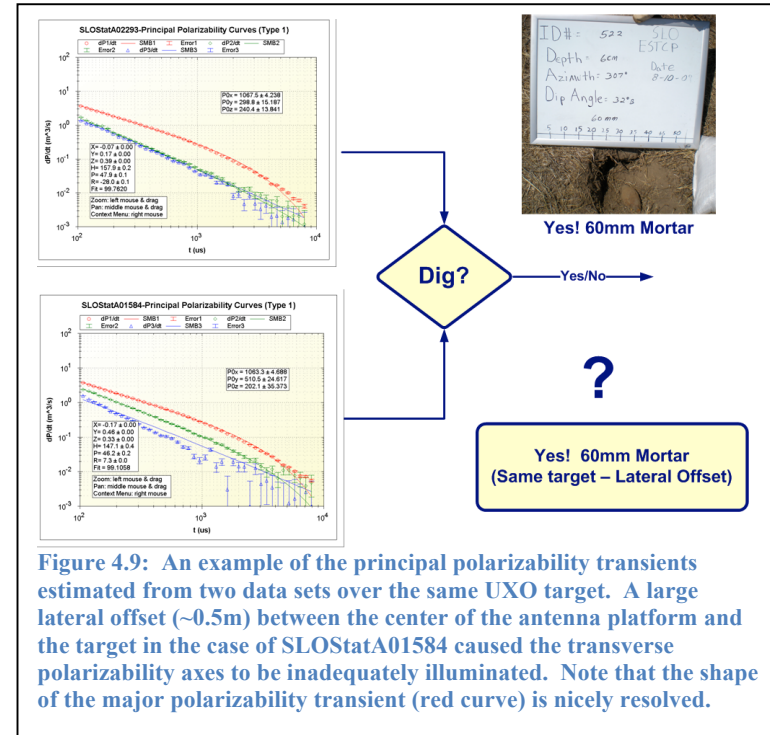


**Figure 4.9:** An example of the principal polarizability transients estimated from two data sets over the same UXO target. A large lateral offset (~0.5m) between the center of the antenna platform and the target in the case of SLOStatA01584 caused the transverse polarizability axes to be inadequately illuminated. Note that the shape of the major polarizability transient (red curve) is nicely resolved.

<sup>10</sup> Offset bias can be reduced if the GPS position is corrected for platform attitude and heading in real-time before it is displayed.

version of this advanced EM technology based on concepts and hardware that have evolved primarily out of the AOL projects that were supported by NAVEODTECHDIV [6]. From the broad perspective of moving this technology from the applied research and demonstration side toward a point where it is not only accepted by the UXO and regulatory communities but also is commercially available, it is important that we review the design of the antenna arrays in order to specify one or more array configurations that maximize the cost-effectiveness of deployment for a particular purpose.

Our objective here is to expand on the excellent (and still relevant work) of Grimm and Sprott [2] and Smith and Morrison [4] to provide answers to the following questions:

1. Under what circumstances are full vector measurements of the secondary field from a target necessary or desirable?
2. What is the penalty that we pay for reducing the number of tri-axial receivers on the MetalMapper platform?
3. How does the horizontal offset between a target and the antenna platform affect the estimation of target parameters?
4. How sensitive is the performance of an otherwise optimum receiver array to small changes in receiver positions. Is there a difference in this sensitivity for 1-C and 3-C receivers?

In this section, we attempt to provide answers to these questions using a new single-source target parameterization program, MMTTargets [1] and other codes.

#### 4.2.2 Arrays Studied

Our interest is in the MetalMapper. Furthermore, we are primarily interested in static measurements at one (or perhaps more) sites that are (more-or-less) over the subsurface target. Therefore, we use the performance of the existing configuration of the MetalMapper as a baseline against which we compare the performance of other systems. In Figure 4.10 we show 8 arrays that we evaluated. The arrays are divided into two groups:

1. **1-C** – A group of 3 arrays having 1-component receiver loops. In all cases, these “1-C” receiver loops are sensitive to fields aligned normal to the plane of the Z transmitter.
2. **3-C** – A group of 5 antenna arrays have 3-component receiver cubes.

Array names consist of a 4-character group plus a 2-character group separated by a hyphen (e.g. 3T5C-30). The 4 character group consists of the characters “3T” that indicate the number of transmitter loops plus another two characters

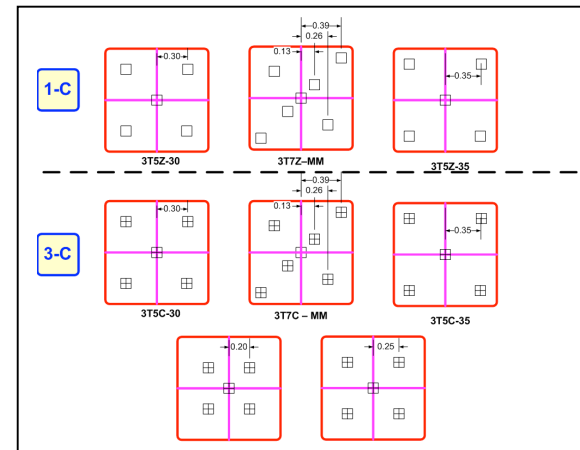


**Figure 4.10: Antenna arrays evaluated during this study. All receiver coils are located on the diagonals of the Z (horizontal) transmitter coil.**

indicating the number of receiver locations and the receiver type (e.g., C = Cube or tri-axial receiver; Z = single component receiver sensitive to vertical fields). The last 2-character group indicates the MetalMapper when it is “MM” and when used in connection with 3T5C or 3T5Z configurations the two figures indicate the X and Y offset from the center of the loop to the center of the receiver. All receivers in this study are centered in the plane of the Z transmitter.

Note that, with the exception of the MetalMapper configurations (3T7C-MM/3T7Z-MM), all the arrays have 5 receivers (either C or Z) and the only difference between arrays is the offset along the diagonal from the array center. We note that the array 3T5Z-35 approximates the “optimum” 5-receiver array determined by Smith and Morrison for spherical targets.

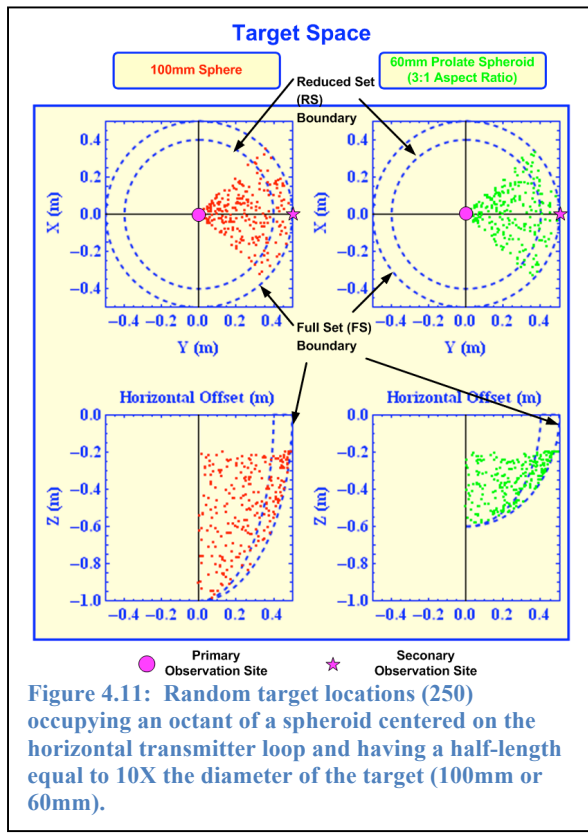


**Figure 4.11:** Random target locations (250) occupying an octant of a spheroid centered on the horizontal transmitter loop and having a half-length equal to 10X the diameter of the target (100mm or 60mm).

#### 4.2.3 Target Space

Given the constraints on the array geometries (i.e., receivers lie along the diagonals of the transmitter loops), we choose to constrain all targets to an octant of a spheroid that is centered at the center of the Z transmitter loop (also the center receiver) having a half-length equal to the 10X the diameter of the test target (e.g., 1m for a 100mm sphere) and a radius equal to half the side dimension of the Z transmitter loop (0.5m). Plan and cross-sectionals of random target locations appropriate for each target diameter are shown on the left (100mm Sphere target) and on the right (60mm Prolate Spheroid) of Figure 4.11. The plotted points represent the locations of 250 random targets. Our experience with the MetalMapper based on demonstrations and a limited amount of modeling is that parameter extraction is much more reliable when the targets have a horizontal offset that is less than 0.4m ( $r < 0.4m$ ). In Figure 4.11, we have drawn a second (inner) boundary that corresponds to this smaller (0.4m) offset distance. We call the targets that are confined within this smaller spheroidal volume the **Reduced Target Set (RS)**.

Our single-source dipole-based modeling program (MMTargets) is able to extract target parameters from data measured at one or more measurement sites. In this report, we include a few results based on the analysis of data from 2 sites. The primary site (shown with a magenta disk) is at the center of the plan view of target space (Figure 4.11). The secondary site is offset by 0.5m east and therefore is centered and tangent to the east edge of the full target set (FS). We have chosen to restrict our target placement to a single octant of a spheroidal volume. Using solutions based on a measurement at the primary measurement site, symmetry arguments allow us to infer that the results would be the same if we distributed the targets over the other 3 octants and processed. However, to make the same inferences using a multi-site solver we would need

to occupy 5 sites (a center site plus 4 sites offset in the 4 cardinal directions). Here, we are simulating a case where the location of the target based on a measurement at the primary site **vectors** us to the secondary site.

#### 4.2.4 Target Features

In this study we follow the lead of Smith and Morrison [4] and use a 100mm sphere as the target for the initial evaluation of array performance. Then we check our results with a target that better simulates the response of a UXO. For this purpose, we use a 60mm diameter prolate spheroid shape with a 3:1 aspect ratio (length = 180mm). The principal polarizability transients of the two targets are plotted in Figure 4.12. For the purpose of this study, the polarizability is sampled at 42 time logarithmically spaced time gates ranging from  $106 \leq t \leq 7916 \mu\text{s}$ . Each time we invert a data set, MMTTargets provides an estimate of the principal polarizability transients of the target together with its extrinsic properties (i.e., the position and attitude angles). In principle, one could match the resulting estimated target polarizabilities with the appropriate curves in Figure 4.12 and form an error estimate (e.g., MSE, RMSE, etc). In our case, it was easier to extract a few scalar **features** from the curves and compare those with known values determined either theoretically or calculated directly from the curves in Figure 4.12. We chose the latter. In Figure 4.13 we define a set of 5 **meta** features that we extract from the parameters that are provided by the modeling program (MMTargets). One feature ( $\hat{V}$ ) is simply proportional to the spheroid volume (estimated from the spheroid length and diameter). The other 4 features are calculated from the integration of the 0<sup>th</sup> and 1<sup>st</sup> order time moments of the 3 principal polarizability curves. The true values of these parameters for the 100mm sphere and the 60mm prolate spheroid target have been tabulated in Table 4.1.

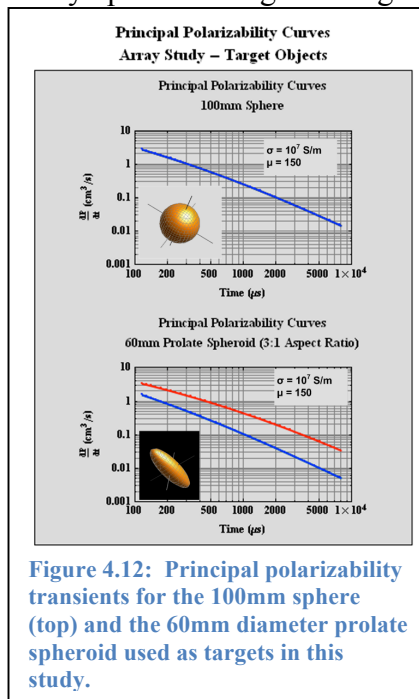


**Figure 4.12:** Principal polarizability transients for the 100mm sphere (top) and the 60mm diameter prolate spheroid used as targets in this study.

**Table 4.1:** Tabulation of various target features extracted from principal polarizabilities shown in Figure 6 and the target dimensions.

Param	100mm Sph	60mm Pr Sphrd	
Vhat	<b>524</b>	<b>339</b>	Size (cm <sup>3</sup> )
P0x	1060	1755	
P0y	1060	485	
P0z	1060	485	
I2P0	<b>1060</b>	<b>745</b>	
P0t	1060	485	
P1x	1392395	2817563	
P1y	1392395	544637	
P1z	1392395	544637	
I2P1	1392395	941953	Shape (cm <sup>3</sup> * us)
P1t	1392395	544637	
RLO	<b>1.0000</b>	<b>1.0000</b>	
P0e	0.0000	0.0000	
P0r	<b>1.0000</b>	<b>3.6149</b>	Time (us)
P1e	0.0000	0.0000	
P1r	1.0000	5.1733	
Taul2	<b>1314</b>	<b>1264</b>	
Taux	1314	1606	
Taut	1314	1122	

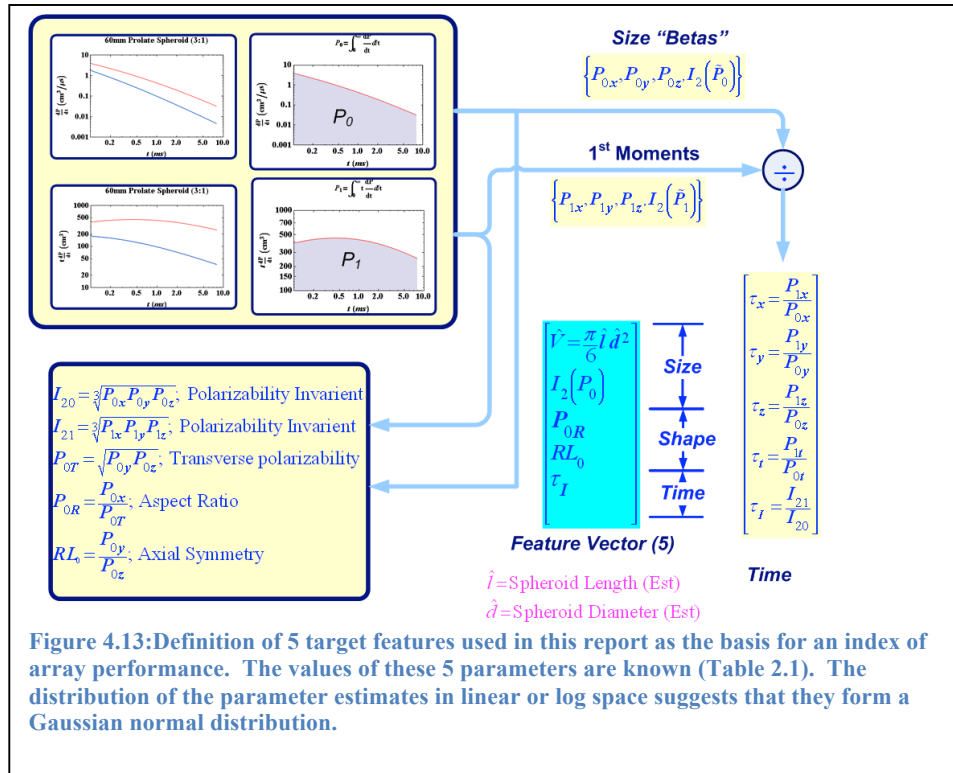
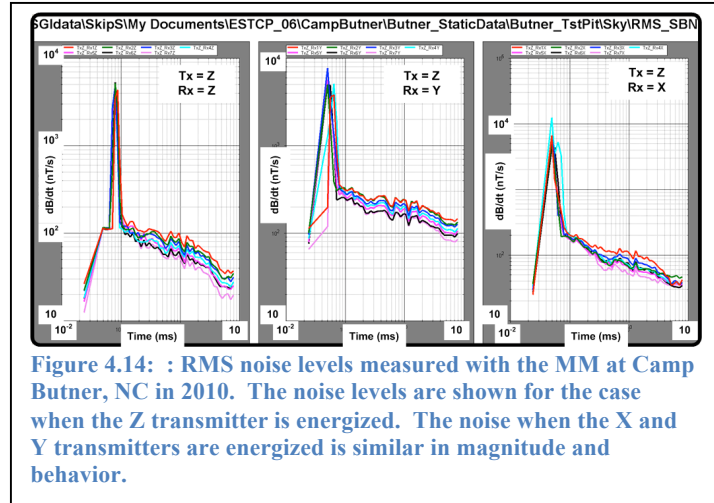


Figure 4.13: Definition of 5 target features used in this report as the basis for an index of array performance. The values of these 5 parameters are known (Table 2.1). The distribution of the parameter estimates in linear or log space suggests that they form a Gaussian normal distribution.

#### 4.2.5 Electromagnetic Interference

The array studies referenced earlier [2, 4, 5] corrupted otherwise perfect model data with random noise to make the array study more realistic. Grimm [2] based the amplitude of his noise levels on a fraction of the signal level of his cylinder target oriented vertically and placed at the shallowest depth (0.55m<sup>11</sup>). Smith [4], on the other hand, assumed a constant noise field of 2 nT/s for receivers responding to a vertical field, varying to 6 nT/s for receivers responding to horizontal fields. Our noise data suggest that their estimate of noise is low by as much as an order of magnitude depending on stacking. In this study, we base our noise values on noise measurements that we have derived from experimental measurements with the MetalMapper over background points. We show in Figure



<sup>11</sup> The depth quoted here includes 0.4m which is the assumed height of the horizontal transmitter loop above ground-level.

4.14 transients representing the RMS noise values for each time channel and each receiver the case of no stacking. The results are plotted only for the case where the Z transmitter has been energized. Plots made with the X and Y transmitter energized, respectively, produce plots that have RMS noise values similar both in magnitude and decay rate with those shown for the Z transmitter (Figure 4.14). The decay in noise values in time is characteristic of the behavior of RMS noise levels when presented this way since it reflects the greater averaging that arises because of the logarithmically increasing gate widths as the gate centers are moved out in time. Figure 4.14 suggests that the noise levels at delay times of around 0.1 ms (100us) are on the order of 100 nT/s. The noise level is larger by about a factor of 2 for the horizontal components. Therefore, we have added random noise to our synthetic data in the amount of 300 nT/s for both horizontal components and 150 nT/s on the vertical components.<sup>12</sup> Consistent with the logarithmically expanding gate widths at later times, we reduce the level of noise at each subsequent gate by a factor equal to the square root of the ratio of the gate width at 106us to the gate width of the time gate under consideration. In practice, this causes the noise level to decrease with a slope of  $-1/2$  when plotted in Log-Log space as is done in Figure 4.14.

#### 4.2.6 Position and Attitude Uncertainty

When processing static data from a single measurement site, small errors in platform position and attitude angles simply serve to bias the estimated position and attitude of the target when they are transformed into the geographic coordinate system. However, we computed some results using two measurement sites. In order to show how small errors in position and platform attitude affect multi-site performance, we introduced random variations in each of the three coordinates with standard deviation of 0.02m and in the 3 attitude angles with standard deviation 1° when calculating the model data.

#### 4.2.7 Parameter Extraction

We inverted each set of 250 data files using MMTTargets, the single-source modeling program that has been described in some detail in Section 2 of this report. As related in that section, MMTTargets generates constrained solutions for the best fitting sphere, prolate spheroid, and oblate spheroid. Lastly, it solves the fully unconstrained problem for the best fitting ellipsoid. From those solutions, we extracted the position and attitude estimates together with the estimates for the target's radius and half-length. In a separate operation, MMTTargets computes the principal polarizability transients using the target position corresponding to the constrained solution that has the least mean square error (MSE). Predictably, that solution invariably corresponds to the ellipsoidal model. From these target parameters (primary features) we are able to compute the 5 meta-parameters (and more that are not listed) highlighted in Figure 4.13. In subsequent sections we will use scatter plots of scalar parameters that we have compiled from each the data sets corresponding to each array and/or target situation. And finally, we will show a metric that quantifies in some sense the relative performance of various arrays.

---

<sup>12</sup> In retrospect, we realized that the noise levels shown in Figure 8 do not account for stacking. Therefore, we could justify reducing the noise levels by a factor of 10 to account for the effect of stacking. This would no doubt greatly improve our performance estimates. But the noise levels would remain at 10/20 nT/s, which is several times larger than that used by Smith [3].

#### 4.2.8 SNR and MSE

In general, the quality of the target parameters derived from a data set corresponding to a static MetalMapper measurement of a target located at a specified position with a specified attitude can be determined by the quality of the fit to the observed data. In MMTTargets, the fit parameter is the mean square error (MSE) between the input data and the data calculated based on estimates of the various target parameters. In Figure 4.15, we summarize data quality with two histograms and two scatter plots using the SNR and the MSE fit statistics for the set of 250 sphere data sets corresponding to the 3T7C-MM (the MetalMapper array)

and the relationship between the two quantities. A few remarks are in order. Firstly, the histogram of SNR shows that about 80 percent of the data sets processed have an SNR > 20dB. Secondly, these uniformly high SNR's result in a similar percentage of the corresponding MMTTargets solutions exhibiting rather good MSE (i.e., MSE<0.2) as shown by the histogram of the MSE's for this data set (Figure 4.15B). In the right hand side of Figure 4.15(panels C & D) we show scatter plots for the full (250 targets) target data set (Figure 4.15C) and the reduced target set (164 targets). Recall that in the reduced set (RS) we have excluded targets positioned outside of the inner spheroidal boundary (see Figure 4.11). What is interesting about these plots is that the outlier points shown in Figure 4.15C (FS) disappear when we reduce the target set by removing targets outside of the spheroid of radius 0.4m (see Figure 4.11). This implies that MMTTarget has trouble finding good solutions for targets with horizontal offsets that place them beneath the sides of the transmitter. Detailed examination of shallow targets with horizontal offsets in the range  $0.4 \leq r \leq 0.5$ m show many if not all the targets forming the outlier points in Figure 4.15C fall within this zone.

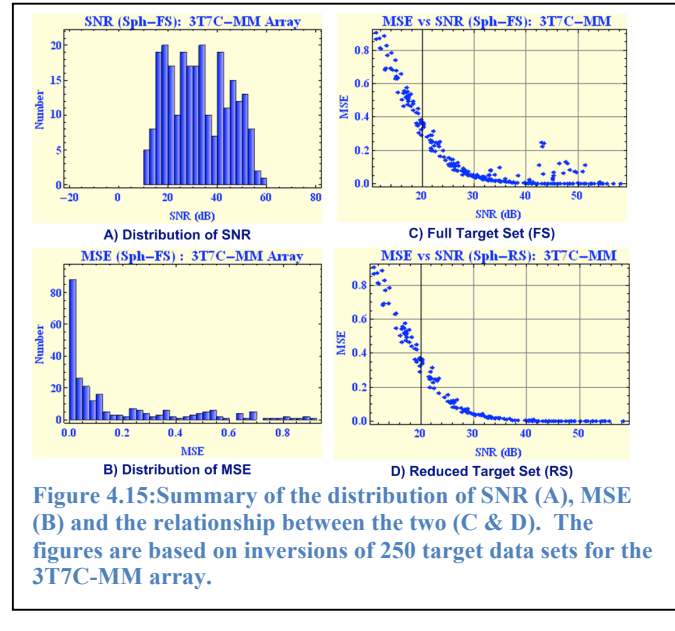
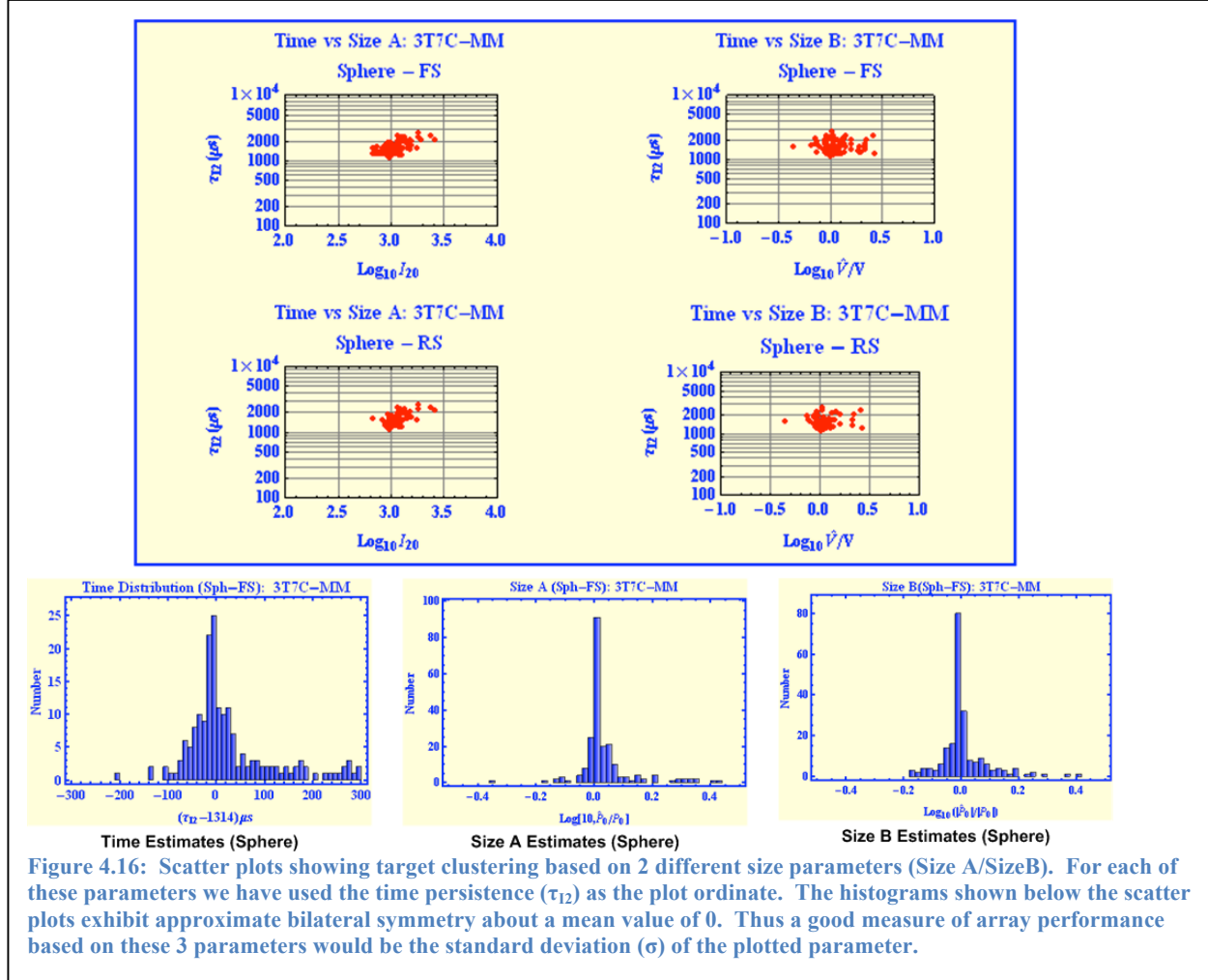


Figure 4.15:Summary of the distribution of SNR (A), MSE (B) and the relationship between the two (C & D). The figures are based on inversions of 250 target data sets for the 3T7C-MM array.

#### 4.2.9 Target Size & Time Persistence

Target parameters related to size and to time persistence are frequently very useful target parameters for classification. In Figure 4.13, we have identified 2 size-related target features ( $\hat{V}$ ,  $I_{20}$ ) and a time persistence feature ( $\tau_{12}$ ) that we will use to evaluate array performance. In Figure 4.16, we show Log-Log scatter plots of these parameter pairs for the full set (FS) of targets and for the reduced set (RS). These scatter plots show that both size estimates and the time estimates cluster well around their expected values in Log space. We have also included histograms showing the distribution of the  $\tau_{12}$  (in linear space – bottom left of Figure 4.16) and the two size features plotted in logarithmic space. To emphasize that the mean of these parameters effectively equal to their theoretical values, the appropriate value has either been subtracted (as in the case for  $\tau_{12}$  – Figure 4.16 lower left) or used as a normalization factor (the two size parameters – bottom center and right panels in Figure 4.16). These histograms show that time errors approximate a distribution with (approximate) bilateral symmetry in linear space while the two size parameters approximate distributions with bilateral symmetry in log space



(e.g., log-normal distributions). We emphasize this behavior since we will use the standard deviations of these parameters as performance metrics for the arrays we evaluate.

#### 4.2.10 Target Shape

After size and time persistence, target attributes that indicate shape are particularly important. In fact, many times interpreters (this author included) focus on target symmetry as indicated in a set of principal polarizability curves having a single major polarizability transient and a pair of smaller minor transients that are identical or nearly identical. This is the ideal case and the one that we always see in free-air or pit measurements when the target is located beneath the center of the MetalMapper antenna array. But as Figure 4.9 illustrates, one should be careful to take into account the offset of the target from the center of the array. We now know that large horizontal offsets can degrade target features affected by the targets symmetry. In Figure 4.9, the lack of symmetry suggested by the polarizability curve set shown in the panel on the lower left is caused by the fact that the target is offset from the center of the MetalMapper array by a distance of slightly more than 0.5m.

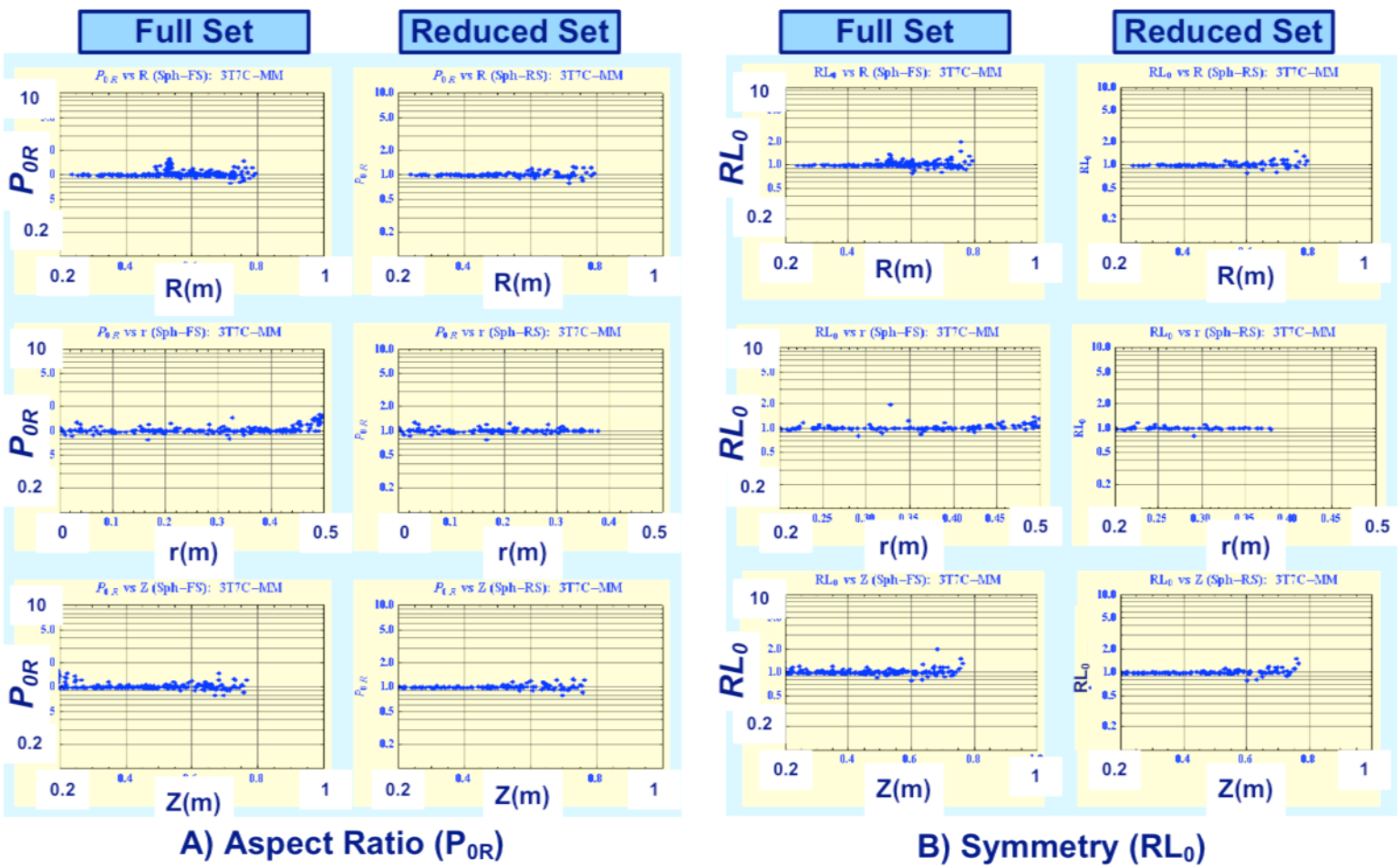


Figure 4.17: Scatter plots of EM aspect ratio parameter (A- $P_{0E}$ ) and symmetry parameter (B- $RL_0$ ) versus target position relative to the platform reference point. The difference between the FS plots (left columns) and RS plots (right columns) demonstrate that it is difficult to resolve shape for shallow targets with horizontal offsets (r) near 0.5m.

In Figure 4.13 we have identified 2 target attributes that provide important information about target shape:

1.  **$P_{0R}$** : This is a measure of the ***aspect ratio***. We have defined it as the ratio of a scalar measure of the major polarizability curve to the geometric mean of the corresponding scalar measures of the two minor polarizability curves. Note that in our definition, aspect ratio is independent of symmetry. We expect a sphere to have an aspect ratio of 1. A UXO is generally expected to be elongated and therefore will have an aspect ratio  $P_{0R} > 1$ .
2.  **$RL_0$** : We use this parameter as an indicator of ***target symmetry***. The parameter is formed as the ratio of two size-related scalar *metaparameters* derived, respectively, from the two minor principal polarizability transients. When the minor curves are identical,  $RL_0 = 1$ . Because we order the principal polarizability according to their size on some basis, good data will usually produce values that are greater than or equal to 1 ( $RL_0 \geq 1$ ).<sup>13</sup>

Using the parameters extracted from our sphere data (3T7C-MM array), we have studied these two shape parameters and their dependence on distance (R) from the center of the MetalMapper array, the horizontal offset distance (r) from the array center, and the target depth. Scatter plots for those parameter pairs are in Figure 4.17A and Figure 4.17B.

In the top row of Figure 4.17A, the aspect ratio is plotted against target distance or range (R). When looking at the full set, we see that estimated aspect ratios show significant departure from their true value (1) at a range of 0.5 and then again at ranges near the maximum for those points plotted.<sup>14</sup> Note that the outlier points at  $R=0.5\text{m}$  are gone when we plot the points for the reduced set. One can infer from these 2 plots alone that the outliers come from shallow targets with horizontal offsets near 0.5m. The second and 3<sup>rd</sup> pair of plots confirm that the problem targets are shallow and have offsets near 0.5m.

In Figure 4.17B, we use  $RL_0$  as the shape parameter. The plot pairs once again show that our ability to determine symmetry properties of targets degrades both with horizontal offset (middle pair) and with depth (lower pair). We are clearly attuned to the fact that the quality of the target parameters degrades with low SNR and so the scatter in the symmetry plots at greater target depths comes as no surprise. For

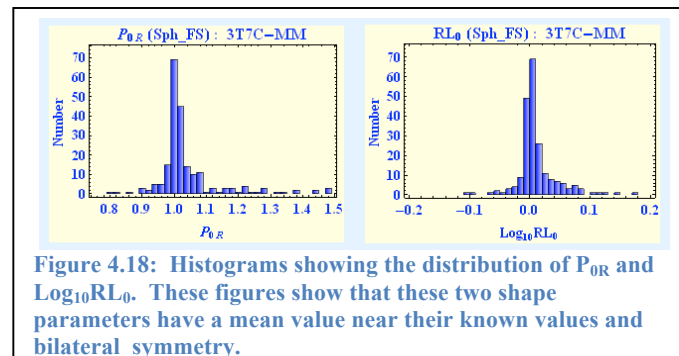


Figure 4.18: Histograms showing the distribution of  $P_{0R}$  and  $\log_{10}RL_0$ . These figures show that these two shape parameters have a mean value near their known values and bilateral symmetry.

<sup>13</sup> Our definition of  $RL_0$  is based on numerical integrations of the principal polarizability transients. There are cases usually involving noisy data or polarization curves exhibiting cross-over. In these cases, we sometimes see  $RL_0 < 1$ .

<sup>14</sup> The astute reader will notice that the range (R) of the target sets halts at  $R=0.8\text{m}$  and not  $1.0\text{m}$ . That is because we used a noise level that was too large to get good solutions for the deeper targets. We excluded those from these plots.

completeness and in order to justify the use of these two shape parameters in defining a performance metric, we include histograms showing the distribution of the both  $P_{0R}$  and  $RL_0$  as Figure 4.18.

#### 4.2.11 An Array Performance Metric

The preceding discussions together with the various graphics have been leading up to a definition of a metric function that we can use to summarize the performance of the arrays that we evaluate. That end, the five parameter histograms in Figure 4.16 (bottom panel) and Figure 4.18 suggest that the standard deviations of the parameters plotted can be used as a metric. In equation 4.9 below, we define that metric.

$$P\left(\hat{V}, \hat{I}_{20}, \hat{P}_{0E}, \widehat{RL}_0, \hat{\tau}_I; V, I_2\right) = \left\langle \log_{10} \frac{\hat{V}}{V} \right\rangle + \left\langle \log_{10} \frac{\hat{I}_{20}}{I_2} \right\rangle + \left\langle P_{0E} \right\rangle + \left\langle \log_{10} \widehat{RL}_0 \right\rangle + \left\langle \hat{\tau}_I \right\rangle \quad (4.9)$$

$\langle \rangle$  = Standard Deviation

In equation 4.9, the 5 quantities  $(\hat{V}, \hat{I}_{20}, \hat{P}_{0E}, \widehat{RL}_0, \hat{\tau}_I)$  are the estimates of the 5 features for the target population for a given array situation. The two scalar parameters  $(V, I_2)$  are the known values of the spheroid volume and the scalar polarizability tensor invariant for the target being used (see Table 4.1). We have chosen to compute standard deviations of 3 target features after taking their logarithms because these parameters appear bilaterally symmetric and have mean values at or near their correct values.

#### 4.2.12 Array Performance Results

As we indicated earlier in this report, we first evaluated the performance of 6 of the arrays (the 5 3-C arrays plus 3T7Z-MM) shown in Figure 4.10. The results reflect inversions from a single receiver site. Then, using the multiple-site inversion capability of MMTTargets, we studied the performance of the present MetalMapper array when two sites over the target have been measured. In this case, we simulate the scenario of a repeated measurement based on large target offset. In such a case, the repeat measurement site has been offset to a site based on the estimated target position using data from an earlier measurement site.

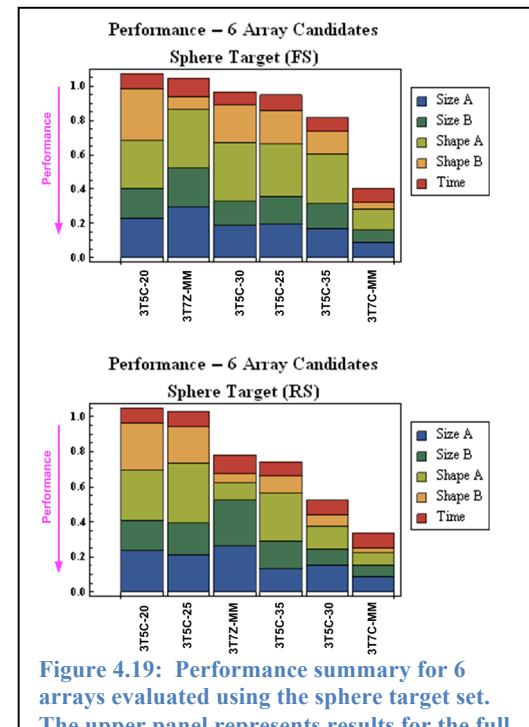
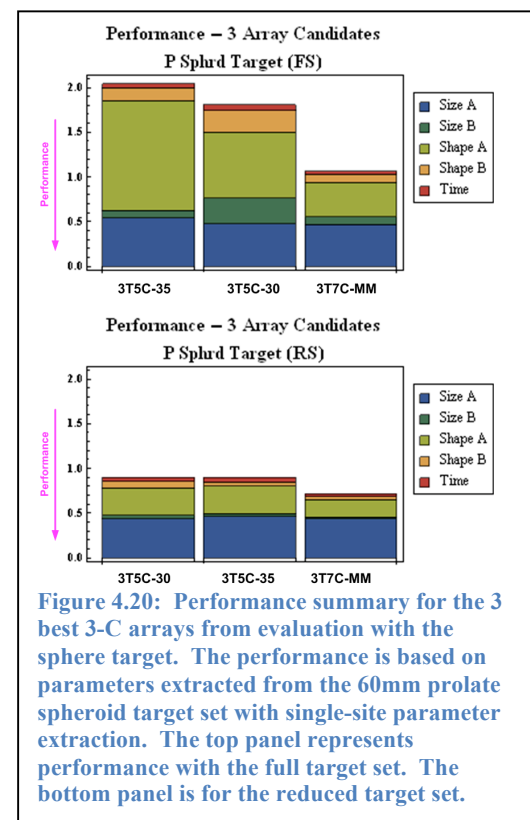


Figure 4.19: Performance summary for 6 arrays evaluated using the sphere target set. The upper panel represents results for the full set (FS), the lower panel shows results for the reduced (RS) target set.

#### 4.2.13 Single-Site Data – Sphere Target

The performance results for all 5 arrays containing tri-axial receivers (3-C) plus one array containing only single-component (1-C) receivers are summarized by means of stacked bar graphs in Figure 4.19. Perfect performance would result if the standard deviations computed in equation 4.9 were zero. Therefore performance increases in the reverse direction of the P value.

For both the full and reduced data sets, the current MetalMapper configuration (3T7C-MM) performs the best. Next, notice that the 1-C version of the MetalMapper configuration (3T7Z-MM) is only marginally better than the array with the worst performance score (3T5C-20). Clearly, 3-component receivers significantly improve performance, even when the targets are kept well within the 1m x 1m area defined by of the horizontal transmitter. Finally, there is a clear trend that suggests that in a receiver array consisting of 5 Cubes, the receivers should be placed outside the geometric center of each quadrant of the 1m x 1m transmitter loop. The results are slightly ambiguous on that score since the 3T5C-35 array is the best 5-Cube array when evaluated with the full set (FS) of sphere targets. But when evaluated against the reduced set (RS), the 3T5C-30 performs better. We note here that in their study Smith et al [4] determined that a system with 5 1-C receivers constrained to be placed within the transmitter loop is optimum for sphere targets when the receivers are near the center and near the 4 corners of the transmitter loop at an offset distance of between 50 and 60 cm. The 3T5C-35 has 4 of its 3-C receivers at a distance of ~50cm from the center. The 3T7C-MM array has 2 receivers at a distance of 55 cm. Our results appear to be consistent therefore with the findings of Smith and his associates.



**Figure 4.20: Performance summary for the 3 best 3-C arrays from evaluation with the sphere target. The performance is based on parameters extracted from the 60mm prolate spheroid target set with single-site parameter extraction. The top panel represents performance with the full target set. The bottom panel is for the reduced target set.**

#### 4.2.14 Single-Site Data – Prolate Spheroid Target

Using the 60mm prolate spheroid (PS) as a target model, we evaluated the performance of the 3 arrays showing the best performance based on the sphere target (3T5C-30, 3T5C-35, and 3T7C-MM). We present those results in Figure 4.20. As with the sphere target, we have evaluated the arrays for both the full target set (Figure 4.20 top panel) and for the reduced target set (Figure 4.20 bottom panel).

The results in Figure 4.20 confirm with a second target geometry that the current MetalMapper array geometry is better than the best of the arrays having 5 3-C receivers. Note, however, that on the reduced target set (Figure 4.20 bottom panel) the overall performance of the 3 arrays is almost identical with the MetalMapper maintaining a slight edge. We think this is due to improved performance of the MetalMapper on those targets having larger horizontal offsets. And notice too that the difference in performance comes largely from the ability to extract better estimates of the “Shape A” parameter (target aspect ratio  $P_{0R}$ ) with data from the MetalMapper array.

We have combined the performance of the 3 arrays for the sphere target set (Figure 4.19 and the prolate spheroid target set (Figure 4.20) into a set of bar graphs summarizing the performance when considering both targets. Those results are shown in Figure 4.21. Here again, the 3T7C-MM clearly retains its performance advantage against the 2 competing 5 cube systems, particularly when considering the full target sets. But when using the reduced target set and thus eliminating all targets with offsets outside the 0.4m limit, the 5-Cube arrays do better with the

3T5C-30 array performing marginally better than the 3T5C-35 system that has its receivers 7 cm farther away from the center.

#### 4.2.15 Multi-Site Performance

In principle, measurements taken at several positions (“sites”) over the targets should vastly improve the fidelity (i.e., performance) of the modeling program used target parameter extraction when the program is capable of processing multi-site data sets. MMTTargets has multi-site inverse modeling capability for a single (dipole) target source. We used the multi-site capability to study performance under the scenario that we have experienced repeatedly in our demonstrations at San Luis Obispo, Butner, and most recently at Mare Island. The scenario is that our first measurement indicated that the target is offset by more than 0.4m from the center of the MetalMapper array. A second data site was placed at the target position estimated from the original measurement. Thus, we have data available over (hopefully) a single target at 2 different surface sites.

We evaluated the performance of 2-Site data sets using the sphere target and the MetalMapper array. The two target sites are noted in Figure 4.11 (“Primary” and “Secondary” observation sites). The primary site is located at the center of the spheroid whose octant volume contains the random target positions. The secondary site is offset laterally along the X axis by a distance of 0.5m. Together the measurements at the two site assure that one of the sites will be reasonably centered over the target. We evaluated performance for 2 cases:

1. **Perfect Position and Attitude** – In this case, the position and antenna attitude angles are assumed to be known perfectly.
2. **Reasonable Position and Noise Uncertainty** – In this case, we allowed for random errors in both the platform position ( $\sigma=2\text{cm}$  for all 3 coordinates) and random errors in the 3 attitude angles ( $\sigma=1^\circ$ ). The standard deviations used for these uncertainties are consistent with those reported for RTK GPS positioning and for the module that transduces attitude angles for the sensor platform.<sup>15</sup>

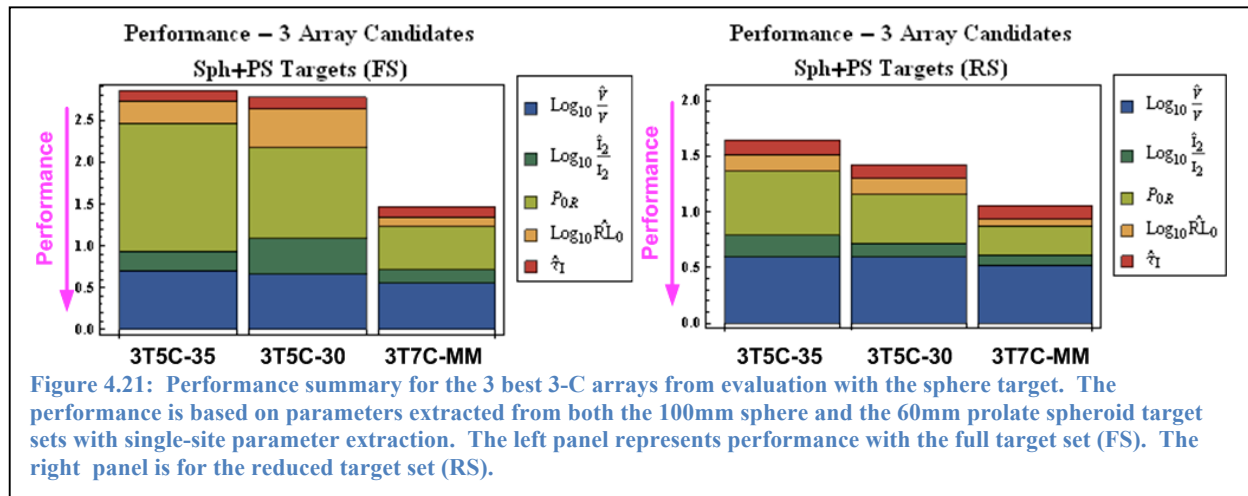
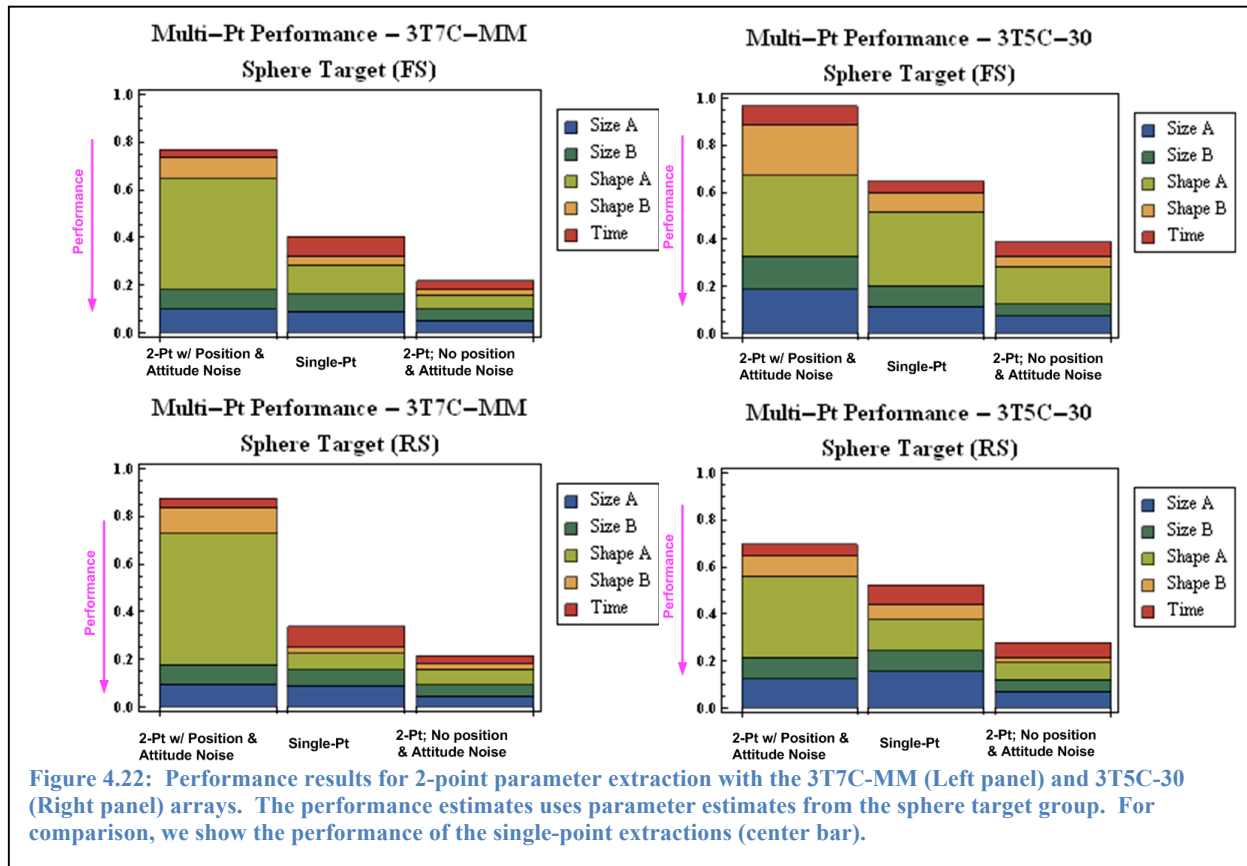


**Figure 4.21: Performance summary for the 3 best 3-C arrays from evaluation with the sphere target. The performance is based on parameters extracted from both the 100mm sphere and the 60mm prolate spheroid target sets with single-site parameter extraction. The left panel represents performance with the full target set (FS). The right panel is for the reduced target set (RS).**

<sup>15</sup> Platform pitch and roll angles have specified accuracies on the order of  $\pm 0.1^\circ$ . Unfortunately, the measurement error for the heading, which are based on vector measurements of the magnetic field, are an order of magnitude larger. We think that random angle errors having a standard deviation  $\sigma=1^\circ$  may in fact be optimistic.

The performance results for 2-site parameter extractions are shown in Figure 4.22 as stacked bar graphs. These results are shown for the 3T7C-MM and the 3T5C-30 arrays. For comparison, we have also included the performance (middle bar) for single-site parameter extraction for those arrays. These results show that 2-Pt and, more generally, multi-point parameter extraction can significantly improve performance. But this improvement can only be achieved when the precision of both platform attitude angles and positioning are perhaps an order of magnitude smaller than the uncertainties that we used for these evaluations.



#### 4.2.16 Conclusions– Optimum Array Study

In this study we have evaluated the performance of the existing *MetalMapper* array (357C-MM) against a set of candidate arrays having fewer tri-axial receivers (5). We have also investigated whether there is a significant benefit in deploying tri-axial receivers rather than a set of vertical receiver loops such as used in the BUD array. We emphasize that our conclusions relate to the efficacy of the arrays for static measurements. However, earlier studies that we have cited strongly suggest our conclusions extrapolate to the case of dynamic measurements with an array containing a single Z transmitter and an array of tri-axial receivers. Our results lead to the following conclusions:

1. The MetalMapper with its present 7-Cube receiver array performs significantly better than the 5-Cube symmetrical receiver arrays regardless of receiver spacing. However, if we restrict our target space to a volume such that shallow targets are never offset horizontally farther than 0.4m from the array center, the array 3T5C-30 has performance that is not significantly degraded from that of 3T7C-MM. We believe that the two tri-axial cube receivers located at coordinates (0.39,0.39) and (-0.39,-0.39) or about 55cm from the center of the array account for the improved performance of the MetalMapper array over its 5-Cube rivals.
2. The results show clearly that if we restrict ourselves to 5 tri-axial receivers, we should place those receivers along the diagonals at a distance of between 42cm-55cm from the array center. Our results show that 3T5C-30 (42 cm diagonal distance from center)

performs marginally better 3T5C-35 (49.5cm diagonal distance from center). Such a wide spacing is consistent with the optimum 1-C receiver placement as determined by Smith et al [4].

3. We conclude that there is a substantial benefit to making tri-axial measurements. This conclusion is made on the basis of the poor performance of the 3T7Z-MM array relative to its 3-C counterpart (3T7C-MM). Although we were not able to study the performance of the 2 other candidate 1-C arrays, we have no reason to believe that fewer 1-C receivers would surprise us by performing better than their 3-C counterparts. We note that array 3T7Z-MM performs better on the reduced target set. So in all probability, if we wish to use 1-C receivers, the penalty we will pay is that we will need to reduce the maximum permissible horizontal offset of the target from the antenna platform.
4. Our results show that the performance of these arrays is generally well characterized by using spherical targets. But there is some ambiguity in those results because the ranking of 3T5C-30 and 3T5C-35 depend on whether we are using the full set or the reduced set. However, when we composite the results from both the sphere target and the prolate spheroid the ranking of the 3 arrays is consistent between the full set and the smaller reduced set.
5. Admittedly, our efforts to evaluate the efficacy of multi-site parameter extraction were limited. Nevertheless, our experiments suggest that the performance of multi-site parameter extraction will be inferior to that of a single well sited measurement over the target unless we develop an efficient means for locating the platform with sub-centimeter accuracy and transducing its 3 attitude angles with  $0.1^\circ$  accuracy. This level of (internal) accuracy might be achieved by either moving the antenna array to precisely located positions on a rigid planar template, or, alternatively, employing an array (e.g. 2 x 2) of identical antenna arrays. Such an array would be similar in concept to the TEMTADs array.

#### 4.2.17 Recommendations for Further Study

There are a number of areas where further study would be useful.

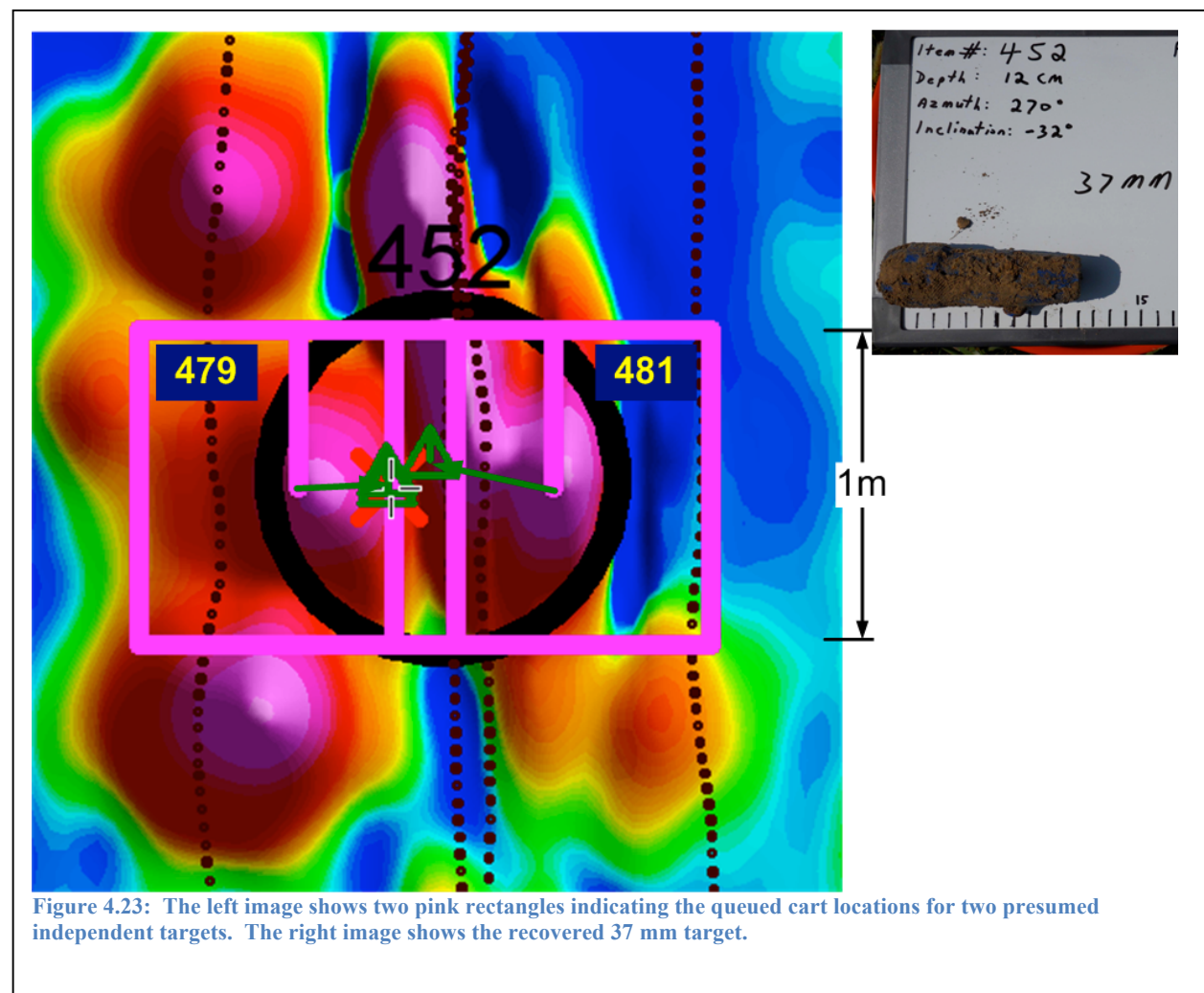
1. Our target sets were generated with a single noise level consistent with noise measurements at several demonstration sites. During analysis we discovered that we did not account properly for the noise reduction due to stack measurements ( $\sqrt{N}$ ). As a result, the noise levels were perhaps overly high. The high noise does not affect the relative rankings of the arrays since data sets for each array were generated with identical noise statistics. However, we would like to investigate different noise levels and how they affect the overall results.
2. We would like to extend the multiple site study in 2 ways. We would like to experimentally determine the required specification for both position and attitude accuracy such that multiple-site measurements (say 2 to 5 closely spaced sites) might

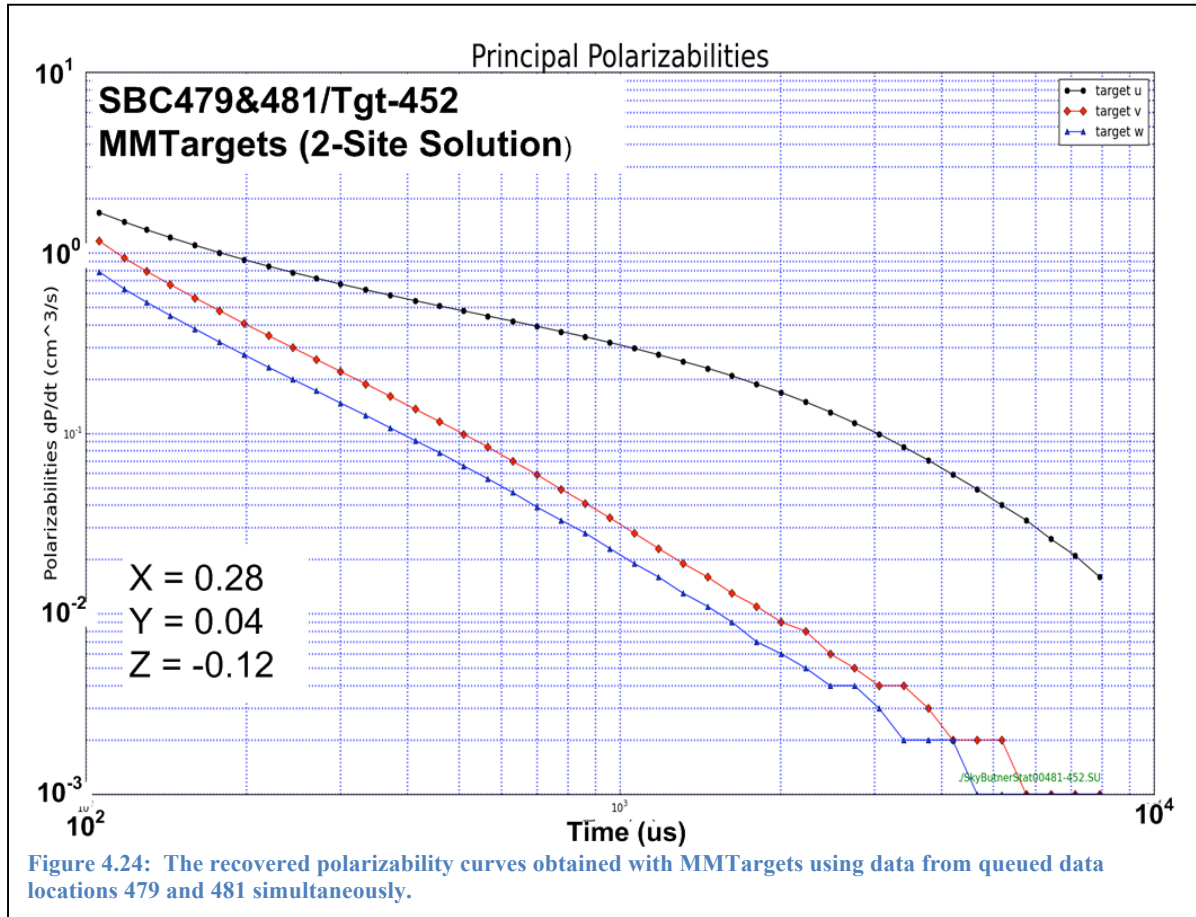
achieve the improved performance suggested by the results shown in Figure 4.22 for the case of no uncertainty in position and attitude for a 2-site data set. If we use more sites, can we relax the accuracy standards?

### 4.3 Parameter Extraction Using Multi-Point Data Sets (Task 3)

*MMTargets* was derived from ALLTEM-Double-Inversion, which was designed to operate on dynamically acquired data from the USGS ALLTEM system. *MMTargets* simply attempts to invert a model to fit the dataset it is directed to use. This can be a single static snapshot, multiple static snapshots, a segment from a single survey line of dynamically acquired data, or segments from several survey lines of dynamically acquired data (i.e. a patch of data). The USGS used only dynamic data, and extracted patches of data that were small, adjacent, survey line segments.

The multi-point inversion capability was demonstrated using synthetic data in Section 4.15 (Multi-Site Performance). Here, the capability is demonstrated by combining data from two survey locations at Camp Butner that were presumed to be two distinct targets (see Figure 4.23). After combining the data from the two survey points, *MMTargets* produces the polarizability curves shown in Figure 4.24. These curves clearly suggest that the target is rod-like; and this assertion was confirmed when a 37 mm ordnance was recovered.

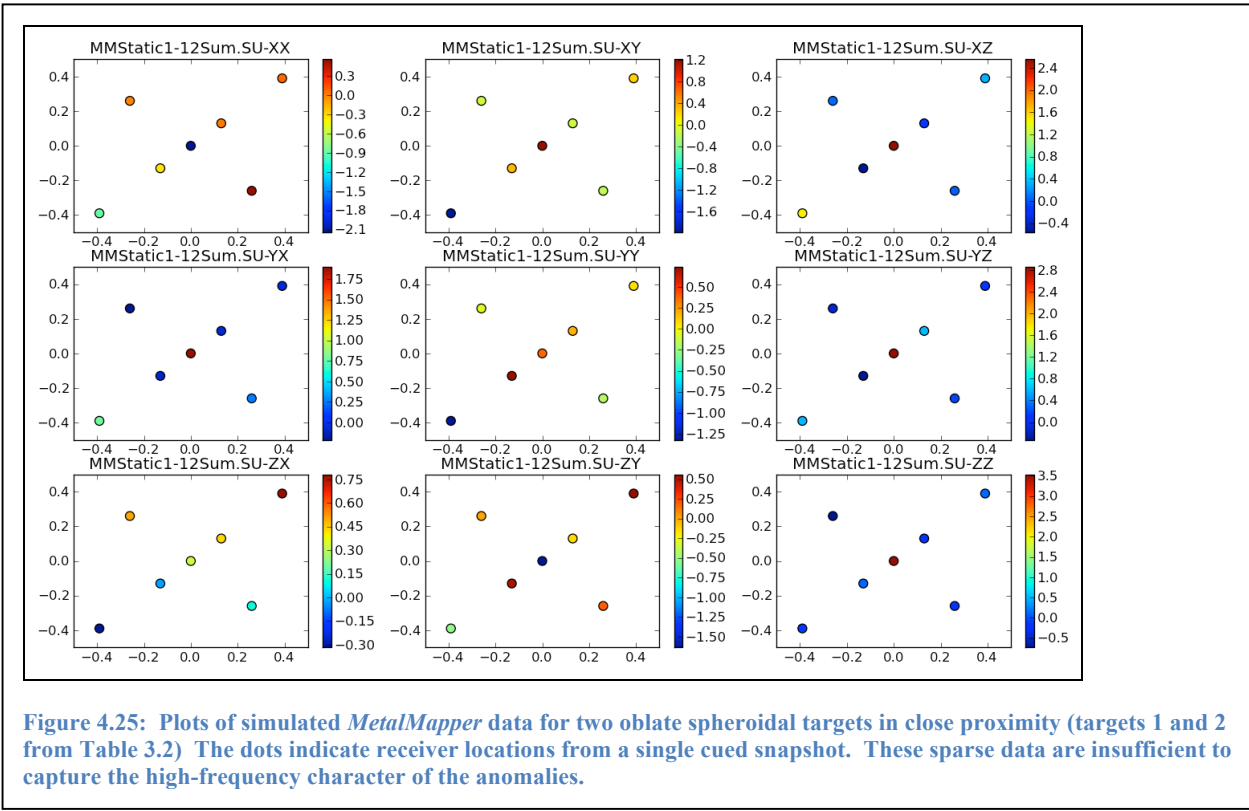




#### 4.4 Multiple Source Detection (Task 4)

Data from targets that cannot be fit using simple single-dipole models can either be clutter or multiple targets. Targets with a small volume and a poor fit to simple dipole models are likely clutter. If multiple models provide similar misfit metrics, this may indicate that a complex (non-dipole) target is present and more advanced analysis algorithms may be needed. However, targets with large volume and a poor fit to simple dipole models may be clutter or multiple objects in close proximity. This section considers the latter possibility. Note that some of the funds originally allocated for this task were redirected towards the integration of the previously discussed routines into *Oasis montaj*. Subsequently, the scope of this task has been reduced and testing of the routines in this section has not moved beyond simulated data.

Characterization and classification of objects in close proximity is a difficult task that is often exacerbated by sparse datasets. A single cued snapshot does not have sufficient spatial coverage and density for effective multi-target characterization and classification. This is illustrated in the figures that follow, which portray the behavior modeled fields from two prolate spheroid targets in close proximity. Table 4.2 contains the target parameters used in the simulation. In these plots, the dots mark receiver locations and the background colors represent field values at the receiver locations. Figure 4.25 shows synthetic data from a single cued snapshot, and Figure 4.26 includes additional snapshots that provide increased data density to help resolve the complex high-frequency nature of targets in close proximity. Note that some of the peripheral data points in Figure 4.26 still have a relatively large amount of energy.



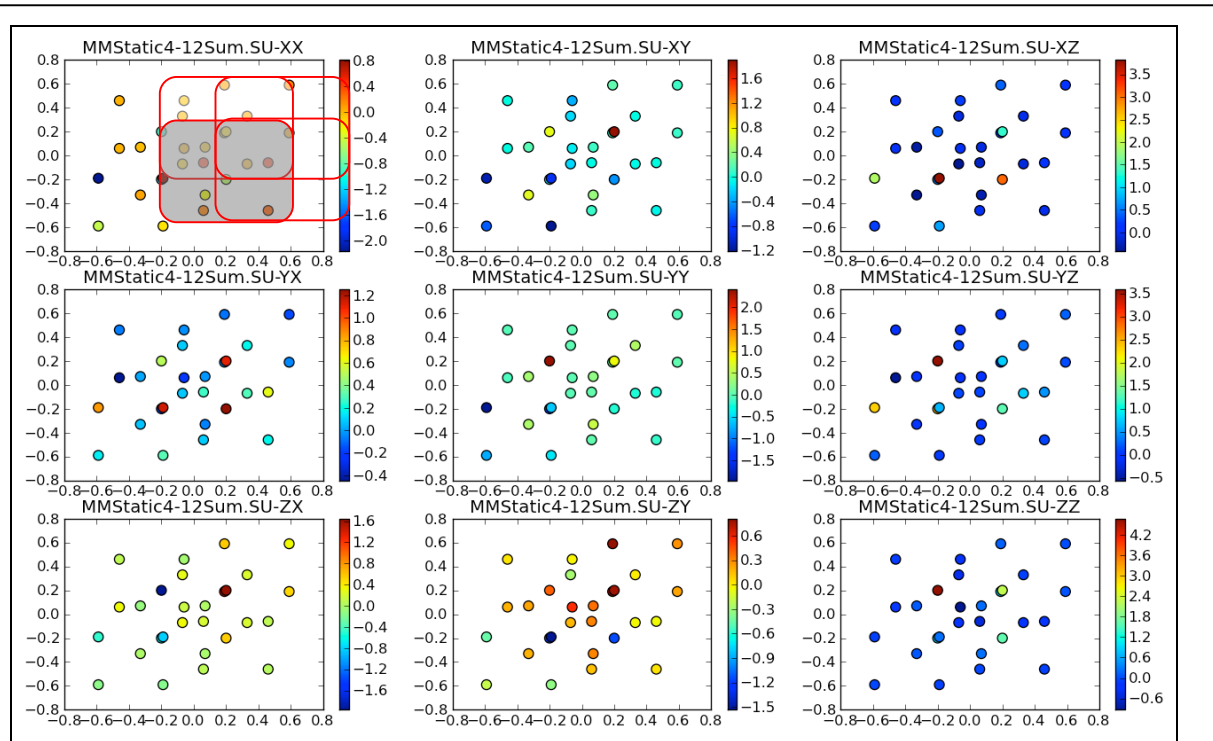


Figure 4.26: Plots of simulated *MetalMapper* data for two oblate spheroidal targets in close proximity. Black dots indicate receiver locations from four cued snapshots. The shaded region shows the footprint of the *MetalMapper* cart. These data are sufficient to capture the high-frequency character of the anomalies.

Table 4.2. Target parameters used to generate modeled data for testing frequency-domain filters and multiple inversion algorithms.

Target	$\sigma$ (S/m)	$\mu_r$	$x$ (m)	$y$ (m)	$z$ (m)	$r_{axial}$ (m)	$r_{transverse}$ (m)	$\alpha$ (deg. az.)	$\beta$ (deg. inc.)
1	$10^7$	150	0.15	-0.10	-0.24	0.451	0.025	10	-23
2	$10^7$	150	-0.10	0.17	-0.20	0.451	0.025	150	73
3	$10^7$	150	0.6	1.15	-0.20	0.451	0.025	0	0, 90
4	$10^7$	150	0.4	1.35	-0.20	0.451	0.025	0	0, 90
5	$10^7$	150	0.1	0.15	-0.20	0.451	0.025	30	45
6	$10^7$	150	-0.1	-0.15	-0.20	0.451	0.025	120	-45

#### 4.4.1 Reduction-to-Pole and Downward Continuation

Song et al. [7, 8] have shown that the success of multi-target inversions is critically dependent on high-quality starting models. Song attacked this problem by Monte Carlo generation of potential

starting models, and using those models whose simulated data reasonably fit the actual data. The present work attempts to reduce this time-consuming process by selecting starting models from filtered datasets. Two filtering methods are used: reduction-to-pole and downward continuation. The goal of these methods is to reduce the interference that occurs with the fields generated by objects in close proximity, and to provide high-quality starting models and constraints for multi-target inversion routines. The benefit of the reduction-to-pole algorithm is that it centers the anomaly over the causative body. For surveys that do not have transmitter coils directly over the target, this method will center the anomaly over the target. The downward continuation routine calculates the field distribution that would occur if the survey instrument were placed at a level closer to the target. This reduces the interference between fields for objects in close proximity. The downside to the routines is that they can generate noise and artifacts. Results from these routines are used to pick high-quality starting models for the multi-target inversion and to provide added constraints for the target's lateral position.

The frequency-domain operations described in this section require a dataset with sufficient density to enable Fourier transforms. Here it is heuristically demonstrated that two adjacent passes of dynamic *MetalMapper* data have sufficient data density to employ a non-uniform discrete Fourier transform, and that spatial frequency-domain techniques can be employed. Figure 4.27 shows simulated data plots for two proximal targets, and Figure 4.28 shows the same data after forward and reverse non-uniform discrete Fourier transforms. Although there is some distortion of the original data, the transformed data is reasonably close to the original data and warrants using the non-uniform Fourier transform for frequency-domain processing. Traditional Fourier transform techniques require data on a uniform grid. For non-uniform survey data, one can grid the data onto a uniform grid before invoking a traditional Fourier transform. For the problem at hand, we would need to grid both the calculated transmitted field and the measured received fields for all coils. This would markedly increase the amount of data to be processed, so an alternative method is formulated that operates directly on the existing data with a non-uniform Fourier transform.

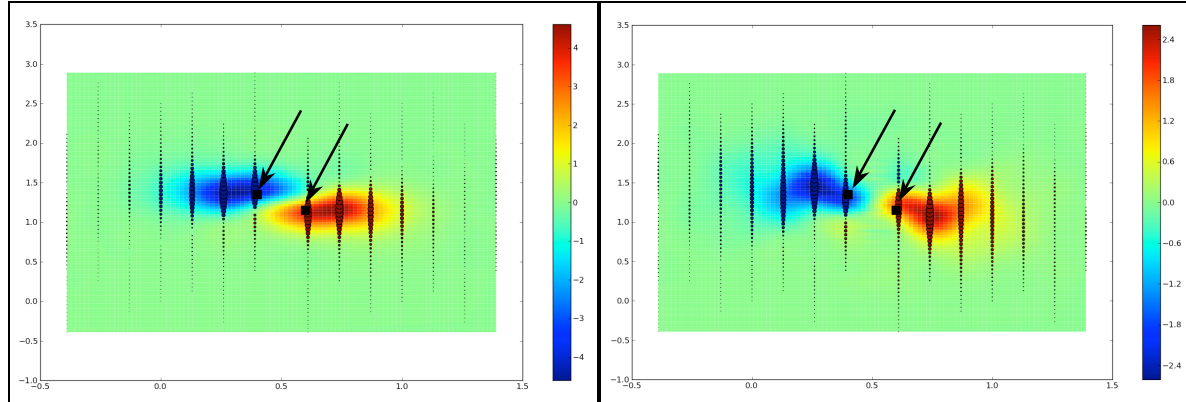


**Figure 4.27:** Left: original image from two vertically oriented oblate spheroid targets (target 3 and 4 from Table 4.2). Right: original image from two horizontally oriented oblate spheroid targets (target 5 and 6 from Table 4.2). Colored dots indicate receiver locations, and large black dots (and arrows) indicate true target positions. These maps simulate data acquired along two adjacent profiles offset by a distance of 1m.

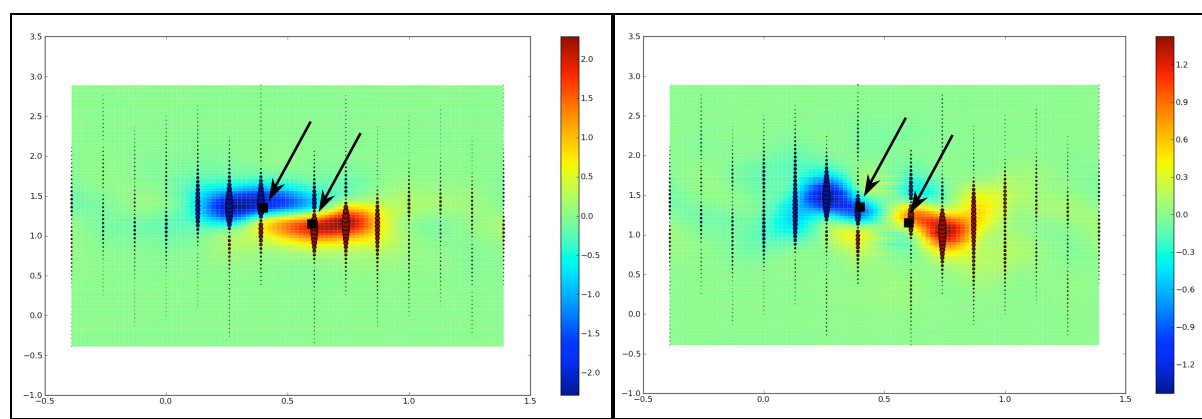


**Figure 4.28: Images resulting from application of non-uniform Fourier transform followed by uniform inverse transform. Left: image from two vertically oriented oblate spheroid targets (target 3 and 4 from Table 4.2). Right: image from two horizontally oriented oblate spheroid targets (target 5 and 6 from Table 4.2). No window function was used. Colored dots indicate data points, and large black dots (and arrows) indicate true target position.**

Downward continuation is a process that attempts to calculate the fields that would be measured if the survey plane were closer to the target. In effect, fields are calculated that would have been measured if the survey were conducted at a lower elevation that was closer to the target. Being closer to the target reduces the interference between fields produced by objects in close proximity. For objects oriented at an oblique angle, the measured field anomalies can be skewed off-center from the horizontal target location. Downward continuation can also move the anomaly closer to the true horizontal location of the target.

If the primary field does not have vertical polarization when energizing a target (or if the dipole magnetization dips at an oblique angle), then the measured field anomaly will be skewed off-center from the horizontal target location. Since the polarization of the primary field at the target rotates as the cart moves, many polarizations are used to excite the target. Reduction-to-pole is a process that calculates the anomaly that would be measured if the primary field were vertical. This method centers the measured energy over the target.

This section provides a brief mathematical presentation of the frequency-domain routines, and presents results that illustrate the effectiveness of these methods. To the author's knowledge, a reduction-to-pole algorithm suitable for EMI data has not been previously reported. In the frequency-domain analysis presented below, the spatial frequency variables are obtained from the characteristic equation, with Eigenvalues  $\lambda_i$ , for the Laplace's equation. See Appendix A for more background on the notation and formulation [9]:

$$k^2 \equiv \lambda_x + \lambda_y + \lambda_z = (ik_x)^2 + (ik_y)^2 + (k_z)^2 = (ik_\rho)^2 + k_z^2 = 0 \quad (4.10)$$

where  $k_\rho^2 = k_x^2 + k_y^2$ , (x-y in horizontal plane, z is vertical) which leads to

$$k_z = |k_\rho|. \quad (4.11)$$

Beginning with the field of a dipole target in the spatial domain:

$$\vec{\mathcal{B}}_{dipole} = -\vec{\nabla}V = \frac{-\mu_0}{4\pi} \vec{\nabla} \left[ \vec{m} \cdot \vec{\nabla} \frac{1}{r} \right], \quad (4.12)$$

the fields on a plane above the target at the origin can be written in the frequency-domain so the depth ( $z$  positive up) and the  $x$ - $y$  dependencies are separated:

$$\vec{B}_{dipole} = -\vec{\nabla}V = \frac{-\mu_0}{4\pi} \vec{\nabla} \left[ \vec{m} \cdot \vec{\nabla} \left[ \frac{2\pi e^{|k_\rho|z}}{|k_\rho|} \right] \right], \quad (4.13)$$

$$\vec{B}_{dipole} = -\vec{\nabla}V = \frac{-\mu_0 m}{2} \vec{\nabla} \left[ im_x k_x + im_y k_y + m_z |k_\rho| \right] \frac{e^{|k_\rho|z}}{|k_\rho|}, \quad (4.14)$$

and finally

$$\vec{B}_{dipole} = \frac{-\mu_0 m}{2} \left( ik_x \hat{x} + ik_y \hat{y} + |k_\rho| \hat{z} \right) \left[ im_x k_x + im_y k_y + m_z |k_\rho| \right] \frac{e^{|k_\rho|z}}{|k_\rho|} = \vec{G}_0(\vec{k}, z, \vec{m}). \quad (4.15)$$

A dipole source at an arbitrary location is given by phase shifting a source from the origin

$$\vec{B}_{arb} = e^{i(k_x x' + k_y y') - |k_\rho| z'} \vec{G}_0(\vec{k}, z, \vec{m}) = \vec{G}(\vec{k}, z, \vec{m}, \vec{r}'), \quad (4.16)$$

so that the magnetization of an arbitrary collection of dipoles is

$$\vec{B}_{anom} = \sum_n \vec{G}(\vec{k}, z, \vec{m}_n, \vec{r}_n). \quad (4.17)$$

If the induced magnetization by the primary field is assumed to be uniform, than the single dipole Green's function can be factored out:

$$\vec{B}_{anom} = \vec{G}_0(\vec{k}, z, \vec{m}) \sum_n e^{i(k_x x'_n + k_y y'_n) - |k_\rho| z'_n} \quad (4.18)$$

Reduction-to-pole takes the form

$$\vec{B}_{RTP} = \vec{B}_{anom} \frac{|k_\rho|}{im_x k_x + im_y k_y + m_z |k_\rho|}, \quad (4.19)$$

and downward continuation is simply

$$\vec{B}_{DC} = \vec{B}_{anom} e^{|k_\rho| \Delta z}, \quad (4.20)$$

where  $\Delta z$  is the downward continuation distance. Finally, both of these operations can be combined

$$\vec{B}_{RTP,DC} = \vec{B}_{anom} \frac{e^{|k_\rho| \Delta z} \cdot |k_\rho|}{im_x k_x + im_y k_y + m_z |k_\rho|}. \quad (4.21)$$

Conventional reduction-to-pole routines usually require a fixed direction for the primary field. For EMI data, the orientation of the primary field at the target changes with cart location and transmitter coil orientation. To work with changing primary field polarizations, the frequency-domain phase shift in equation 6.10 can be incorporated into the Fourier transform used to move from the space-domain to the frequency-domain. The discrete Fourier transform projects the space-domain data onto frequency-domain basis functions, and each sample point in the space-domain has a frequency-domain representation. Since the primary field at each spatial location is different, a different phase shift factor multiplies each sample point in the frequency-domain before it is summed:

$$B(k_x, k_y) = \sum_i B(x_i, y_i) S_{RTP} e^{i(k_x x_i + k_y y_i)}, \quad (4.22)$$

where  $S_{RTP}$  is the phase shift factor. The changing phase shift factor is applied to each data point in the space-domain before calculating the Fourier transform. Changing the order of operations is permissible for uniformly convergent functions.

In practice, both reduction-to-pole and downward continuation can introduce artifacts in the data, and can produce nonsensical results if misapplied. Reduction-to-pole has well-known difficulties when the magnetization direction approaches horizontal. Therefore, only data recorded with the z-axis transmitters and receivers are used, and then only when the primary field inclination at the target is greater than 5 degrees. The difficulties with downward continuation arise because the method is essentially a high-pass filter, which can accentuate high frequency noise and introduces artifacts. Consider that the spectrum of a dipole source is band-limited, and as the observation point moves farther from the source the high frequency energy is reduced (see Figure 6.5). Therefore, the classical dipole spectrum can be used as a limiter during the downward continuation process.

The reduction-to-pole and downward continuation methods have been implemented in a *Python* script. *Python* is a free and open-source language similar to Matlab with many scientific libraries. These routines were applied to the data presented in Figure 4.27 Figure 4.28. For calculating the primary fields, the reduction-to-pole routine requires a target position. The centroid of the anomaly was used for the lateral target position, and 0.25 m was used for the depth. The reduction-to-pole results are shown in Figure 4.30 where the anomaly peaks have been moved very close to the actual target location (compare with anomaly peak locations in Figure 4.27 and Figure 4.28). Figure 4.31 shows the results of downward continuation for 10 cm. To an extent, the anomaly energy has moved closer to the actual target locations, but some unwanted artifacts are beginning to appear. Figure 4.32 shows the combination of both reduction-to-pole and downward continuation. The anomaly peaks are very close to the actual target positions, but there are many unwanted artifacts. Low-pass filtering may reduce some of

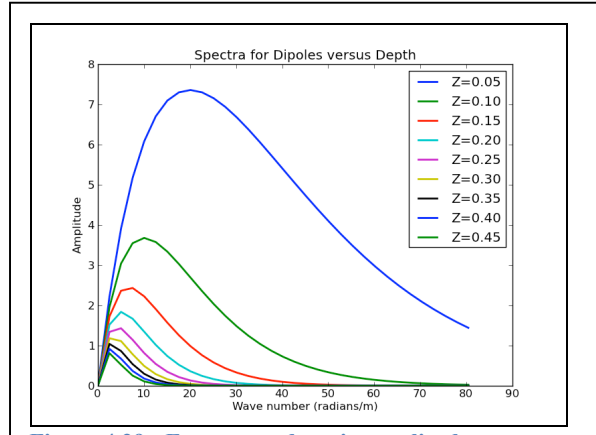


**Figure 4.29: Frequency-domain amplitude spectra for dipoles at various depths. The amplitude spectra are independent of dipole orientation.**

these artifacts, but noisy data will cause them to increase. While both reduction-to-pole and downward continuation each help to provide better estimates of target location, the best results have been achieved using reduction-to-pole with no downward continuation. These preliminary results suggest that more accurate starting models for multi-target inversion can be obtained with these methods.

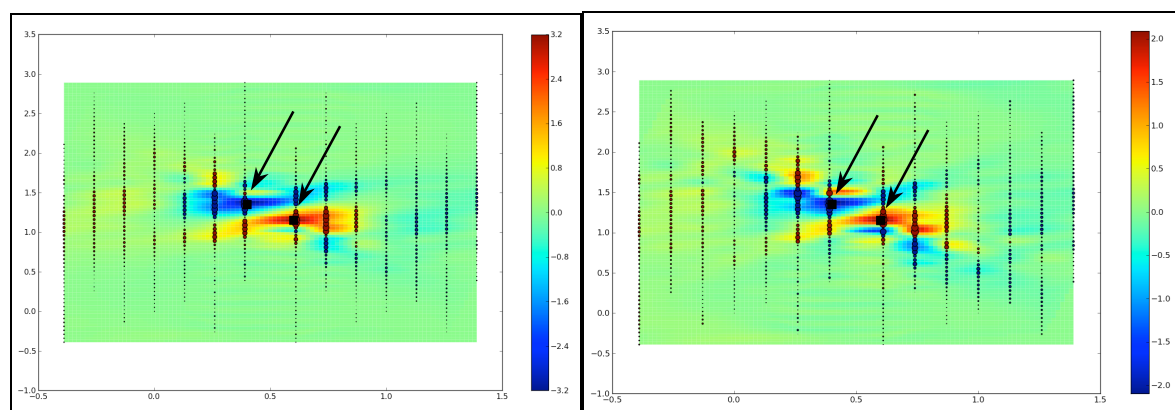


**Figure 4.30:** Images resulting from the reduction-to-pole routine. Left: image from two vertically oriented oblate spheroid targets (target 3 and 4 from Table 6.1). Right: image from two horizontally oriented oblate spheroid targets (target 5 and 6 from Table 6.1). Colored dots indicate data points, and large black dots (and arrows) indicate true target positions. Energy peaks are now very close to actual target locations.

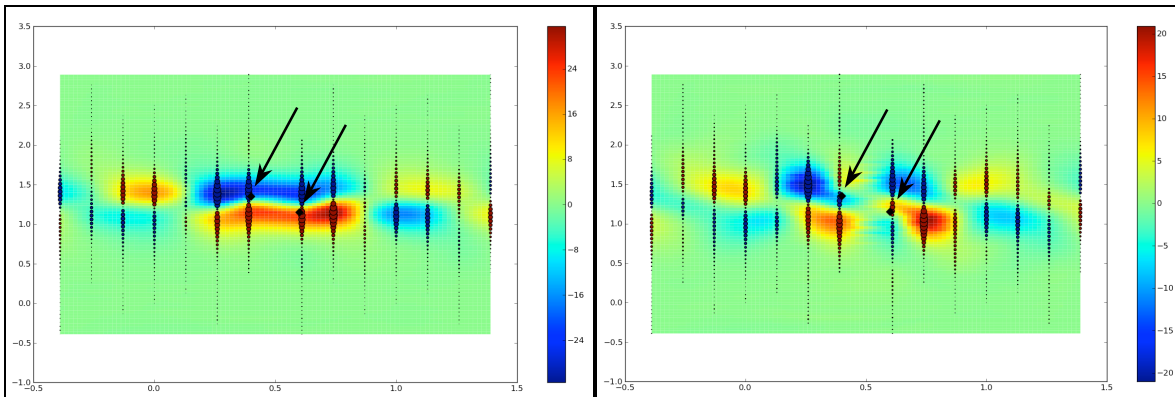


**Figure 4.31:** Images resulting from application downward continuation routines. Left: image from two vertically oriented oblate spheroid targets (target 3 and 4 from Table 3.2). Right: image from two horizontally oriented oblate spheroid targets (target 5 and 6 from Table 3.2). Colored dots indicate data points, and large black dots (and arrows) indicate true target positions.

Gridding the data before reduction-to-pole or downward continuation may reduce artifacts, but the calculations will require substantially more memory and longer run times. Thus far, the routines have been written in *Python*, which runs slowly compared with code compiled into native machine language such as C or C++. It is recommended that these routines be rewritten in a faster language.

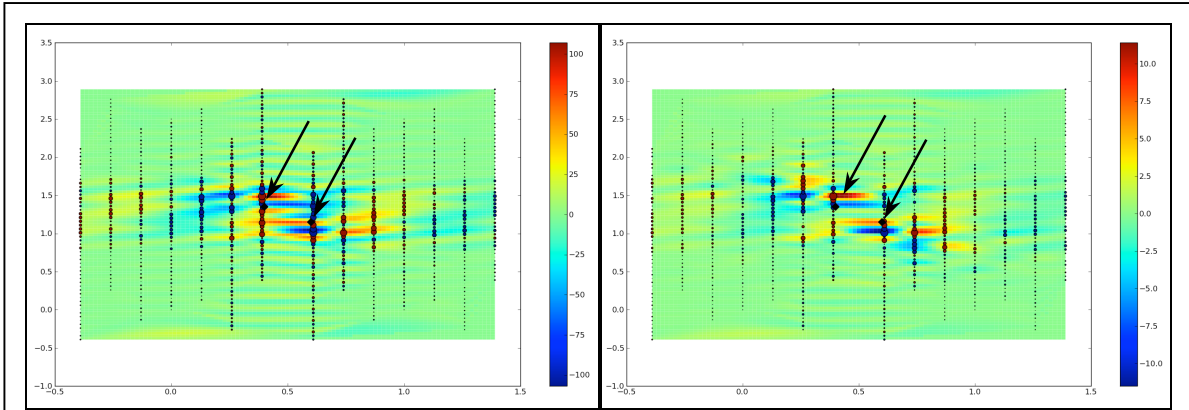


Figure 4.32: Images resulting from application of both the reduction-to-pole and downward continuation routines. Left: image from two vertically oriented oblate spheroid targets (target 3 and 4 from Table 3.2). Right: image from two horizontally oriented oblate spheroid targets (target 5 and 6 from Table 3.2). Colored dots indicate data points, and large black dots (and arrows) indicate true target positions. Energy peaks are very close to target locations.

#### 4.4.2 Multi-Target Inversion

Inverting for multiple targets is challenging for several reasons. First, there are more parameters to solve for. Second, all of the parameters have a non-linear relationship with the data (when target locations are unknown). Once the locations of the targets are known, the size and orientation can be determined by solving a linear problem. Nevertheless, knowledge of the approximate horizontal target position can significantly improve the performance of multi-target inversion routines.

Several groups have been experimenting with multiple target solvers. Song et al. [7,8] use a Monte Carlo method to find starting models with a reasonably good data misfit, and then polished the parameter estimates using conventional decent inversion techniques. Keiswetter [10] uses a Monte Carlo technique to generate an initial population of models, then selects the best combination from this population, and finally iterates this process as needed. Shubitidze et al. [11] characterizes targets using ortho-normalized volume magnetic sources. Song et al. [12] uses the MUSIC algorithm to determine multiple target positions, and then applies a joint diagonalization method to estimate their shape. In addition to MUSIC, statistical methods such as independent component analysis and blind source separation can be applied [13]. A combination of physical constraints such as downward continuation and Green's function relationships with statistical measures such as independence should be investigated.

Because this project was multi-faceted, the limited resources for a particular task constrained most developments to be incremental improvements on existing routines. Therefore, for the multi-target inversion we examine methods that did not require coding a complex routine from scratch. Rather, we attempted to extend the capabilities of the existing *MMTargets* inversion routines. This involved two different approaches. The first is a simple target stripping procedure and the second is the interleaved multi-target solver.

The simple target stripping approach was investigated by creating a *Python* script to invert for two targets, one at a time. The process starts by constraining the lateral position of the targets based on the reduction-to-pole and downward continuation methods discussed previously. Then a single target inversion attempts to fit the data, and the residual dataset is calculated by subtracting the modeled data for the best-fit target. Finally, another single target inversion is run to fit a second target to the residual data. The results for two targets in close proximity at the same depth were poor. When trying to fit one target to a multiple target dataset, the depths are over estimated because the lateral extent of multiple targets is greater than individual targets and

**Table 4.3. Single-target inversion results (unconstrained positions) and true values from repeated from Table 6.1.**

Queued Points	Target	$x$ (m)	$y$ (m)	$z$ (m)	$r_{\text{axial}}$ (m)	$r_{\text{transverse}}$ (m)	$\alpha$ (az.) (deg)	$\beta$ (inc.) (deg)	MSE (%)
	1 (true)	0.15	-0.10	-0.24	0.451	0.025	10	-23	
	2 (true)	-0.10	0.17	-0.20	0.451	0.025	150	73	
1	1+2	-0.068	0.171	-0.276	0.045	0.044	220	-55.5	3.7
4	1+2	0.123	0.345	-0.275	0.051	0.037	227	65.5	3.4
	5 (true)	0.1	0.15	-0.20	0.451	0.025	30	45	
	6 (true)	-0.1	-0.15	-0.20	0.451	0.025	120	-45	
1	5+6	0.014	0.010	-0.301	0.060	0.041	168	-45	3.3
4	5+6	0.209	0.210	-0.285	0.059	0.038	169	-51	3.4

the inversion incorrectly tries to fit a target that is too deep to better match the data. While there may be some cases where this method provides reasonable results, the performance was unsatisfactory for cases tested in this report. Therefore, we do not recommend further study for this method.

The interleaved solver takes a different approach. Because the cost to invert a dense matrix scales as  $O(n^2)$ , doubling the number of targets increases processing time by a factor of four for each iteration. Rather than doubling the number of parameters for a dual target system, the *MMTargets* multi-target inversion routine considers the contribution of only one target at a time. As the inversion routine iterates, it refines the parameter estimates for one target at a time, and repeatedly cycles through the entire list of targets. In the limit of iterative parameter updates shrinking to zero, this method is exactly equivalent to a simultaneous multi-target solver using the Gauss-Newton method. In practice, the iterative parameter updates are small, so this method reasonably approximates a simultaneous multi-target solver. With this method, doubling the number of targets only increases the solver run time by a factor of two. However, results show that it is very likely that iteratively improving the parameter estimates for a given set of starting models will reduce the data misfit to a local minimum. To address this problem, one can either specify a large number of initial models, or *MMTargets* can generate these models randomly.

To evaluate solver performance, simulated data from target pairs from Table 4.2 were summed together. Table 4.3 lists solver results from the single target inversion. For single target

inversions, two different starting models were used with essentially no constraints on parameter ranges. For the multi-target interleaved solver, two initial models were used and subsequent models (100 in total) were selected randomly (genetic mutation is also supported) until a new model with a mean squared error (MSE) less than 90% was found. The proper horizontal position of the targets was given in the initial models and were only allowed to vary by +/- 1 cm. The results are listed in Table 4.4 for both a single queued snapshot and for four queued snapshots. The MSE of the multi-target solver is significantly less than those of the single target solver. The estimated depths are not unreasonable, but vary by up to about 10 cm. The shape and orientation attributes are incorrect. The low MSE indicates that the data were fitted reasonably well (real data with misfits of 2-3% are typical). This leads to the conclusion that the multi-target problem is ill-posed, and there are many models that reasonably fit the data.

The following conclusions and recommendations can be made for the multiple targets problem based on the test cases presented earlier in this Section.

1. Without lateral position constraints, the interleaved solver does not converge to an acceptably small MSE. Lateral position constraints such as those offered by the reduction-to-pole routines are necessary for reasonable multi-target inversion performance.
2. The multi-target inversion routines and frequency-domain filters have only been tested with modeled data with no noise. A much more thorough evaluation is needed using noisy data and actual survey data.
3. Although the multi-source inversion problem is ill-posed, the routines developed for this project have provided reasonable location and volume estimates for the cases tested.
4. Results show that the data misfits (MSE) for single static snapshots are similar to those from multiple queued snapshots.
5. In addition to MUSIC, many statistical methods such as independent component analysis and blind source separation may be leveraged [13] to help solve the multiple source problem. A combination of physical constraints such as downward continuation and Green's function relationships with statistical measures such as independence should be investigated.
6. At each Gauss-Newton iteration, the interleaved solver attempts to perform a step-wise optimization of the estimated target parameters based on the data misfit. For the multi-target problem, local minima are reached very frequently. When a local minimum is reached, a new set of parameters is created via Monte Carlo. Since the Gauss-Newton optimizations oftentimes does not make substantial progress toward a global solution, and since new starting models are found by Monte-Carlo, the routine is essentially a Monte-Carlo solver. This is very inefficient. In future work, we plan to develop and test a simultaneous multiple-target solver.
7. Choosing new starting models by genetic mutation rather than Monte Carlo gave inferior results.

8. The stripping method is not a viable method for multiple target inversion.

**Table 4.4. Multi-target inversion results (constrained lateral positions) and true values from repeated from Table 6.1.**

Queued Points	Target	$x$ (m)	$y$ (m)	$z$ (m)	$r_{axial}$ (m)	$r_{transverse}$ (m)	$\alpha$ (az.) (deg)	$\beta$ (inc.) (deg)	MSE (%)
	1 (true)	0.15	-0.10	-0.24	0.451	0.025	10	-23	
	2 (true)	-0.10	0.17	-0.20	0.451	0.025	150	73	
1	1:(1+2)	0.140	-0.090	-0.227	0.030	0.030	187	60.7	0.88
1	2:(1+2)	-0.099	0.162	-0.184	0.046	0.024	27.4	-77.1	0.88
4	1:(1+2)	0.140	-0.090	-0.250	0.051	0.029	162	22.1	0.59
4	2:(1+2)	-0.110	0.180	-0.161	0.041	0.024	156	65.7	0.59
	5 (true)	0.1	0.15	-0.20	0.451	0.025	30	45	
	6 (true)	-0.1	-0.15	-0.20	0.451	0.025	120	-45	
1	5:(5+6)	0.090	0.150	0.204	0.047	0.026	358	27.4	1.3
1	6:(5+6)	-0.090	-0.152	-0.250	0.039	0.037	239	5.6	1.3
4	5:(5+6)	0.090	0.140	-0.222	0.047	0.028	202	-35.6	1.5
4	6:(5+6)	-0.090	-0.140	-0.250	0.047	0.033	117	-45.0	1.5

#### 4.5 Oasis Montaj Integration (Task 5)

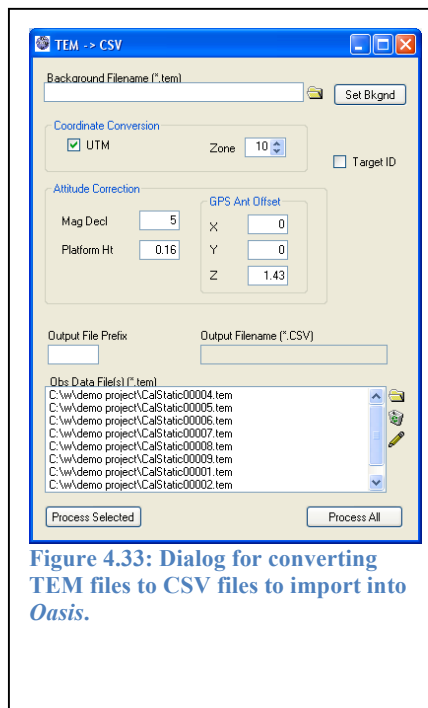
The task of integrating some of the routines from this project into *Geosoft's Oasis montaj* was added to the project base on a suggestion from the program office during an IPR. The integrated routines are separated into two groups. This first group contains the data import and detection routines for dynamic data. These routines were created by G & G Geosciences, Inc., and are outlined in their report. The second group contains automated *MetalMapper* data import routines for static data, and automated single target inversions by *MMTargets*. This group of routines is available to *Oasis montaj* users via the *UX-Targets* menu. There are four menu items in the *UX-Targets* menu:

- Convert TEM files to CSV format
- Convert TEM noise files to SU format
- Import ASCII Target Snapshot Data
- Characterize Targets

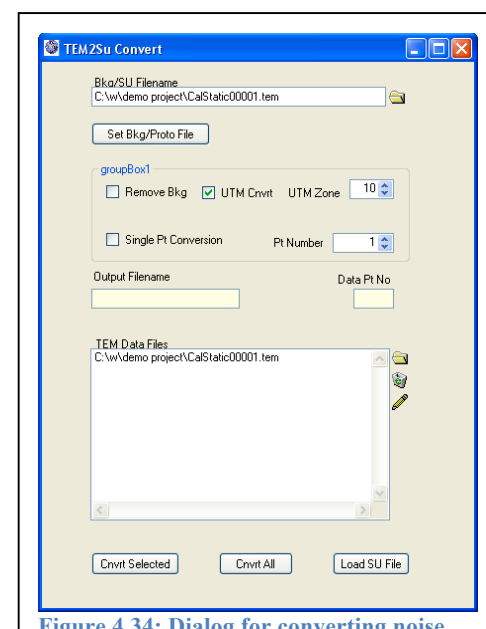
The remainder of this section presents a brief overview of the *UX-Targets* routines. A *UX-Targets* user manual is available with more detailed information.

The first three menu items are used to streamline importing large *MetalMapper* datasets into *Oasis*. During a re-acquisition survey, a large number of TEM files will be generated – one or more files for each target in the re-acquisition list. Importing these data is a three-step process. First the binary TEM files are converted to

ASCII so they can be imported by *Oasis*. Invoking the Convert TEM files to CSV format presents the dialog shown in



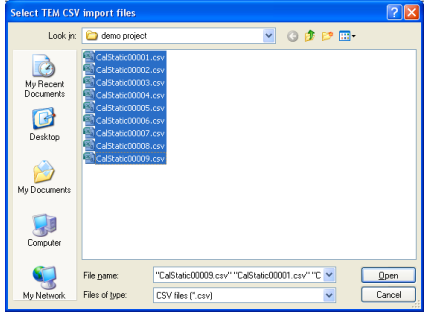
**Figure 4.33:** Dialog for converting TEM files to CSV files to import into *Oasis*.



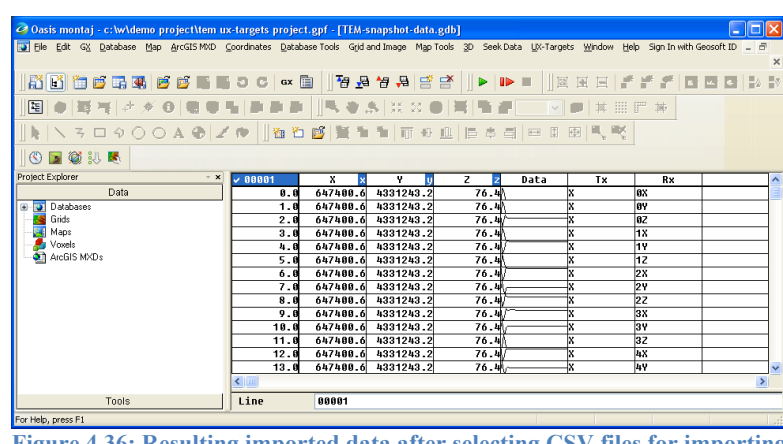
**Figure 4.34:** Dialog for converting noise file from TEM to SU format for *MMTargets*.

Figure 4.33. The user simply drags and drops all of the files to be converted onto the dialog. Enter the other information requested by the dialog and press Process All. The result will be a group CSV files, one for each TEM file. Next, *MMTargets* requires a TEM data file from a target free location so that it can estimate the EM noise level in the data. This is done with the Convert TEM noise files to SU format menu item. Enter the files names in the dialog as shown in Figure 4.34 and press Cnvrt All. In the final step, all of the data are imported into *Oasis* using the Import ASCII Target Snapshot Data menu item (see

Figure 4.35 and Figure 4.36.) Because all the data import routines operate on the entire list of files in the survey, the data import process is quite efficient.

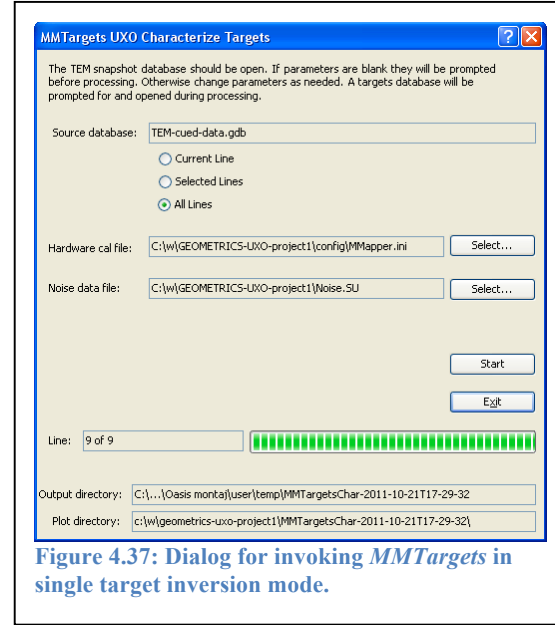


**Figure 4.35: Selecting CSV files for importing into *Oasis*.**



**Figure 4.36: Resulting imported data after selecting CSV files for importing into *Oasis*.**

The final menu item, Characterize Targets, starts the single target inversion process (see Figure 4.37). The inversion routine is run for all selected targets, and the results are placed in the targets database (see Figure 4.38). *MMTargets* generates a rich set of target properties that can be used in the discrimination process, which are listed in Table 4.5. Also, a summary plot as shown in Figure 4.39 is generated for each target with the principal polarizability curves and some import target parameter estimates. These plots can be quickly scanned using the *Microsoft Windows Picture Viewer* application. Because the dialog allows selection of all of the queued snapshots, the entire dataset can be processed with very little human interaction. *MMTargets* has a large number of user-configurable setting that control how the program processes and inverts each dataset. These settings are configured using keyword parameters defined in an INI file. The detailed function of each key word is beyond the scope of this report. For more details, users are referred to the *MMTargets* user manual.



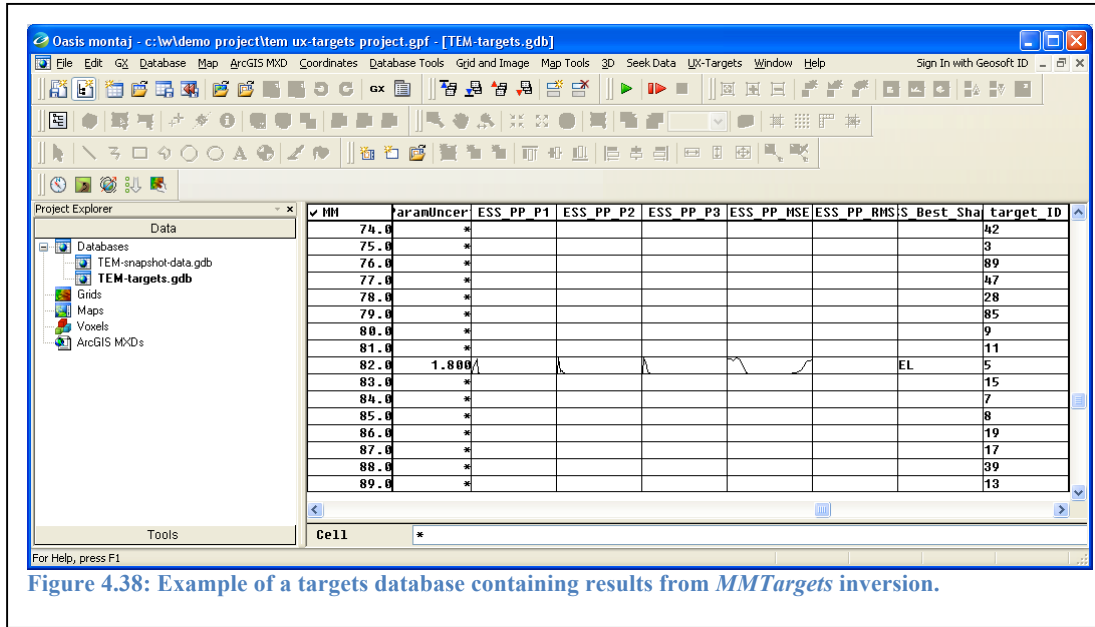


Figure 4.38: Example of a targets database containing results from *MMTargets* inversion.

Table 4.5: *MMTargets* single target properties list.

Target Type	Property	Description
Sphere	x, y, z	Target location
	r1, r2, r3	Principle axis radii
	azimuth, inclination	Target orientation
	MSE	Mean squared error between the modeled data and the actual data
Oblate spheroid	x, y, z	Target location
	r1, r2, r3	Principle axis radii
	azimuth, inclination	Target orientation
	MSE	Mean squared error between the modeled data and the actual data
Prolate spheroid	x, y, z	Target location
	r1, r2, r3	Principle axis radii
	azimuth, inclination	Target orientation
	MSE	Mean squared error between the modeled data and the actual data
Ellipsoid	x, y, z	Target location
	r1, r2, r3	Principle axis radii
	azimuth, inclination	Target orientation
	MSE	Mean squared error between the modeled data and the actual data
Best overall	x, y, z	Target location
	r1, r2, r3	Principle axis radii
	azimuth, inclination	Target orientation
	MSE	Mean squared error between the modeled data and the actual data

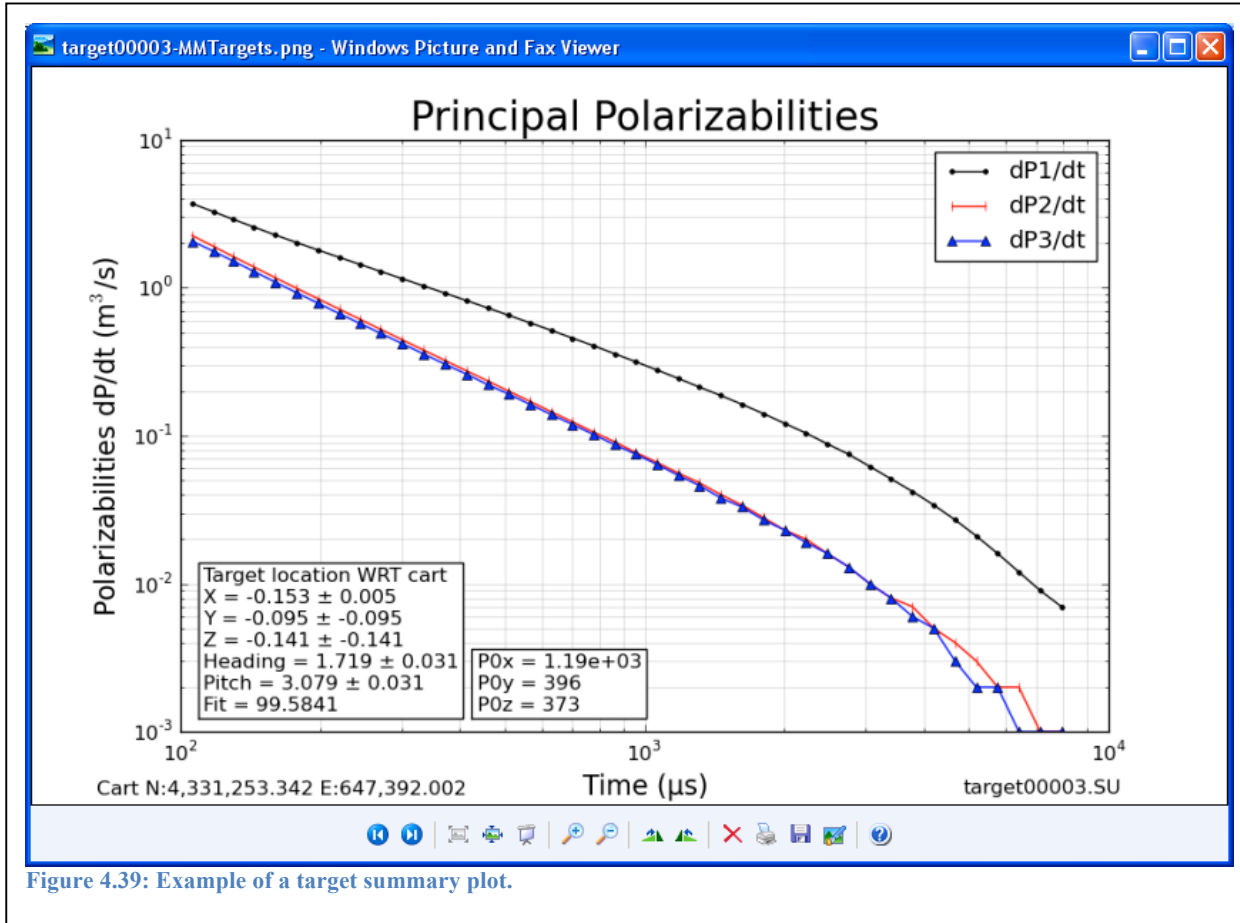


Figure 4.39: Example of a target summary plot.

## 5 Discussion and Recommendations

This project has addressed a number of important issues associated with UXO remediation. This Section summarizes the contributions of this project, makes conclusions from the results obtained, and makes recommendations for future work.

### 5.1 New Contributions and Conclusions

The tasks in this project all made significant contributions to UXO research. Before considering the contributions of each task, we list the capabilities of a program named *MMTargets* that has contributed to each of these tasks. *MMTargets* has been configured for the *MetalMapper*, and has several operating modes as described below.

1. *MMTargets* can create synthetic datasets to simulate both static and dynamic datasets for a wide range of targets. EM noise, positional uncertainty, and orientation uncertainty can each be added to the simulated data. This is very useful for studies pertaining to optimizing coil geometries, positioning equipment, and survey design.
2. *MMTargets* can conduct shape-constrained inversions.
3. *MMTargets* provides consistent orientation of principal polarizabilities through the entire decay curve.
4. *MMTargets* can perform multi-target inversions.
5. *MMTargets* has a physics-based detection routine that helps detect targets along lines of dynamically acquired data. In this mode, it provides initial estimates of target position and size.
6. *MMTargets* takes coil geometry definitions from a text file, so it can easily be customized for processing data acquired by other time-domain EMI instruments.

The five main tasks in this project covered a lot of ground. The salient contributions of each task as listed below.

1. Improved Target Detection – This task implements a simple physics-based indicator in the *MetalMapper* acquisition program and in *Oasis montaj*. The model used by the indicator is a spherical target. An inversion routine using this simple model has also been added to *MMTargets*. These routines will help users find the location of targets during acquisition and processing. This will likely reduce the number of statically acquired targets that are off-center.
2. Target Parameter Extraction with Multiple-Point Static or Dynamic Data Sets – The capability of *MMTargets* to invert multiple-point static datasets for single and multiple targets has been demonstrated. Both modeled data and actual survey data were used in the single target demonstration, while only modeled data were used in the multi-target demonstration. Essentially, *MMTargets* has the functionality to invert any *MetalMapper* dataset acquired by any means for single or multiple targets to provide characteristic information to a classifier.

3. Optimal Array Configuration(s) – The optimal array task addressed the issue of survey instrument cost and complexity versus benefit to characterization and classification efforts. Several transmitter-receiver permutations were investigated.
4. Multiple Source Detection – The objective here is to identify those target picks associated with complex secondary magnetic fields that arise either from the presence of multiple targets in close proximity, targets that are asymmetrical, or that may be too large dimensionally to be approximated with a point dipole. A multi-target inversion algorithm has been developed and tested. Downward continuation and reduction-to-pole algorithms have also been developed to aid interpretation and to provide useful starting models for the multi-target inversion.
5. Oasis montaj Integration – This task was not part of the original work scope, but was added after the program office suggested that the new routines should be integrated into existing *Oasis montaj* workflows. *TEM2CSV* and *TEM2SU* were created to help import the TEM files recorded by the *MetalMapper* system into *Oasis montaj*. *Oasis montaj* GXs have been written to do the following:
  - a. Streamline the import of *MetalMapper* data,
  - b. Perform constrained inversions using several basic shapes,
  - c. Generate inversion summary plots for each target,
  - d. Import inversion results into *Oasis montaj* for use in classification routines.

## 5.2 Recommendations and Future Work

This project has expanded the software support for current state-of-the-practice *MetalMapper* surveys. The detection and inversion phases have been enhanced. These routines have been demonstrated with modeled data and with a few cases from actual surveys. Nonetheless, more testing is needed demonstrate that these routines should be part of standard workflows.

### 5.2.1 Recommendation for *MMTargets*

1. The primary reason for the broad F-Test distributions is noisy data, which produces a noise objective function. While the noise is small enough to permit reasonable inversion results, the noise causes a number of small local minima in the same vicinity of the reported solution. The local minima in the vicinity of the solution all have similar MSE values, and some will likely have lower MSE values than that of the reported solution. It is anticipated that smoothing the objective function will reduce these difficulties and reduce the breadth of the F-Test distributions. This is recommended as future work.

### 5.2.2 Recommendation for Detection

1. The real-time detection routines should reduce the errors and erroneous results due to static data collection at significant lateral offsets. This needs to be demonstrated.
2. In addition to the state-of-the-practice workflow, we have demonstrated the capability to invert dynamic data. This capability needs to be further tested and integrated into the standard *Oasis montage* workflows. With successful dynamic surveys, it may be possible to significantly reduce the cost of geophysical detection and classification efforts by

significantly reducing or eliminating the queued re-acquisition phase. We recommend further development and testing for dynamic surveys.

### 5.2.3 Recommendations for Optimal Arrays

1. Our target sets were generated with a single noise level consistent with noise measurements at several demonstration sites. During analysis we discovered that we did not account properly for the noise reduction due to stack measurements ( $\sqrt{N}$ ). As a result, the noise levels were perhaps overly high. The high noise does not affect the relative rankings of the arrays since data sets for each array were generated with identical noise statistics. However, we would like to investigate different noise levels and how they affect the overall results.
2. We would like to extend the multiple site study in 2 ways. We would like to experimentally determine the required specification for both position and attitude accuracy such that multiple-site measurements (say 2 to 5 closely spaced sites) might achieve the improved performance. If we use more sites, can we relax the standards for platform position and attitude accuracy?

### 5.2.4 Recommendations for Multiple Targets

1. Multi-target inversion remains difficult. While we have made significant inroads, there are still testing and algorithmic improvements that are needed. Reduction-to-pole reduces the search space by significantly constraining the lateral position of the target.
2. There are many statistical source separation methods available that may be applicable to the multiple source problem. In addition to MUSIC, statistical methods such as independent component analysis and blind source separation may be applicable [9]. A combination of physical constraints such as downward continuation and Green's function relationships with statistical measures such as independence should be investigated.
3. The interleaved multi-target solver may perform better if the parameters for all targets are simultaneously optimized at each Gauss-Newton iteration. This should be tested.

### 5.2.5 Recommendations for *Oasis montaj* Enhancements

1. *MMTargets* has the ability to model static and dynamic data with various coil geometries, EM noise, and uncertainty in cart location and orientation provides a cost-effect method for testing new algorithms and proposed instrument arrays. This capability should be added to *Oasis montaj* to allow practitioners to design surveys and test various scenarios.
2. The reduction-to-pole and interleaved multi-target inversion routines should be integrated into the *UXTargets* processing menu so that they can be further evaluated using actual survey data.
3. In order to invert dynamic data, data patches outlined by polygons must be generated. The USGS *ALLTEM* data processing package has this capability. These routines should be extended to operate with *MMTargets* and added to the *UXTargets* processing menu.
4. The USGS *ALLTEM* data processing package has a set of statistical classification routines based on the highly regarded open-source '*R*' statistical software package. These routines should be added to the *UXTargets* menu.

### 5.3 Future Plans

We will continue to seek funding sources from both the commercial and government sectors for testing and enhancing the new processing routines. The algorithms we have developed can easily be tailored to support other popular EM instruments such as the NanoTEM, the BUD, the AOL, the TEMTADS, and the EM63. We will seek demonstration opportunities using these instruments as well.

## 6 References

- [1] C. P. Oden, "Combining Advances in EM Induction Instrumentation and Inversion Schemes for UXO Characterization," *Progress in Electromagnetic Research*, vol. Submitted, 2011.
- [2] R. E. Grimm, and T.A. Sprott, "Model-based sensor design optimization for UXO classification," in *UXO/Countermine Forum 2002*, Orlando, FL, 2002.
- [3] B. Barrow, and Herbert H. Nelson, "Effects of Position Error on Inverting EMI Data for UXO Discrimination Using the MTADS Platform," in *The UXO/Countermine Forum*, New Orleans, LA, 2001.
- [4] J. T. Smith, and H. Frank Morrison, "Optimizing Receiver Configuration for Resolution of Equivalent Dipole Polarizabilities In Situ," *IEEE Trans. on Geosc. & Rem. Sens.*, vol. 43, pp. 1490-1498, July 2005.
- [5] R. E. Grimm, "Triaxial Modeling and Target Classification of Multichannel, Multicomponent EM Data for UXO Discrimination," *Jour. Envir. & Eng. Geophys*, vol. 8, pp. 239-250, 2003.
- [6] D. D. Snyder, and David C. George, "Qualitative and Quantitative Detection of UXO with EMI Using Arrays of Multi-Component Receivers," in *SAGEEP 2006*, Seattle, WA, 2006.
- [7] L.-P. Song, Leonard R. Pasion, Stephen D. Billings, and Douglas W. Oldenburg, "Non-linear Inversion for Multiple Objects in Transient Electromagnetic Induction Sensing of Unexploded Ordnance: Technique and Applications," *IEEE Transaction on Geosciences and Remote Sensing*, vol. Submitted for Publication, p. 13, 2010.
- [8] L. P. Song, Douglas W. Oldenburg, Leonard R. Pasion, and Stephen D. Billings, "Transient electromagnetic inversion of multiple targets," in *SPIE*, 2009, pp. 73030R-73030R-12.
- [9] R. J. Blakely, *Potential Theory in Gravity and Magnetic Applications*. New York: Cambridge University Press, 1996.
- [10] D. Keiswetter, "SAIC Analysis of Data Acquired at Camp Butner, NC," presented at the Partnersin Environmental Technology Technical Symposium and Workshop, Washington, DC, 2010.
- [11] F. Shubitidze, Ben Barrowes, Irma Shamatava, Juano Pablo Fernandez, and Kevin O'Neill, "The orthonormalized volume magnetic source technique applied to live-site UXO data: Inversion and classification studies," *SEG Expanded Abstracts*, vol. 30, pp. 3766-3770, 2011 2011.
- [12] L.-P. Song, and Douglas W. Oldenburg, "Estimating Source Locations of UXO using the MUSIC algorithm," *Geophysics*, vol. Submitted, 2011.
- [13] A. Hyvarinen, J. Karhunen, and E. Oja, *Independent Component Analysis*. New York: Wiley and Sons, 2001.

## 7 Appendix A

We describe the problem formulation for Laplace's equation using the separation of variables technique below

Starting with Laplace's equation:  $\nabla^2 B = \frac{\partial^2 B}{\partial x^2} + \frac{\partial^2 B}{\partial y^2} + \frac{\partial^2 B}{\partial z^2} = 0$

If we assume that  $B$  is separable, that is it can be written as a product of three functions of one variable such as  $B = X(x)Y(y)Z(z)$ , then

$$\nabla^2 B = \frac{\partial^2 XYZ}{\partial x^2} + \frac{\partial^2 XYZ}{\partial y^2} + \frac{\partial^2 XYZ}{\partial z^2} = YZ \frac{\partial^2 X}{\partial x^2} + XZ \frac{\partial^2 Y}{\partial y^2} + XY \frac{\partial^2 Z}{\partial z^2} = \frac{1}{X} \frac{\partial^2 X}{\partial x^2} + \frac{1}{Y} \frac{\partial^2 Y}{\partial y^2} + \frac{1}{Z} \frac{\partial^2 Z}{\partial z^2} = 0$$

Now the equation is separated and each term is a function of one variable. The only way this equation can be satisfied for all values of  $x$ ,  $y$ , and  $z$ , is if each term has a constant value and if the sum of these terms is zero.

$$\frac{1}{X} \frac{\partial^2 X}{\partial x^2} + \frac{1}{Y} \frac{\partial^2 Y}{\partial y^2} + \frac{1}{Z} \frac{\partial^2 Z}{\partial z^2} = \lambda_x + \lambda_y + \lambda_z = 0$$

The equation with the  $\lambda$ 's is the characteristic equation for the Laplace equation, and the  $\lambda$ 's are called the Eigenvalues. If we assume a solution of the Laplace equation of the form

$$B = B_0 e^{\alpha_x x + \alpha_y y + \alpha_z z} = X_0 e^{\alpha_x x} Y_0 e^{\alpha_y y} Z_0 e^{\alpha_z z},$$

then

$$\frac{X_0}{X} \frac{\partial^2 e^{\alpha_x x}}{\partial x^2} + \frac{Y_0}{Y} \frac{\partial^2 e^{\alpha_y y}}{\partial y^2} + \frac{Z_0}{Z} \frac{\partial^2 e^{\alpha_z z}}{\partial z^2} = \frac{X_0 \alpha_x^2 e^{\alpha_x x}}{X} + \frac{Y_0 \alpha_y^2 e^{\alpha_y y}}{Y} + \frac{Z_0 \alpha_z^2 e^{\alpha_z z}}{Z} = \alpha_x^2 + \alpha_y^2 + \alpha_z^2 = 0$$

Now at least one term (one of the  $\alpha$ 's) in the above equation must be negative and at least one must be positive. Although there are other possibilities, we are free to choose the following, which satisfies this sign constraint for all values of  $k_x$ ,  $k_y$ , and  $k_z$ :

$\alpha_x = ik_x$ ;  $\alpha_y = ik_y$ ;  $\alpha_z = k_z$ . This leads to a solution of the form

$$B = B_0 e^{i(k_x x + k_y y) + k_z z} = X_0 e^{ik_x x} Y_0 e^{ik_y y} Z_0 e^{k_z z} = X(x)Y(y)Z(z)$$

which casts the solution in terms of the Fourier transform of  $B$  with respect to  $x$  and  $y$ . The wavenumber variable  $k_z$  can be written in terms of the wavenumber variables  $k_x$  and  $k_y$ :

$$k_z^2 = k_x^2 + k_y^2$$